

DESIGNING AND OPTIMIZING GRATINGS FOR SOFT XRAY DIFFRACTION EFFICIENCY

A Thesis Submitted to the
College of Graduate Studies and Research
in Partial Fulfillment of the Requirements
for the degree of Master of Science
in the Department of Physics and Engineering Physics
University of Saskatchewan
Saskatoon

By
Mark Boots

©Mark Boots, October 2011. All rights reserved.

PERMISSION TO USE

In presenting this thesis in partial fulfilment of the requirements for a Postgraduate degree from the University of Saskatchewan, I agree that the Libraries of this University may make it freely available for inspection. I further agree that permission for copying of this thesis in any manner, in whole or in part, for scholarly purposes may be granted by the professor or professors who supervised my thesis work or, in their absence, by the Head of the Department or the Dean of the College in which my thesis work was done. It is understood that any copying or publication or use of this thesis or parts thereof for financial gain shall not be allowed without my written permission. It is also understood that due recognition shall be given to me and to the University of Saskatchewan in any scholarly use which may be made of any material in my thesis.

Requests for permission to copy or to make other use of material in this thesis in whole or part should be addressed to:

Head of the Department of Physics and Engineering Physics
Rm 123 Physics Building
116 Science Place
University of Saskatchewan
Saskatoon, Saskatchewan
Canada
S7N 5E2

ABSTRACT

This is the abstract of my thesis.

ACKNOWLEDGEMENTS

Acknowledgements go here. Typically you would at least thank your supervisor.

This is the thesis dedication (optional)

CONTENTS

Permission to Use	i
Abstract	ii
Acknowledgements	iii
Contents	v
List of Tables	vii
List of Figures	viii
List of Abbreviations	xiii
1 Introduction	1
2 Motivation: Why grating efficiency matters	2
2.1 Soft X-ray Spectroscopy Techniques	4
2.1.1 Absorption spectroscopy	5
2.1.2 Emission spectroscopy	6
2.1.3 Importance of Soft X-ray Spectroscopy (SXS)	7
2.2 Spectroscopy Instrumentation	8
2.2.1 Beamline optics: Monochromators and Spectrometers	11
2.2.2 Goals for Soft X-ray Instruments	13
2.2.3 Challenges of Soft X-ray Applications	16
2.3 REIXS spectrometer project	17
2.4 Summary: Why Grating Efficiency Matters	18
3 Theory: How to calculate grating efficiency	20
3.1 Introduction and brief history of grating theory	20
3.1.1 Simplifying Assumptions	24
3.1.2 Electromagnetic field and polarization	26
3.1.3 Maxwell's equations for sinusoidal time-varying fields	26
3.1.4 Periodicity of gratings and fields (aka, pseudo-periodic functions and the Fourier basis)	28
3.1.5 Deriving the Grating Equation	30
3.2 Defining Grating Efficiency	35
3.3 Solving for efficiency	38
3.3.1 Numerical Challenges	38
3.3.2 Applying boundary conditions within the groove region	38
3.3.3 Handling stacks of gratings	38
3.4 X-rays and materials: how do they interact?	38
4 Implementation of Theory: What people and I did to implement the theory using computers	42
4.1 Methods	42
4.1.1 Rigorous Coupled Wave method: GSolver	42
4.1.2 Differential method: Gradif by Michel Neviere	42
4.2 Improving the usability and efficiency of calculation methods	42
4.2.1 Visual interface to the Gradif code	43
4.2.2 Detecting convergence failures	47

4.2.3	Open source, open access, and future work	47
4.3	General trends and factors affecting efficiency	49
4.3.1	Effect of grating profile: groove shape	49
4.3.2	Effect of groove density	58
4.3.3	Effect of coating thickness	58
4.3.4	Comparison of coating materials	62
4.3.5	Effect of photon energy / wavelength	65
4.3.6	Effect of incidence angle	65
4.3.7	TODO Applications to beamline and instrument design	68
4.4	Validation: comparison of theory to experimental results	71
5	Design: How David and I applied these tools to make the REIXS spectrometer optical design	76
5.1	Application to spectrometer design	76
5.1.1	Design goals	76
5.1.2	Comparative examples	77
5.2	Design Process	79
5.2.1	Justification of design choices	81
5.3	High-resolution (3rd order) design	85
5.3.1	Options for reaching extreme resolution	85
5.3.2	Justification for 3rd order design	85
5.4	TODO Coating choices:	86
5.5	TODO: Optimization and Tolerancing	86
5.6	Summary of Final Design	86
6	Characterization: How we measured the actual grating performance, and accounted for differences	93
6.1	AFM measurements of the manufactured grating profile	94
6.2	Diffractometer measurements of actual grating efficiency	95
6.2.1	Beamline 6.3.2 reflectometer	96
6.2.2	Diffraction experiment procedure	99
6.2.3	Sources of error	104
6.3	Real-world grating effects	107
6.3.1	Stray radiant energy	107
6.3.2	Manufacturing errors the <i>can</i> be modelled	112
6.4	Grating results	112
6.4.1	LEG	112
6.4.2	IMP	113
6.4.3	MEG	113
6.4.4	HEG	113
6.4.5	HRMEG and HRHEG	114
7	Real-World results: Why there aren't any yet	122
8	Future work: What should have been in Chapter 6	123
	References	124
A	Sample Appendix	126
B	Another Sample Appendix	127

LIST OF TABLES

4.1	Critical incidence angles for “total external reflection” at 410 eV for the mirror and grating coatings shown in Figure 4.16.	67
4.2	Geometry parameters and incidence configuration for the gratings in Figures 4.20 to 4.23. The geometry measurements were taken at the center of the grating; accurate characterization of these gratings after ruling made them ideal for comparing with theoretical calculations. CIA stands for “constant included angle” – a mounting configuration which maintains a constant angle between the incident direction and 1st order.	71
5.1	Gratings chosen for the REIXS spectrometer, with their target energies used for optimization, the energy ranges they will be able to cover, and the final optimized grating parameters . . .	79
5.2	Predicted resolving power (RP, $E/\Delta E$) and grating efficiency (Eff) of the REIXS spectrometer at the emission lines of interest. Values are listed for all gratings where the emission energy lies within the detector’s motion range. (Resolving power results are taken from (TODO REF david’s thesis).)	88
6.1	For higher-order suppression, Beamline 6.3.2 has a variable-incidence mirror and a set of transmission filter elements. The mirror coating, mirror angle, and filter need to be selected based on the energy range of the scan. (Mirror angles are measured from grazing incidence.)	105

LIST OF FIGURES

2.1	A rather sensitive, compact, visible light spectrometer (Ocean Optics USB4000-UV-VIS). It uses a blazed reflection grating optimized for 300nm light, and connects to a personal computer using USB. Image credit: OCEAN OPTICS, INC. [10]	3
2.2	In this schematic of a grating monochromator, light from the source is focussed by mirrors and dispersed by the grating. An exit slit picks out the desired wavelength or energy range, and blocks the remaining light. Depending on the design, the output wavelength can be adjusted by changing the angle of the grating, the angle of the mirrors, and/or the position of the exit slit. (The resolution – the energy bandwidth of the outgoing light – depends on the dispersion of the grating, the geometry, and the size of the exit slit. An ideal monochromator would produce truly monochromatic light, but this would require an infinitely small slit.)	9
2.3	In this schematic of a grating spectrometer, mirrors are used to focus light from the source (or entrance slit) onto the detector, passing over a plane grating en-route to disperse the light by wavelength. (This is a <i>Czerny-Turner</i> arrangement, typical of compact visible-light designs like the one in Figure 2.1.) Since the grating diffracts different wavelengths at different angles, the intensity distribution across the detector surface creates a spectrum related to the wavelength (or photon energy).	10
2.4	The spectrometer in this schematic uses a curved grating to both disperse light by wavelength, and focus it onto the detector. (This is typical of soft x-ray designs where the poor reflectivity of additional mirrors is usually avoided.) The intensity distribution along the surface of the detector can be converted into a spectrum with respect to wavelength or energy. Since the detector only captures a limited range of outgoing angles, it can be moved to pick out the desired wavelength window for each measurement.	10
2.5	The Petersen Plane Grating Monochromator, as implemented on the HE-PGM-3 beamline at BESSY. In Ref. [20], Petersen et. al. provide a good overview of monochromator focussing techniques, prior to the widespread adoption of VLS designs. Image from: [20].	12
2.6	The SXF endstation spectrometer on Beamline 8.0.1 of the Advanced Light Source – a typical “workhorse” spectrometer. It uses spherical gratings in a Rowland Circle design; four gratings let users choose between higher resolution or higher efficiency at different energy ranges. The resolving power of this machine is compared with other leading spectrometers in Figure 5.1. Image from: [12]	13
2.7	A detector image and corresponding spectrum produced by the SXF spectrometer in Figure 2.6. (This particular scan is of the nitrogen emission lines in nitrogen-doped zinc oxide.) The curvature of the spherical gratings provides focussing in the dispersion direction (x -axis), but unfortunately produces a curved image in the perpendicular direction (y -axis). This curvature is corrected by aligning rows along the red curve when the image is summed to produce the spectrum on the right.	14
2.8	The detector has an effective spatial resolution dx which is the minimum distance required to resolve two adjacent incident rays. Except for the $n = 0$ order, the grating produces an angular dispersion $d\theta_{2,n}/d\lambda$, which is the angular separation between infinitesimally-adjacent wavelengths. To increase the spacing between adjacent wavelengths on the detector, we can either increase the grating-detector distance r' , or increase the angular dispersion.	15
2.9	A variety of soft x-ray spectroscopy techniques, and the number of gratings required in the beam path to accomplish each one. Of these techniques, those in <i>italic text</i> are possible on the REIXS beamline using the emission spectrometer endstation. For all these techniques – and particularly those using two gratings – more efficient gratings would increase the speed of experiments, improve the quality of data, and increase the minimum concentration of samples that can be feasibly studied.	19
3.1	A one-dimensional grating with in-plane incidence.	20

3.2	The Rayleigh expansion describes the electric field (TE polarization) or magnetic field (TM polarization) in homogenous media, above and below the grating. The terms in the expansion include a finite number of propagating plane waves – the diffraction orders – and an infinite number of decaying, or “evanescent” plane waves. From the geometry of the diffracted and transmitted wave vectors, we can derive the grating equation, but we need to solve the A_n and B_n coefficients to determine the efficiency of each order.	32
3.3	The total electromagnetic flux through this highlighted area (Q_2) is used to define the grating efficiency of a diffraction order n , as the ratio of the flux of the diffracted wave $\bar{S}_n^{(2)}$ compared to the incident wave $\bar{S}^{(2)}$	36
3.4	Arbitrarily-complicated structures can be handled by dividing the grating into layers, where each layer is either homogenous (constant refractive index), or modulated (with a refractive index that changes periodically as a function of x at any given height y).	39
3.5	Modulated layers in a complicated stack of gratings. In between every layer, we can insert an imaginary, infinitely-thin homogenous layer where the Rayleigh expansion applies. The A'_n and B'_n expansion coefficients connect the boundary conditions between layers. Within each layer, the Rayleigh expansion does not apply – inside the grooves, the field cannot be represented as a simple sum of plane waves – and numerical methods are required to approximate it.	40
4.1	The RCW method approximates every real grating as a stack of rectangular gratings, where the boundary conditions are easy to solve and the problem can be reduced to algebraic methods.	42
4.2	This web application provides a graphical user interface for calculating grating efficiencies. Forms prompt users for the grating parameters.	44
4.3	This web application provides a graphical user interface for calculating grating efficiencies. The results are plotted, and users can download a text-based table for further analysis.	46
4.4	This ‘Options’ page configures the numerical precision of the calculations, the diffraction orders of interest, and the polarization of the incident light. It also sets some other house-keeping options for where users want to store their data.	48
4.5	5 common groove profiles and their geometry parameters. The rectangular profile (a) and triangular profile (b) are idealized versions of those produced by mechanical ruling. The trapezoidal profile (c) is usually produced accidentally while trying to rule a rectangular profile with an imperfect ruling tip. The sinusoidal profile (d) is the natural shape produced by holographic ruling; the result can be ion-etched to approximate a triangular profile (e).	50
4.6	Henry Rowland’s ruling engine, mechanically engraving a grating under the operation of his instrument maker Theodore Schneider. Photographed at Johns Hopkins University, Baltimore. Image credit: EMILIO SEGRE VISUAL ARCHIVES/AMERICAN INSTITUTE OF PHYSICS/SCIENCE PHOTO LIBRARY (TODO ref http://www.sciencephoto.com/media/150151/enlarge)	51
4.7	The MIT ‘B’ ruling engine, now owned and operated by Richardson Gratings (a division of the Newport Corporation). It can rule gratings up to 420 mm wide, with grooves up to 320 mm long. The maximum groove density is 1500 lines/mm. Equipped with a servo system for advancing the grating carriage and interferometric feedback using frequency-stabilized lasers, it is the most accurate ruling engine in the world. To control for thermal expansion of the engine, the room temperature is controlled to 0.005°C; the system even compensates for changes in room air pressure since a change of just 2.5 mm of mercury will affect the refractive index of air (and therefore the interferometer wavelength) by one part per million. The entire engine is suspended from springs to dampen vibrations between 3Hz to 60Hz, which could otherwise be transmitted to the diamond tip. Image credit: DIFFRACTION GRATING HANDBOOK (TODO REF).	52

4.8	Master gratings can be replicated using a resin which hardens while in contact with the master (or subsequently, a submaster replicated from the first master). First, a parting agent (2) is applied to the surface of the master; it must be thin and uniform otherwise it will affect the profile. A metallic (aluminum or gold) coating about 1 μ m thick is then applied above the parting agent; this coating will eventually end up as the top surface of the replicated grating, and is called the <i>transfer coating</i> (3). Finally, the replica blank (5) is cemented from above using a resin (\sim 10 μ m thick) that hardens under UV exposure or over time (4). Once the resin is cured, the gratings are separated at the parting agent layer, leaving the hardened resin in the shape of the grooves, with the metal coating adhered to the top. This will produce a mirror image of the master grating; to create a perfect replica, this first replica needs to be replicated again.	53
4.9	The Sheridan technique for recording pseudo-blazed holographic gratings uses a single light beam reflected back on itself to make a regular interference pattern of standing waves. The master substrate consists of a <i>transparent</i> photoresist material which is hardened or weakened by exposure to the light. By placing the substrate at an angle θ to the light path, the light and dark fringes are stretched out parallel to the grating surface; additionally, the angled incidence creates a lopsided sinusoidal intensity pattern that mimics blazed gratings. Image credit: DIFFRACTION GRATING HANDBOOK (TODO REF).	54
4.10	In the blazed condition, the desired order diffraction angle – in this case, 1st order – is aligned with the direction of specular reflection off the groove surfaces.	56
4.11	0th order, 1st order, and 2nd order efficiency of three different groove profiles, all optimized for use at 400 eV. The blazed grating is superior in both 1st and 2nd order. All gratings: 1200 lines/mm, Platinum coating. Blazed: 1.46° angle, 60° anti-blaze angle. Sinusoidal: 13.7 nm groove depth. Laminar (rectangular): 9.6nm groove depth, 50% duty cycle.	57
4.12	Increasing the groove density always decreases the diffraction efficiency – at least for all the useful orders ($n \neq 0$). In these plots, we have tried to control for inter-related factors: For the blazed grating in (a), the blaze angle has been adjusted with the groove density (using Equation 4.8) to maintain the on-blaze condition. In (b), the sinusoidal grating depth was optimized at 1200 lines/mm, and then the depth-to-period ratio was maintained across changes to the groove density.	59
4.13	0th order, 1st order, and 2nd order efficiency as a function of energy, for a range of groove densities from 300 to 2700 lines/mm. All gratings are triangular, platinum-coated, with an optimal blaze angle dependent on the groove density according to Equation 4.8. (Blaze angles are shown in the legend.) As the groove density increases, the maximum achievable efficiency drops, but the bandwidth of the blaze-optimization peak becomes wider.	60
4.14	In the soft x-ray regime under grazing incidence, metal-coated dielectric gratings are indistinguishable from pure metal gratings. . . as long as the coating is thicker than \sim 20nm (although the exact thickness depends on the material, photon energy, and incidence angle). These calculations show Pt coatings of varying thickness over an SiO ₂ substrate, as well as an infinitely thick pure Pt grating. (Blazed grating, 1200 lines/mm, 1.46° blaze angle, 88° incidence. . . .	61
4.15	The reflectivity of a pure mirror at grazing incidence (88°), as a function of photon energy. Lighter elements like carbon and nickel have the highest peak reflectivity, but have strong absorption features. Heavier metals, particularly those within the platinum group, have reasonable reflectivity over the entire soft x-ray region of interest. Up to 200 eV, gold has a higher reflectivity than Pt and Ir.	63
4.16	A comparison of the mirror reflectivity, 0th order, and 1st order efficiency for different coating materials, as a function of photon energy. (Gratings: Sinusoidal profile, 88° incidence angle, 1200 lines/mm, 13.7 nm groove depth.) Note that the 1st order efficiency has energy-dependent features that are not visible in the simple reflectivity.	64
4.17	The reflectivity of a perfect platinum mirror as a function of incidence angle at 410 eV, calculated using the complex refractive index and the complex Fresnel equations. The “total external reflection” approximation suggests a critical angle of 83.3° for total reflection, but due to absorption within the material, the reflectivity only reaches 1 at complete grazing incidence (90°). There is no substantial difference between TE and TM polarization.	67

4.18	The effect of incidence angle on diffraction efficiency for various grating profiles. While the 0th order efficiency/reflectivity always increases as the incident light becomes more grazing, there is an optimal incidence angle below 90° for higher-order light. The critical angle for total external reflection in Platinum is 83.3° ; clearly both the 0th-order and 1st-order efficiency drop off significantly below this angle. (Gratings: 1200 lines/mm, platinum coating, 400 eV; blaze angles and profiles as indicated.)	69
4.19	While the blaze angle can always be used to tune a grating for a required incidence angle, there is still a particular <i>optimal</i> incidence angle that – when combined with a corresponding optimized blaze angle – would produce the highest achievable efficiency. This optimal angle doesn't seem to depend on the material, but only on the groove density and energy. (Gratings: all 1200 lines/mm; coatings, blaze angles, and energies as indicated.)	70
4.20	Comparison of grating efficiency calculations to diffractometer measurements. Blazed grating, 1440 lines/mm, 2.2° blaze angle, 12.8° anti-blaze angle. Incidence: 160° constant included angle to the 1st inside order.	72
4.21	Comparison of grating efficiency calculations to diffractometer measurements. Rectangular grating, 600 lines/mm, 22.2 nm depth, 1.12 μ m valley width. Incidence: 167° constant included angle to the 1st inside order.	73
4.22	Comparison of grating efficiency calculations to diffractometer measurements. Trapezoidal grating, 300 lines/mm, 57° side angles, 49.3 nm depth, 2.46 μ m valley width. Incidence: 167° constant included angle to the 1st inside order.	74
4.23	Comparison of grating efficiency calculations to diffractometer measurements. Trapezoidal grating, 390 lines/mm, 57° side angles, 54 nm depth, 1.39 μ m valley width. Incidence: 160° constant included angle to the 1st inside order.	75
5.1	Resolving power performance comparison of existing spectrometer designs, calculated with all detectors having a 20 μ m pixel size. The legend specifies the spectrometer and grating choice (size and/or line density). Image from (TODO REF: David Muir M.Sc. thesis.)	78
5.2	Approximation of the process used to design the optics of the REIXS spectrometer.	80
5.3	The focal curve is the path in space the detector needs to move along to maintain focussing as a function of energy. This plot shows the effect of the b_2 VLS correction term: with a b_2 of 0, the focal curve is the same as the Rowland circle focal curve. A specific b_2 value of -12 (highlighted in red) straightens the focal curve, which could simplify the detector mechanics, but also shortens the focal distance and reduces the resolution at the detector. Image from (TODO REF Figure 2.17)	82
5.4	Variable line space (VLS) corrections reduce aberrations that cause curvature, as seen in these ray-traced detector images of three adjacent emission lines. However, the increase in resolution due to better focussing is not able to make up for reduced dispersion across the surface of the detector, as compared to the Rowland circle alternative. Image from (TODO REF Figure 2.18)	82
5.5	Common errors in the manufacture of ruled and holographic gratings. Holographic exposure creates a sinusoidal profile; subsequent ion-etching (b) can only approximate a triangular profile. Ruled gratings can suffer from blaze angle errors (c), or errors due to the shape and/or depth of the diamond tip (e). If the ruling engine introduces periodic errors in the groove position, this additional structure (d) superimposes additional diffraction patterns (ghosts).	83
5.6	At some points along the efficiency curve, the grating efficiency is actually higher in 3rd order than it would be in 1st order for an equivalent-resolution grating with three times the groove density. . . assuming you could even manufacture such a grating. HRMEG and alternatives: nickel coating, geometry as indicated. HRHEG and alternative: platinum coating, blaze angle of 4.05°	87
5.7	The REIXS spectrometer design offers higher predicted resolution than the existing designs we surveyed in Figure 5.1. (The advantage is even more dramatic when considering the 3rd order high resolution gratings.) However, the full strength of the design comes from a knowledgeable balance with grating efficiency, based on our combined calculations. Image from: (TODO REF David's thesis Figure 4.7)	89
5.8	Theoretical diffraction efficiency for the Low Energy Grating and Impurity Grating.	90

5.9	Theoretical diffraction efficiency for the Medium Energy and High Energy Gratings.	91
5.10	Theoretical diffraction efficiency for the High Resolution Gratings, optimized to be used in 3rd order.	92
6.1	The Low Energy Grating has a smooth regular profile, shown in this example image measured using an Atomic Force Microprobe (AFM).	95
6.2	The Calibration and Standards Beamline (6.3.2) at the Advanced Light Source consists of a bending magnet source, a VLS-PGM monochromator with three selectable gratings, a higher-order suppressor, and a two-circle reflectometer shown in more detail in Figure 6.3. The curvature of refocussing mirror M3 can be adjusted to image the exit slit onto the sample, or to focus the light at infinite. Image from: (TODO REF http://cxro.lbl.gov/als632/)	96
6.3	The reflectometer on Beamline 6.3.2 at the Advanced Light Source allows for independently setting the angle of the gratings in the beam, and setting the angle of a pinhole photodiode detector. Upstream, filters in the beamline are used to remove contamination from the higher-order light of the monochromator.	97
6.4	In the coordinate convention for the reflectometer, the sample angle is measured up from grazing incidence, and the detector angle is measured up from grazing incidence. The sample position stage (x, y, z) is mounted to the sample angle stage, so that the centre of rotation is always at the height of the beam.	98
6.5	The simplest diffractometer experiment scans the detector angle while illuminating the grating with a constant photon energy. The diffraction orders are visible as peaks along the outgoing angle axis (measured up from the incident beam direction at 0°). The 0th order (reflection) peak is easily visible at 3.5° , or twice the incident angle (88.25° , or 1.75° from grazing). Grating: HRHEG.	101
6.6	When the groove density of a grating is accurately known, the detector angle can be moved in tandem with the monochromator energy to keep it on the diffraction peak as the incident photon energy is scanned. This allows faster, nearly continuous efficiency measurements as a function of photon energy. (Grating: LEG)	102
6.7	Roughness of the grating surface scatters stray light outside the diffraction orders. Typically, surface roughness is responsible for most of the reduction in real-world grating efficiency, compared to theoretical calculations.	108
6.8	Unprotected Nickel quickly forms a surface oxide of NiO, which strongly reduces the reflectivity at the Oxygen edge (525eV)	113
6.9	AFM measurements of the Low Energy Grating (LEG) profile, averaged along the grooves (TODO μm x TODO μm). The best-fit blaze angle is at the centre of the grating.	114
6.10	Theoretical and measured efficiency of the Low Energy Grating (LEG).	115
6.11	AFM measurements of the Impurity Grating (IMP) profile, averaged along the grooves (TODO μm x TODO μm). The best-fit blaze angle is at the centre of the grating.	116
6.12	Theoretical and measured efficiency of the Impurity Grating (IMP).	116
6.13	AFM measurements of the Medium Energy Grating (MEG) profile, averaged along the grooves (TODO μm x TODO μm). The best-fit blaze angle is at the centre of the grating.	117
6.14	Theoretical and measured efficiency of the Medium Energy Grating (LEG).	117
6.15	AFM measurements of the High Energy Grating (HEG) profile, averaged along the grooves (TODO μm x TODO μm). Severe ruling errors were apparent. The profile wasn't sufficiently triangular to attempt to fit a blaze angle.	118
6.16	Theoretical and measured efficiency of the High Energy Grating (LEG).	119
6.17	AFM measurements of the HighRes Medium Energy Grating (HRMEG) profile, averaged along the grooves (TODO μm x TODO μm). The best-fit blaze angle is at the centre of the grating.	120
6.18	AFM measurements of the HighRes High Energy Grating (HRHEG) profile, averaged along the grooves (TODO μm x TODO μm). The best-fit blaze angle is at the centre of the grating.	121

LIST OF ABBREVIATIONS

LOF	List of Figures
LOT	List of Tables

CHAPTER 1

INTRODUCTION

blah blah blah

remember to include in introduction:

- - define diffraction grating (transmission, reflection)
- - orders... energy dispersiveness of non $n=0$ orders
- - what is: diffraction efficiency
- - mention: in most cases of beamline design the grating eff is hardly considered, or left to the manufacturer. Even more rare to actually **test** the gratings for their actual efficiency.

CHAPTER 2

MOTIVATION: WHY GRATING EFFICIENCY MATTERS

In 1821, when Joseph von Fraunhofer first resolved the sodium doublet lines using a diffraction grating he fashioned out of metal wire stretched between the grooves of two screws, he probably would not have anticipated the full scientific impact of his invention. Immediately, these observations helped reinforce Fresnel's new wave theory of light [8]. More importantly, the diffraction grating quickly became the foundation of spectroscopy, superseding the prism as a wavelength-dispersive element with higher resolution, and applicable to radiation from the infrared to x-rays. Eventually it would enable a huge range of experiments and new discoveries in all fields of science:

- In astronomy, Fraunhofer himself was the first to conduct spectroscopic measurements on light from the sun, moon, planets, and stars. Shifts in the position of well-known absorption lines proved, using the Doppler Effect, that the universe was expanding. Today, the composition and temperature of galactic objects is routinely measured using grating-based spectroscopic techniques.¹
- In physics, visible spectroscopy of the hydrogen emission lines (Balmer Series) provided the data for Niels Bohr's explanation of electron levels in the atom. Peter's discovery of the Zeeman Effect – the splitting of emission lines in a magnetic field – was accomplished using a 20-foot Rowland Circle spectrometer [28]; his results back up the modern version of quantum theory and the magnetic and spin quantum numbers.
- In chemistry, many elements (such as caesium and rubidium, identified by Kirchhoff and Bunsen in 1860) were first discovered in trace amounts using spectral analysis.
- Biologists and biochemists regularly use spectrophotometers to assay the concentration of a tagged reagent in a solution, making gratings a routine (and almost forgotten) tool in life sciences, pharmaceutical, and genetic research.

One common lamentation of the early spectroscopists was the faintness of the light leaving the grating; indeed, we can imagine them in darkened rooms, peering through telescope objectives, straining to make out the faintest lines by eye (Figure TODO):

¹In fact, the company that manufactured the gratings for this project also ruled the gratings used in the Hubble Space Telescope.

Some lines can be distinguished in the spectrum of Procyon; but they are seen with difficulty, and so indistinctly that their positions cannot be determined with certainty. I think I saw a line at the position D in the orange.

Joseph Fraunhofer, in *Prismatic and Diffraction Spectra* [9, p. 61]

Photographic film – and later, modern imaging devices like CCDs – have probably succeeded in removing at least the physical pain associated with spectroscopy. However, increases in grating efficiency are even more important and useful today as they would have been in 1830. At visible wavelengths, more efficient gratings have already enabled a range of compact spectrometers with very high sensitivity, such as the convenient USB-powered computer peripheral in Figure 2.1. Other wavelength ranges are more challenging; grating efficiency is especially critical to the variety of soft x-ray spectroscopy experiments now taking place at synchrotrons around the world, where the low reflectivity of optical materials makes it difficult to build highly efficient devices.



Figure 2.1: A rather sensitive, compact, visible light spectrometer (Ocean Optics USB4000-UV-VIS). It uses a blazed reflection grating optimized for 300nm light, and connects to a personal computer using USB. **Image credit:** OCEAN OPTICS, INC. [10]

Simply put, the *diffraction grating efficiency* is the fraction of useful diffracted light outgoing from a grating, relative to the amount of incoming light. (Chapter 3 offers a more formal definition.) While spectroscopy experiments vary in hardware, instrumentation, and purpose, we can make a pair of very general observations on why the grating efficiency is so important. From the point of view of an experimenter, it affects the amount of light available to their sample or detector, and therefore:

1. It affects the *speed* at which experiments can be done, by determining the exposure time required to record data of sufficient quality. In general, improvements in grating efficiency could reduce the amount of time for a given measurement – or equivalently, increase the number of measurements that could be taken in a certain time period. (For example, it takes anywhere from 3 minutes to several hours to measure a soft x-ray emission spectrum on the 8.0.1 beamline at the Advanced Light Source, depending on the concentration of the sample and the desired resolution. One could argue that a factor of 2 optimization in the grating efficiency could almost double the number of users or the scientific throughput of the beamline.)

2. It affects the *feasibility* of doing an experiment in the first place. In situations where the experimental light source is extremely weak (for example, spectral analysis of faint stars in astronomy, or emission line measurements of trace elements in material science) the grating efficiency must be sufficient to raise the signal level above the background noise level seen by the detector. This is no longer a question of patience; if the signal level is below the background noise, our unhappy experimentalist could accumulate detector readings all day (or indefinitely) to no avail.²

The motivation for this project was therefore to understand the factors affecting the efficiency of diffraction gratings, and to apply this knowledge to their optimization. To accomplish this, we sought the ability to model gratings numerically and calculate their efficiency – a useful outcome for all grating spectroscopy applications.

However, we had another specific, selfish goal, which was actually our primary objective. At the onset of this project, we were involved in the optical design of a soft x-ray emission spectrometer, destined for use on the REIXS beamline at the Canadian Light Source. Working with David Muir, whose studies on spectrometer resolution are published in his M.Sc. thesis [17], we attempted to simultaneously achieve both *world-class resolution* and *record efficiency* for this machine.³ Therefore, although the calculation techniques presented in this thesis are general, our examination of trends in diffraction efficiency looks most closely at the types of gratings used in the soft x-ray regime.

Given our specific motivation, the following sections explain the ultimate goal of such a machine, and show how gratings are typically employed in soft x-ray spectroscopy.

2.1 Soft X-ray Spectroscopy Techniques

Soft x-rays are photons with energies in the range of approximately 100 to 10 000 eV (or wavelengths of about 10 to 0.1 nm). Unlike with hard x-rays, which are highly penetrating, soft x-ray energies correspond to the binding energies of core-level electrons in common, lightweight elements. This property is ironically responsible for both the experimental challenge of working with them – they are quickly absorbed by any matter over very short distances – as well as their inherent usefulness as a probe of the electronic structure in materials.

Soft x-ray experiments use this light – usually created by a tuneable source such as a synchrotron – and focus it onto a sample to be studied. Two techniques provide complementary information: absorption spectroscopy, and emission spectroscopy.

²In fact, Zeeman mentions in the introduction to his paper that he was inspired by Faraday, who spent the last years of his life trying, “but in vain, to detect any change in the lines of the spectrum of a flame when the flame was acted on by a powerful magnet”. Zeeman decided “it might be yet worth while to try the experiment again with the excellent auxiliaries of the spectroscopy of the present time...” [28], brought on by Henry Rowland’s new mechanically-ruled reflection gratings.

³As it turns out, these two goals are implicitly in conflict; see Section 2.2.2.

2.1.1 Absorption spectroscopy

Absorption spectroscopy measures the absorption rate of photons as a function of their wavelength (or energy). Experimentally, this is done by shining a monochromatic beam of light onto the sample and measuring the amount of light absorbed as the energy of the beam is changed.

Figure TODO shows the available absorption processes. When the photon energy increases to become sufficient to excite an electronic transition in the material, dramatically more photons will be absorbed; this is known as an *absorption edge* (Figure TODO). Near the edge, as photons are absorbed by exciting electrons from the core level into unoccupied levels, adjacent unoccupied levels will have different probabilities of experiencing a transition, according to the quantum mechanical nature of the bonding in the material. (Note that according to the selection rule for dipole radiation, only electron transitions with a change in orbital angular momentum quantum number $\Delta l = \pm 1$ are allowed, since momentum must be conserved and photons have an angular momentum [spin] of one unit.) The absorption will increase for energies where the transition probability is higher; therefore, the absorption spectrum is actually a measure of the *density of unoccupied states* for electrons in the material.⁴

One outstanding question concerns how the absorption rate is measured – how do we know how many photons were absorbed? Perfect absorption spectroscopy would shine the beam clear through the sample, and measure the intensity of the beam before and after to determine the fraction of light absorbed. While *transmission measurements* like this are feasible with hard x-rays, the short attenuation length of soft x-rays would require prohibitively thin samples for any beam to be left on the other side. Instead, different measurements are used as a proxy for the total absorption rate:

Total Electron Yield

For the excited electron, the most probable decay mechanism is to quickly relax into a lower-energy state, transferring its energy to a more loosely bound electron in the process. This secondary electron, known as an Auger electron, can then be ejected from the sample – assuming it is close enough to the surface. The **total electron yield** (TEY) method determines the absorption rate by measuring the electric current that must flow into the sample to neutralize the ejected electrons and keep the sample uncharged. (Experimentally, this is done by simply connecting a wire to the sample holder, and placing a sensitive ammeter along the path to a solid ground connection.)

TEY measurements are difficult for some samples, either because an insulating sample doesn't allow current to flow in to replenish the ejected electrons ("sample charging"), or because electrons ejected deep in the material are reabsorbed elsewhere. This makes TEY measurements most sensitive to absorption events near the surface ($\sim 2\text{nm}$), and restricts them to conductive samples.

⁴To be accurate, we should say the '*partial* density of unoccupied states', since the vacancy left behind in the original electron state ("core-hole") will affect the energy of the unoccupied states.

Total Fluorescence Yield

Total Fluorescence Yield (TFY) measurements overcome these problems by using a light-sensitive detector near the sample. Although several orders of magnitude less probable than the Auger decay process, excited states can also relax by emission of a photon. Instead of ejected electrons, TFY measures the intensity of all photons emitted during the decay, which makes it applicable to both insulating and non-insulating samples. Because photons have a greater escape depth than electrons, this technique is also able to probe deeper within a material than TEY can. Due to the low probability of fluorescence transitions compared to Auger transitions (several orders of magnitude), TFY measurements benefit greatly from concentrated samples and a light source which is capable of high intensity.

2.1.2 Emission spectroscopy

While absorption measurements provide information about the *unoccupied* states, we can also study what happens *after* the initial photon is absorbed. When a core-level electron is promoted by the absorption of a photon, it leaves behind a “core-hole”, and the atom (or molecule, or crystal) is left in an excited state. While there are many ways for the system to collapse back to the ground state, there is a small probability that some valence-band electron will decay to fill the core-hole by the emission of another photon. Since the energy of the emitted photon will match the energy difference between that valence electron and the core level, the intensity distribution of *all emitted light* will correspond to the probability of finding electrons in the valence band at those energies. Therefore, if we could collect the *fluorescence* emitted from the sample and plot its intensity as a function of energy, we would have a measure of the *density of occupied states* for electrons in the material. In this way, emission spectroscopy provides information on the bound electronic states, which is not present in the absorption spectrum.

Experimentally, XES measurements are done by illuminating the sample with a fixed photon energy above the absorption edge. The fluorescence is captured using an energy- (or wavelength-)sensitive detector which is tuned to the energy range just below the absorption edge. Over time, an intensity spectrum is built up from the collected photons (Figure TODO). Since fluorescence transitions are a random process, and highly improbable compared to other decay mechanisms like Auger decay, XES measurements require a sufficient exposure time to build up good statistics. They also benefit greatly from a high-intensity beam source and an efficient detector – such as a sensitive spectrometer with high-efficiency gratings.

TODO Figure: XES process

Resonant Inelastic X-ray Scattering (RIXS)

An advanced form of XES is known as RIXS (*Resonant Inelastic X-ray Scattering*). Instead of exciting a sample with a photon energy well above the absorption edge, the energy of the beam is tuned to match transitions previously identified in the absorption spectrum (or stepped incrementally through this range).

This allows the experimenter to preferentially excite into specific electronic states: at *resonance*, the transition probability will be extremely high because the exciting photon energy exactly matches the transition energy and the emitted photon energy.

RIXS is a one-step process, but it can be explained mathematically as a simultaneous two-step process which combines absorption and emission: from the initial electronic state, an incoming photon is absorbed, creating a “core-hole” and an excited electronic configuration. This intermediate state decays by the emission of another photon into a final state, and this transition doesn’t necessarily need to involve the original electron. The difference in energy of the emitted and incident photons provides an *energy-loss spectrum* describing the nature of excitations within the material.

According to this two-step explanation, RIXS can probe transitions that would be forbidden by the dipole selection rule. For example, a 2p electron could be excited into a 3d state, and another 3d electron with a slightly different energy could collapse to fill the 2p hole, thereby effectively creating of a ‘d-d’ excitation [5].

2.1.3 Importance of Soft X-ray Spectroscopy (SXS)

Soft x-ray spectroscopy is a valuable tool in material science for its ability to gain insight into the electron environment within a material. Since the electronic structure determines the bonding between atoms and thereby a material’s mechanical, chemical, and physical properties, this is a big deal indeed. Additionally, x-ray spectroscopy has a few complementary advantages over other analytical techniques like neutron diffraction and photoemission spectroscopy:

- It is **element-specific**: for a material containing a number of elements, it is usually possible to find absorption edges for each element that do not overlap with the others, making it possible to independently probe the bonding environment of each. For example, in an organic sample containing carbon, nitrogen, and oxygen, one can probe the oxygen using the O 1s absorption at 543 eV, and then separately excite the nitrogen 1s electrons at 410 eV.
- More than being just element-specific, it is also **site-specific**: soft x-ray spectra make it possible to distinguish, for example, single-bonded carbon atoms at one location in a molecule from double-bonded atoms at another.
- Depending on the detection technique, it can be **surface-sensitive** or **bulk-sensitive** (i.e.: it can probe through surface contamination or oxidation, testing the nature of the material below).

Additionally, there are a few experimental considerations which make SXS desirable:

- It can be done **non-destructively** on whole samples, without having to crush them into powders, dilute them in solution, etc. It can also allow in-situ measurements of samples created directly within the vacuum chamber – for example, crystal samples created using sputtering or vapour deposition techniques.

- Because of the high brightness and small size of synchrotron beams, it can be done on **very small and thin samples**. Since the penetration depth of soft x-rays is so short, the interaction volume created by the beam will be tiny regardless of the sample thickness, making it a very useful characterization technique for thin film samples and even monolayers.

One obvious experimental disadvantage is that these techniques require access to synchrotron accelerators to produce the soft x-ray beam, which – for the foreseeable future – are not yet available in convenient desktop or bench-top models. Additionally, since soft x-ray experiments must be performed under ultra-high vacuum (UHV) conditions (see section 2.2.3), samples must either be UHV-compatible or carefully isolated from the vacuum environment behind thin windows.

Despite these limitations, SXS techniques have created some notable and very interesting discoveries in physics; some highlights are listed here:

- In 1990, de Groot et. al. presented the first comprehensive understanding of soft x-ray absorption in transition metal compounds. Not only did they produce some state-of-the-art experimental spectra for the time, but they also gave a thorough interpretation of them using crystal field atomic-multiplet theory [6].
- Butorin et. al. published the first RIXS studies of transition metals, and discovered *d-d* excitations in manganese oxide [5].
- Recently, Braicovich et. al. used RIXS to measure the dispersion of magnetic excitations in cuprate superconductors. This study also found a magnetic dispersion branch that had never been found before using neutron scattering, and found that these types of materials are in non-homogenous spin states, revealing a bit more about the mysterious nature of cuprate superconductors [4].
- With the proper experimental equipment, RIXS studies can also be done on gaseous samples. In 2011, Pietzsch et. al. measured very high resolution RIXS on oxygen gas (O_2) to observe the vibronic structure. The exciting result from this study was the presence of spatial quantum beats in their spectra – essentially, an observation of quantum mechanical interference like the famous double-slit experiment, but using excitations into different states instead of transmission through different slits [23].

2.2 Spectroscopy Instrumentation

The preceding sections make it clear that to perform soft x-ray spectroscopy experiments, we need three capabilities:

1. Obviously, one needs a source of soft x-rays – typically, the brighter, the better. This became possible with the advent of synchrotron particle accelerator facilities, which emit broad-spectrum x-rays as

relativistic electrons are forced to change their path by bending magnets.⁵

2. For absorption and emission spectroscopy:

From this broad spectrum of light, one needs to produce a nearly monochromatic beam of light to shine onto the sample, and must be able to adjust the energy of this beam. This is the role of a *monochromator*, which takes a broad-spectrum light source and extracts a small range of wavelengths from it (Figure 2.2).

3. Additionally, for emission spectroscopy:

One must be able to capture the light emitted from the sample and resolve it by wavelength. The end goal is to measure the relative intensity as a function of wavelength (or energy); this is accomplished using a *spectrometer* (Figure 2.4).

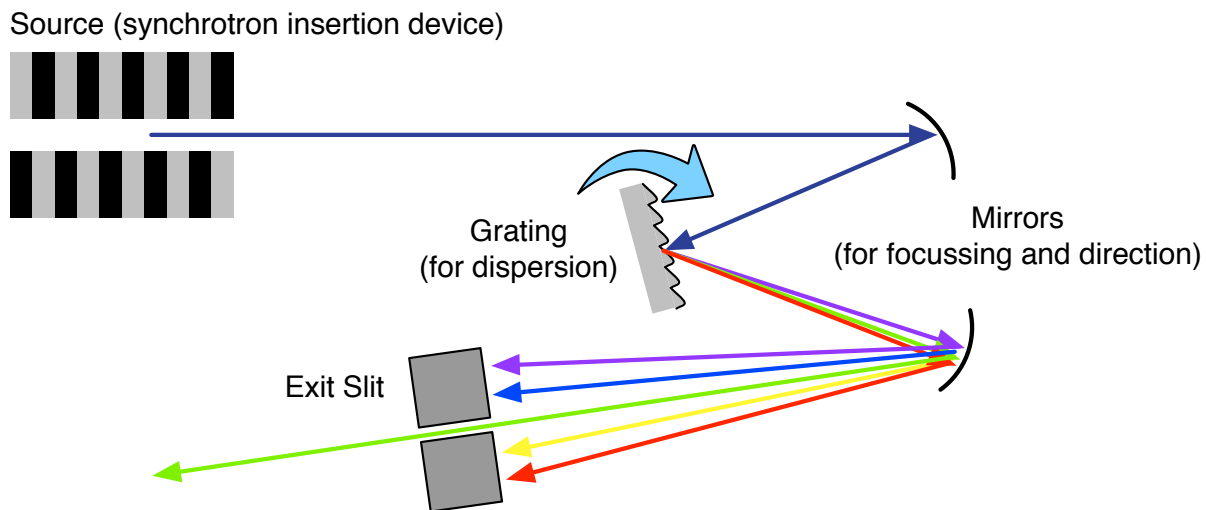


Figure 2.2: In this schematic of a grating monochromator, light from the source is focussed by mirrors and dispersed by the grating. An exit slit picks out the desired wavelength or energy range, and blocks the remaining light. Depending on the design, the output wavelength can be adjusted by changing the angle of the grating, the angle of the mirrors, and/or the position of the exit slit. (The resolution – the energy bandwidth of the outgoing light – depends on the dispersion of the grating, the geometry, and the size of the exit slit. An ideal monochromator would produce truly monochromatic light, but this would require an infinitely small slit.)

⁵Much more intense synchrotron light can be generated by “insertion devices” known as *undulators* and *wigglers*, in which an alternating array of magnets in a straight section of the accelerator forces the electron beam to bend many times over a distance of a few meters. Although light from insertion devices still contains a range of wavelengths, its spectrum consists of sharp intensity peaks which can be adjusted to the desired wavelength by changing the strength of the magnetic field. We intentionally avoid going into too much detail on synchrotron physics in this thesis; more information can be found in Ref. [19].

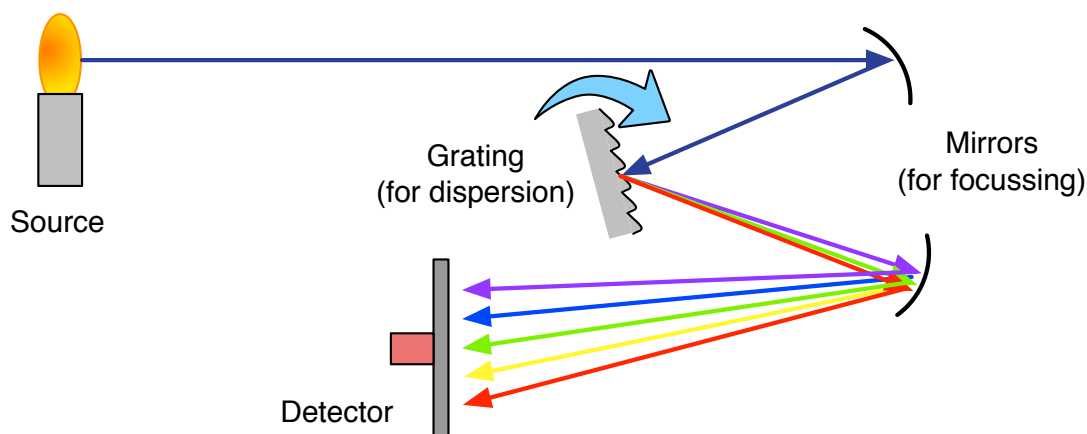


Figure 2.3: In this schematic of a grating spectrometer, mirrors are used to focus light from the source (or entrance slit) onto the detector, passing over a plane grating en-route to disperse the light by wavelength. (This is a *Czerny-Turner* arrangement, typical of compact visible-light designs like the one in Figure 2.1.) Since the grating diffracts different wavelengths at different angles, the intensity distribution across the detector surface creates a spectrum related to the wavelength (or photon energy).

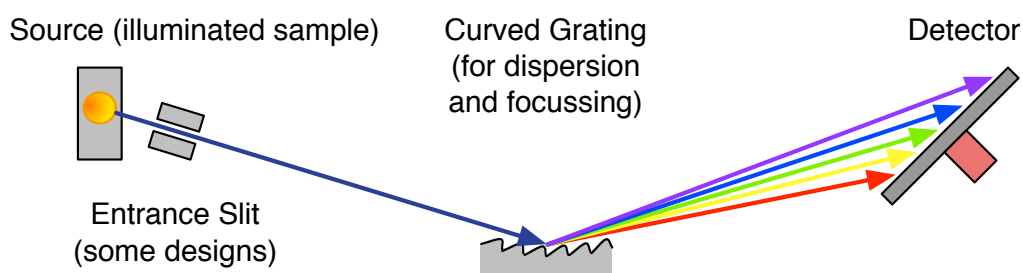


Figure 2.4: The spectrometer in this schematic uses a curved grating to both disperse light by wavelength, and focus it onto the detector. (This is typical of soft x-ray designs where the poor reflectivity of additional mirrors is usually avoided.) The intensity distribution along the surface of the detector can be converted into a spectrum with respect to wavelength or energy. Since the detector only captures a limited range of outgoing angles, it can be moved to pick out the desired wavelength window for each measurement.

2.2.1 Beamline optics: Monochromators and Spectrometers

Monochromators

The role of a monochromator (shown schematically in Figure 2.2) is to pick out a narrow range of wavelengths from a chromatic light source, and deliver the monochromatic beam to the experiment. For infrared light out to soft x-rays, diffraction gratings provide the most efficient way of separating the incoming beam based on wavelength.⁶ When the incidence angle and mounting angle of the grating are chosen to direct a single ($n \neq 0$) diffraction order toward the exit slit, the wavelength term in the grating equation (equation 3.61)

$$n\lambda/d = \sin \theta_{2,n} - \sin \theta_2$$

creates a dependence on the sine of the outgoing angle $\theta_{2,n}$, so that shorter wavelengths leave more normal, and longer wavelengths leave at more grazing angles. Depending on the optical and mechanical design, the output wavelength can be selected by changing the angle of the grating, the angle of the mirrors (and hence the incidence angle onto the grating), and/or the position of the exit slit.

The resolution of the monochromator – ie: the bandwidth of wavelengths present in the output light – depends on the angular dispersion of the grating, the geometry, and the size of the exit slit; an ideal device would obviously produce a perfectly monochromatic beam, but this would require an infinitely-small exit slit. (In practice, the size of the exit slit is used to adjust the resolution, in an unavoidable trade-off against the amount of flux produced.) Resolution is measured as the energy bandwidth ΔE (full width at half-maximum) for a given central energy; for example: $\Delta E = 500$ meV at 1000 eV. Often it is more convenient to normalize it as the *resolving power* $RP = E/\Delta E$, which has the benefit of being identical when measured in wavelength as well:

$$RP = \frac{E}{\Delta E} = \frac{hc/\lambda}{\Delta\lambda dE/d\lambda} = \frac{hc/\lambda}{\Delta\lambda (-hc/\lambda^2)} = \frac{\lambda}{-\Delta\lambda} \rightarrow \frac{\lambda}{\Delta\lambda} \quad (2.1)$$

In addition to dispersing the light by wavelength, monochromators must also act to *focus* light from the source, typically onto the exit slit, or onto the focal point of a downstream mirror. The schematic shown in Figure 2.2 is a *plane grating monochromator (PGM)*, where the focussing is accomplished using the two curved mirrors. Other designs use either a curved grating (*spherical grating monochromators*), or subtly change the line spacing of the grooves (*variable line space (VLS) grating monochromators*) to create the required focussing effect and reduce the number of optical elements. We avoid going into detail on focussing and monochromator design here; a good reference is provided in Ref. [19].

Our efficiency calculations in the rest of this thesis assume plane gratings and uniform line spacing; however, when curved gratings are used, the radius of curvature is typically so large – on the order of 10m – that the local changes over a grating surface (a few cm) do not affect the efficiency. With VLS gratings,

⁶For hard x-rays, monochromators use “natural” diffraction gratings consisting of atomic planes in blocks of single crystals, since the inter-atomic spacing is comparable to the short wavelength of the light; these might be analyzed more appropriately using Bragg scattering theory than the electromagnetic approach we take for the man-made structures in this thesis.

the groove spacing may change by a few percent from end-to-end, and we have modelled these situations by averaging the results of multiple efficiency calculations using a set of representative points.

Figure 2.5 is a diagram of a plane grating monochromator, designed by Petersen for the HE-PGM-3 beamline at BESSY [20], which became the basis for many soft x-ray beamlines. Many designs offer multiple switchable gratings to let the user optimize between efficiency and resolution, since higher line density gratings are required to maintain the resolving power at higher energies. (As we will show in Chapter 4, the grating efficiency declines as both the line density and energy increase.) This one use a 366 line/mm grating to cover the energy range between 30 eV and 700 eV, a 1221 line/mm grating to cover the energy range between 120 and 1900 eV.

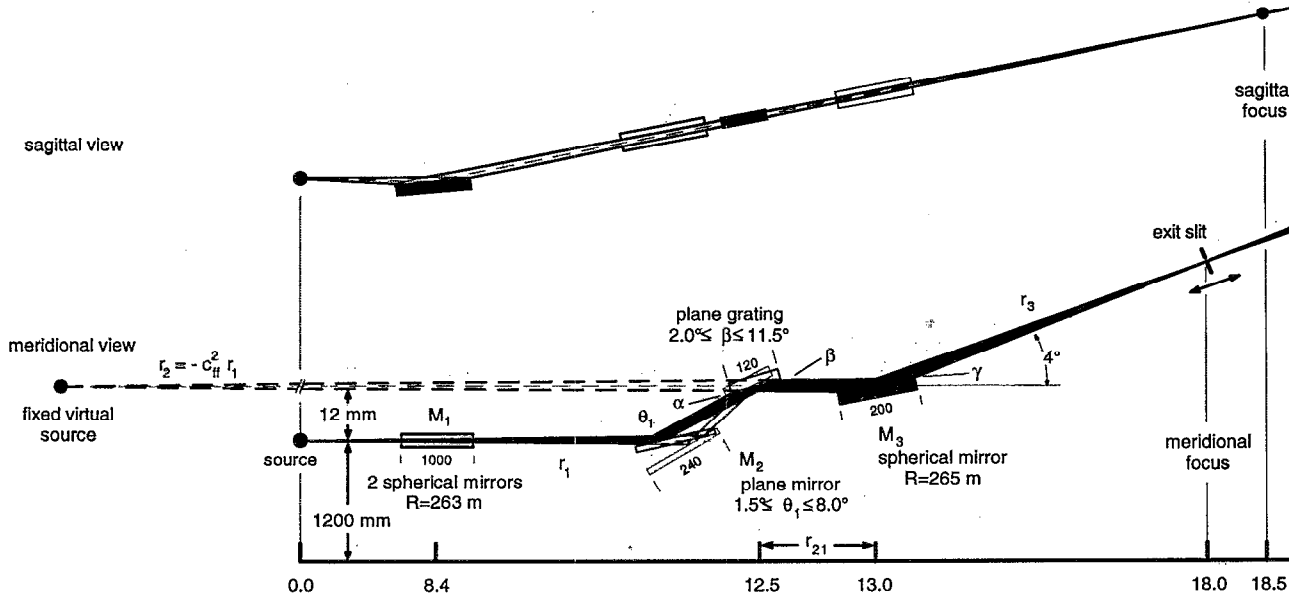


Figure 2.5: The Petersen Plane Grating Monochromator, as implemented on the HE-PGM-3 beamline at BESSY. In Ref. [20], Petersen et. al. provide a good overview of monochromator focussing techniques, prior to the widespread adoption of VLS designs. **Image from:** [20].

Spectrometers

If the goal of a monochromator is to produce monochromatic light, the goal of a spectrometer is to produce a *spectrum* – ie: to resolve the frequency components that exist in an unknown light source and measure their relative intensity. The device in Figure 2.3 is identical to the monochromator shown in Figure 2.2, except that the exit slit has been replaced by an area-sensitive detector. With the grating positioned so that an outgoing diffraction order (typically the 1st order, for best efficiency) lands on the detector, the angular dependence on wavelength puts short wavelengths onto the top of the detector, and long wavelengths onto the bottom of the detector. The intensity profile recorded across the detector surface is a spectrum, although some mathematical correction will need to be done to calibrate the energy axis, by mapping detector positions to diffraction angles, and diffraction angles to energy using the grating equation.

The spectrometer in Figure 2.4 is more representative of those used in soft x-ray applications, where the low initial levels of fluorescence from the sample and the poor reflectivity of mirrors make it desirable to eliminate as many optical components as possible. Just like monochromators, spectrometers must focus light from the entrance slit – or directly from the source, in the case of slit-less designs – onto the detector. This is accomplished by using spherical gratings and arranging the geometry to exploit the *Rowland Circle* focussing condition discovered by Henry Rowland [19, p. 169], or again by using VLS gratings to alter the shape of the focal curve. More information on spectrometer focussing can be found in the M.Sc. thesis by David Muir [17].

Like monochromators, spectrometer designs usually offer switchable gratings with different line densities and coatings, optimized for different energy ranges as we show in Chapter 5. Figure 2.6 shows a top and side view of the SXF endstation on Beamline 8.0.1 of the Advanced Light Source, a typical “workhorse” spectrometer, which balances moderate resolution with reasonable efficiency. It uses four gratings with groove densities of 600, 1000, and 1500 lines/mm to cover the energy range from 70 to 1200 eV, and uses a 40 mm wide multi-channel plate detector with an effective spatial resolution between 40 and 80 μm . Figure 2.7 shows an image recorded by that detector, and the corresponding spectrum.

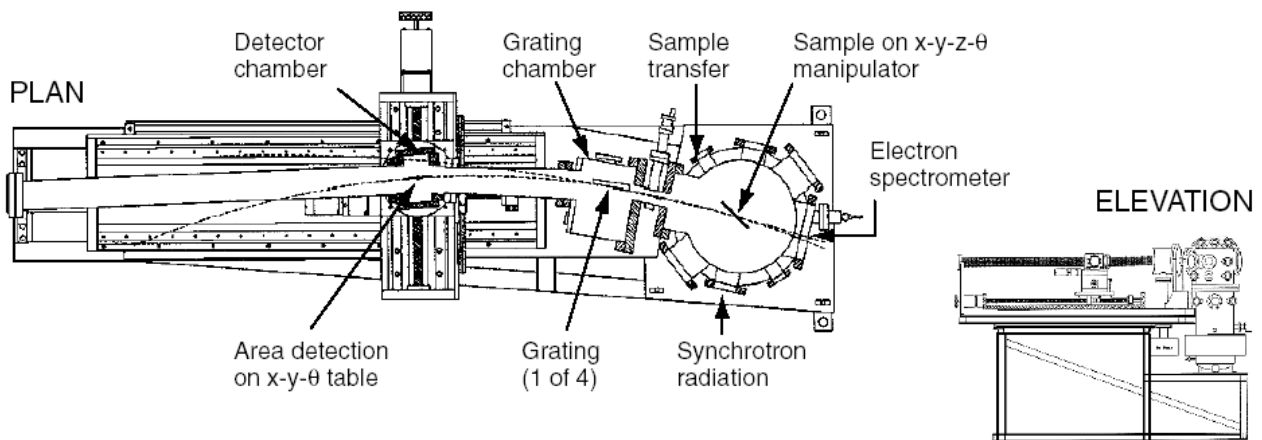


Figure 2.6: The SXF endstation spectrometer on Beamline 8.0.1 of the Advanced Light Source – a typical “workhorse” spectrometer. It uses spherical gratings in a Rowland Circle design; four gratings let users choose between higher resolution or higher efficiency at different energy ranges. The resolving power of this machine is compared with other leading spectrometers in Figure 5.1. **Image from:** [12]

2.2.2 Goals for Soft X-ray Instruments

In the design of both spectrometers and monochromators, there are two goals we have already mentioned that are important from the experimenter’s perspective:

- The **resolution** is important in order to see details in spectra and probe new science. On a soft x-ray beamline, the monochromator determines the resolution of an absorption scan, and the spectrometer

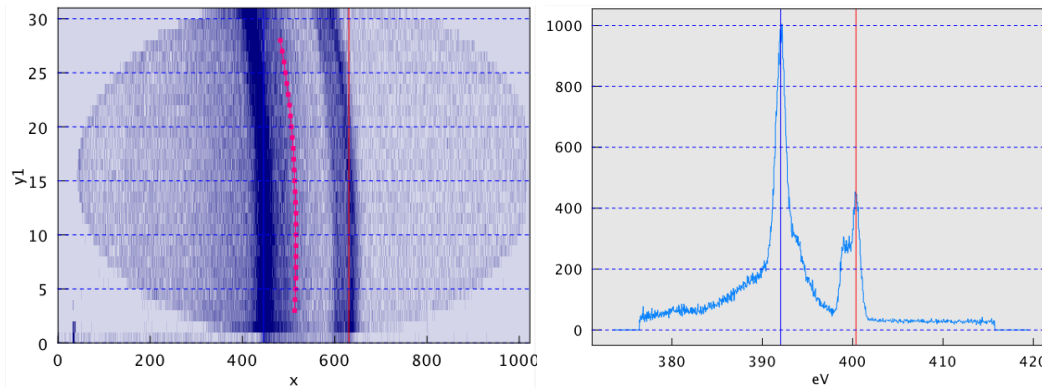


Figure 2.7: A detector image and corresponding spectrum produced by the SXF spectrometer in Figure 2.6. (This particular scan is of the nitrogen emission lines in nitrogen-doped zinc oxide.) The curvature of the spherical gratings provides focussing in the dispersion direction (x -axis), but unfortunately produces a curved image in the perpendicular direction (y -axis). This curvature is corrected by aligning rows along the red curve when the image is summed to produce the spectrum on the right.

determines the resolution of an emission scan. Both are involved in the experimental resolution of RIXS studies.

- The overall **efficiency** is important because it determines how much light is available, and indirectly how long it takes to generate enough photon interactions to record acceptable statistics. At a minimum, the efficiency must be high enough to produce a signal above the background noise level of the detector. Beyond this threshold, increases in efficiency make it faster to do experiments and let the user accomplish more science in their shift.

Since the probability of an excited atom decaying via fluorescence transitions is so low compared to other decay methods, the initial amount of light available in emission experiments is extremely low. This is further compounded in experiments on doped or dilute samples, when trying to observe the emission lines of the dopant elements. Finally, the entrance slit of a spectrometer can only capture a tiny geometric fraction of all photons out of the sample. All of these reasons combine to make emission spectroscopy experiments extremely “photon hungry”, which means that efficiency is especially critical here.

What makes these two goals challenging is that they are inherently in tension. To see why, we consider as an example a simple emission spectrometer like the one shown again in Figure 2.8.

The immediate result of a spectroscopy experiment is the image produced along the detector surface. For all detectors – be they photographic film, multi-channel plate detectors, or CCDs – there is an *effective spatial resolution*: the minimum distance along the detector that is required for two adjacent rays to be distinguished. For a given detector, if you wanted to increase the *energy resolution*, you would want to either

1. increase the angular dispersion of the grating – thereby increasing the angular separation between adjacent wavelengths, or

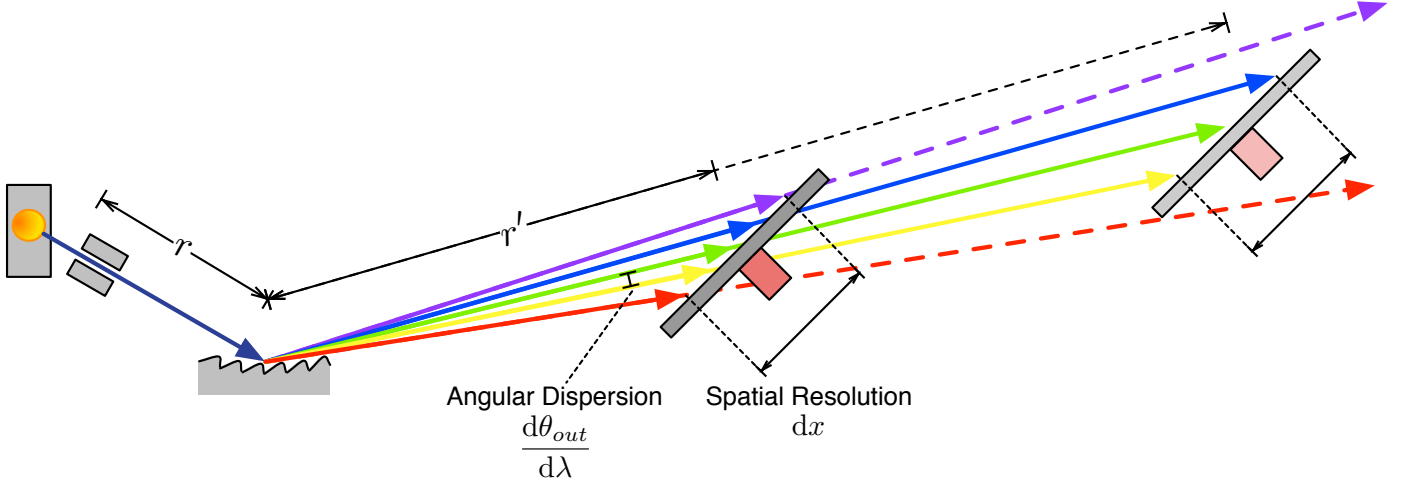


Figure 2.8: The detector has an effective spatial resolution dx which is the minimum distance required to resolve two adjacent incident rays. Except for the $n = 0$ order, the grating produces an angular dispersion $d\theta_{2,n}/d\lambda$, which is the angular separation between infinitesimally-adjacent wavelengths. To increase the spacing between adjacent wavelengths on the detector, we can either increase the grating-detector distance r' , or increase the angular dispersion.

2. you would want to put the detector a long way from the grating, so that over distance the angular dispersion creates a large spatial separation between adjacent wavelengths.⁷

Both of these solutions inherently reduce the *geometric efficiency* of the spectrometer: the fraction of all photons captured by the detector assuming perfect mirror and grating efficiency. In the dispersion direction (or *meridional* direction, vertical in Figure 2.8), the detector will now only capture photons from a smaller energy range; the corresponding reduction in light gathered is an unavoidable tradeoff no matter what scheme is used to increase resolution. However, the second method – increasing the distance from the grating to the detector – reduces the solid angle captured by the detector also in the perpendicular direction (or *sagittal* direction, out of the page), further decreasing the geometric efficiency to an extent which depends on the nature of focussing in that direction.⁸ The only way to increase resolution with only the minimum essential reduction in geometric efficiency is by using the first method: increasing the grating’s angular dispersion. By differentiating the grating equation (3.61) with respect to wavelength (holding the incident angle θ_2 constant):

$$\frac{n\lambda}{d} = \sin \theta_{2,n} - \sin \theta_2 \quad (2.2)$$

$$\frac{n}{d} = \cos \theta_{2,n} \frac{d\theta_{2,n}}{d\lambda} \quad (2.3)$$

$$\frac{d\theta_{2,n}}{d\lambda} = \frac{n}{d \cos \theta_{2,n}} \quad (2.4)$$

⁷This is why currently the world’s two highest-resolution emission endstations use 10 meter- and 50 meter-long spectrometers; see section TODO.

⁸A complete analysis of focussing criteria would show that, at least for Rowland Circle spectrometers, increasing the source-grating distance requires an increase in both the entrance slit-grating distance, *and* an increase in the grating radius; both of these actions further decrease the geometric efficiency, possibly as a function of the cube of the distance. One could compensate by using larger gratings, but the maximum grating size must be limited to manage spherical aberrations; see Ref. [17, p. 98].

we derive an expression for the angular dispersion; it is clear that to create more dispersion, we can either increase the groove density (decrease the groove spacing d), or use a higher diffraction order n . Unfortunately, as will be shown in Chapter 5, both of these actions substantially reduce the *grating efficiency*. As an additional challenge, we can see that the dispersion will be reduced for higher energies, which leave the grating at more normal angles, creating a larger $\cos \theta_{2,n}$.

No matter which method is used, resolution and overall efficiency are in conflict. Whether it is a hit to the grating or to the geometry, increasing the resolution demands a reduction in efficiency and vice-versa, the cleverness of the beamline designer being measured in his or her ability to negotiate this compromise.

While this example examined resolution as seen by a spectrometer detector, the same unfortunate principles apply to monochromators as well.

2.2.3 Challenges of Soft X-ray Applications

All grating spectrometers, regardless of their wavelength range, are subject to the unavoidable tradeoff between resolution and efficiency. However, the nature of soft x-rays adds an additional set of challenges within this regime, which combine to make efficiency even more important.

UHV Compatibility

Because the energy of soft x-ray photons matches the energy of core level electron transitions in all light elements, they are readily absorbed in matter over very short distances. (Just passing through 1 mm of nitrogen at atmospheric pressure is enough to attenuate a 200 eV beam by 63 percent!) For starters, this means that all SXS experiments must be done under *ultra-high vacuum* (UHV) conditions, where the beam path has been evacuated of air and other contaminants, ideally to a pressure lower than 10^{-8} torr. This is accomplished by using vacuum chambers and sealed beam pipes, pumped down using turbo-molecular pumps, ion pumps, and/or cryogenic pumps. At these low pressures, most common materials would “out-gas”, boiling off contaminants into the vacuum environment. As a result, chambers and instrumentation must be built using a restricted set of UHV-compatible materials (certain grades of stainless steel and aluminum, copper, gold, and some special ceramics and high-temperature thermoplastics). Anything that comes into contact with the vacuum environment must be carefully cleaned prior to assembly, and it is often necessary to “bake out” the chambers by heating them to temporarily raise the vapour pressure while pumping in order to remove water and other contaminants adsorbed to the inside surfaces before eventually attaining UHV levels.

For the experimenter, UHV requirements also apply to samples. Liquid samples and non-UHV-compatible samples must be carefully enclosed and sealed behind thin windows to let the beam in. (Beryllium is often used in this application, due to its strength and relatively low absorption). Loading samples into the vacuum chamber must be done through an airlock, and remote actuators are required to adjust the sample position and the position of optical elements.

Low Reflectivity and Grazing Incidence

Beamline designers face a more significant challenge when choosing optical elements. The easy absorption of soft x-rays means that mirror and grating surfaces have extremely low reflectivity at these wavelengths – at least at normal incidence. For visible light, the reflectivity of a polished aluminum surface approaches 90%; at 200eV, the reflectivity of the same surface is less than 0.005% [7].

Two approaches are necessary to work around this challenge. Optical coatings need to be selected to avoid absorption edges in the region of interest. For example, carbon and nickel have relatively high peak reflectivities (Figure 4.15), but very strong absorption features at 284 eV and 853 eV respectively; these coatings would only be appropriate for optical elements used within a narrow wavelength range away from those edges. In many-electron materials like gold and platinum, the most pronounced core-level absorption edges occur outside the soft x-ray region, and as result they have acceptable reflectivity over a wide bandwidth.⁹

Second, mirrors and gratings need to be aligned and used at *grazing incidence* – i.e., with the incident light striking them at glancing angles just a few degrees from parallel to their surface. At soft x-ray wavelengths, most materials have a refractive index with a real part *less than* one; the phase velocity of light is actually *faster* than it would be in a vacuum. This allows us to exploit the phenomenon of total internal reflection (TIR), except in this case it becomes a *total external reflection*, since the refractive index is higher in the grating material than it is in the vacuum above it. Just as with conventional TIR in glass and air, we can calculate a critical angle above which total external reflection will occur (see Section 4.3.6). For most metals, this turns out to be around 83 to 85 degrees from the surface normal.

2.3 REIXS spectrometer project

This thesis – and its motivation to establish a better understanding of diffraction grating efficiency – emerged from a primary engineering goal: to design and build a world-class emission spectrometer for the REIXS beamline at the Canadian Light Source. The REIXS (*Resonant Elastic and Inelastic X-ray Scattering*) beamline is optimized for material science experiments; it offers an elliptically-polarizing undulator to produce a high brightness beam of soft x-ray photons, and a high-resolution monochromator with a flux of $\sim 10^{13}$ photons/second and a resolving power greater than 5000. The beamline has room for two endstations; our task was to build the emission spectrometer, which will be used for inelastic scattering experiments, while a team from the University of British Columbia built the second endstation used for elastic scattering measurements.

Chapter 5 describes the design process and the resulting optical design of the spectrometer. Used in combination with the work of David Muir on spectrometer resolution [17], the ability to model grating

⁹Gold and platinum do have absorption edges in the soft x-ray range, but these correspond to outer shell electrons (for example, gold 4s electrons bound at 802 eV) instead of core-level electrons. The outer electrons see shielding by the inner ones, and therefore have a lower transition probability.

efficiencies allowed us to optimize the design for an intelligent compromise between these two competing goals. In the process, we discovered an efficiency peak in the 3rd order – typically assumed to be unusable – that prompted us to create an innovative design capable of reaching much higher resolution than would otherwise be possible given the space constraints of the beamline.

Figure ?? is a picture of the REIXS spectrometer as built, in August 2011.

(TODO picture)

2.4 Summary: Why Grating Efficiency Matters

Figure 2.9 lists a variety of soft x-ray spectroscopy techniques, and shows the number of gratings in the beam path to the detector for each. Of these techniques, those in *italic text* are possible on the REIXS beamline; the remaining are possible on other beamlines at the CLS. For all of these techniques, the ability to create more efficient gratings would increase the speed of experiments, improve the quality of data, and increase the minimum concentration of samples that can be feasibly studied.

Conversely, during the design phase of these kinds of instruments, the unavoidable tradeoff between resolution and efficiency implies that accurate predictions of the grating efficiency could ironically be used improve *resolution*: by deliberately sacrificing efficiency, designers could push their resolving power to the limit once the efficiency is known to be “good enough”.









	Photon In	Electron In
Electron Out	<i>Near-edge X-ray Absorption Fine Structure (NEXAFS):</i>  <i>electron yield</i>	Electron Energy Loss Spectroscopy (EELS)
	Extended X-ray Absorption Fine Structure (EXAFS):  electron yield	
	X-ray Photoelectron Spectroscopy (XPS) 	
Photon Out	<i>Soft X-ray Emission Spectroscopy (SXE)</i> 	<i>Inverse Photoelectron Spectroscopy (IPES)</i> 
	<i>Resonant Inelastic X-ray Spectroscopy (RIXS)</i> 	
	X-ray Excited Optical Luminescence (XEOL) 	
	<i>NEXAFS: fluorescence yield</i> 	

Figure 2.9: A variety of soft x-ray spectroscopy techniques, and the number of gratings required in the beam path to accomplish each one. Of these techniques, those in *italic text* are possible on the REIXS beamline using the emission spectrometer endstation. For all these techniques – and particularly those using two gratings – more efficient gratings would increase the speed of experiments, improve the quality of data, and increase the minimum concentration of samples that can be feasibly studied.

CHAPTER 3

THEORY: HOW TO CALCULATE GRATING EFFICIENCY

3.1 Introduction and brief history of grating theory

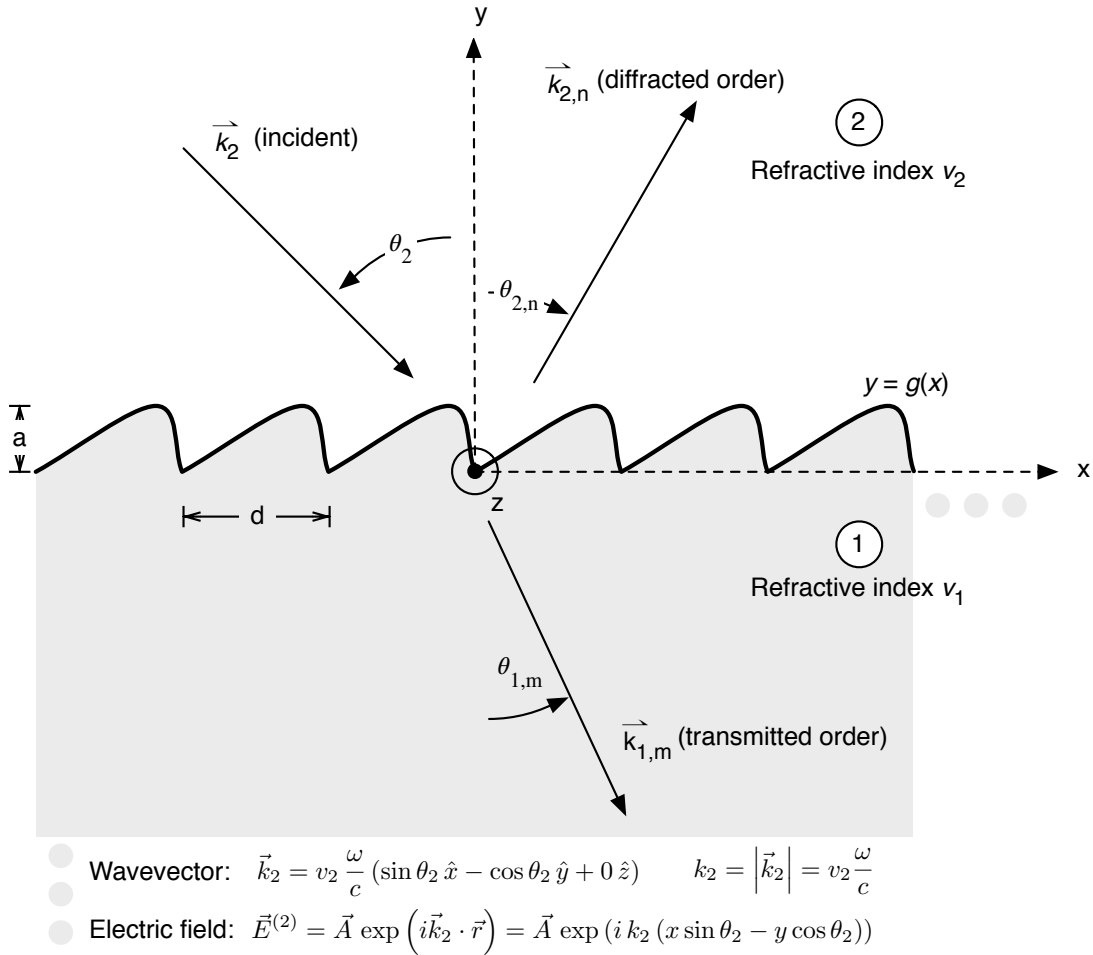


Figure 3.1: A one-dimensional grating with in-plane incidence.

For centuries, we have known that gratings reflect and transmit light into a set of discrete angles – called *orders* – where the angles depend on the wavelength (Figure 3.1). A variety of simple proofs have been used to explain this. In undergraduate books, the grating equation is introduced as a consequence of constructive

interference from a linear array of coherent emitters. (This makes sense for a slotted transmission grating, but it is less obvious why an arbitrarily-shaped periodic structure like one of those shown in Figure 4.5 would behave the same way.) Other proofs – such as those using Fermat’s Principle to minimize an optical path function with a phase offset introduced by the grating [19, p. 93 – 99] – are general enough to explain the existence of diffraction orders, but they do not say anything about how much light goes into each.

This is unfortunate, because to understand grating efficiency, we must understand the distribution of light into orders. In general, this requires finding the solution to Maxwell’s equations for the electric and magnetic fields of the light, in the presence of the grating’s periodic boundary conditions, for a known incident field. Prior to the availability of computers and numerical techniques, great efforts were attempted using analytical methods to answer this question. In 1907, Lord Rayleigh set up the problem¹ using a Fourier approach identical to the one we use later in this chapter [26]. However, without access to powerful numerical methods, he could only make coarse approximations, using expansions truncated at the first or second power of the groove height.² This led to some obviously non-physical results, such as predictions of infinite intensity in any order when the outgoing angle of a higher order reached exactly 90 degrees. From 1907 until 1960, advancements in grating theory amounted to finding clever but limited simplifications to these expansions, which would work for in the case of one particular groove profile, incidence angle, or approximation limit.

It is only within the last thirty years that mathematical techniques and computational power have advanced enough to accurately model the electromagnetic field of light within and around the surface of a grating, allowing us to actually determine how energy is distributed between the orders, and how much is absorbed within the grating. The introduction of computer-based numerical methods in the 1960s spawned a renewal of research into general solutions to the problem. The first “rigorous” algorithm³ was invented by several researchers in 1966, using Maxwell’s equations in integral form and the Kirchoff integral theorem [21][27][11]. It was generalized from perfectly conducting (i.e.: perfectly reflecting) gratings to finite-conductivity metallic gratings in an important paper in 1972 [15]. Alongside these “integral” methods, two other broad families of algorithms emerged based on Maxwell’s equations in differential form:

- the “modal” methods, which relate the electromagnetic field to a Fourier expansion in the vertical (y) direction with unknown coefficients, called modes. The total field satisfying the boundary conditions is solved algebraically as a linear combination of the modes. [2][3][1]
- the “differential” methods, which exploit the periodicity of the grooves to express both the grating boundary and the fields as Fourier expansions in the x -direction. The total field satisfying the boundary conditions is determined by numerically integrating a finite set of differential equations. (We explore

¹Actually, Rayleigh’s first application of this technique was to the diffraction of sound waves [25]. It turns out that the wave equation for a pressure wave in compressible media is the same as for the fields in an electromagnetic wave, and the boundary conditions at interfaces are also analogous. In Ref. [26] he shows applications to both sound and light.

²And this, despite assuming a perfectly reflecting grating, exactly normal incidence, and only one term in the Fourier expansion for the groove shape – i.e., a sinusoidal grating.

³“Rigorous” meaning a method that doesn’t introduce approximations into the theoretical equations, other than inevitably in the process of finite-precision numerical calculations.

the details of this method later in this chapter.)

The modal methods are not actually general because they require the edges of the grooves to be vertical; although limited to gratings with rectangular profiles⁴, they are accurate in this special case, and fast compared to the differential method because they avoid numerical integration. The other two approaches are general in representation, although the integral approach can only be solved for certain geometries. TODO CHECK.

By 1980, grating theorists had devised a wide variety of implementations for each family – after all, it is one matter to express the problem as a complete set of algebraic or differential equations; it is another matter to actually solve that set! Reference [] provides a comprehensive review of all the methods that were available by this date.⁵ Of the three families, the differential approach had proven to be the most general way of setting up the problem, but it ran into two numerical problems – particularly when used to describe TM-polarized light. One problem was strictly computational: round-off errors when doing finite-precision computer arithmetic would lead to ever-growing contamination during the numerical integration of exponential functions. This issue was solved by the introduction of the “S-matrix” propagation algorithm in 1996 [13][16]. The second problem was related to the mathematical implications of truncating an infinite Fourier series – unfortunately necessary for numerical calculations. This challenge was also finally resolved by the breakthrough work of Li [14] in 1996 on the factorization of truncated Fourier series, and has been applied extensively by Neviere and Popov [24][18].

This chapter lays the groundwork for a full electromagnetic theory describing the interaction of light waves with periodic structures. The notation presented here is consistent with the notation used by Neviere in []. However, before diving into the details of the mathematics, it might be useful to summarize the basic physical principles behind the solution:

1. The theory starts by using the Maxwell equations to derive a 2nd-order wave equation for the electric and magnetic field of the light. According to classical optics, the incoming light can be divided into two independent polarization components; the “Transverse Electric” (TE) component has its *electric* field vector always parallel to the z -axis in Figure 3.1, and the “Transverse Magnetic” (TM) component has its *magnetic* field vector always parallel to the z -axis. Due to the beautiful symmetry of the Maxwell equations, it turns out that the wave equation for the electric field in TE polarization is the same as the equation for the magnetic field in TM polarization, and for most of the theory we can use the same mathematics to work with both, referred to as the “general field” or just “the field”.⁶ Because the TE

⁴We can attempt to avoid this limitation by using stacks of thin rectangular gratings to represent an arbitrary shape, as we will see in Section 3.3.3. Unfortunately, this approximation leaves sharp edges and sharp corners at every layer, which cannot be physically representative of the electric field near a smooth grating; we discuss this more in Section 4.1.1

⁵The same author provides a follow-up paper, written ten years later on new methods that differ completely from the fundamentals used in 1980 [22].

⁶While the wave equation is the same for both the TE electric field and the TM magnetic field, the boundary conditions for the fields at the grating interface are different and need to be handled separately. This is responsible for the difference in efficiency dependent on polarization.

and TM polarizations are independent, we can solve the grating problem for both separately, and then combine the diffracted field solutions in proportion to the polarization of the incident light.

2. Because the grating is periodic, we use Fourier series expansions in the horizontal direction to express both the permittivity of the grating material, and the field itself. In the vertical direction, there are three distinct regions:

- Region 2: above the grooves, where the refractive index is uniform ($v = v_2$);
- Inside the grooves – the “modulated region” – where the refractive index changes as a function of the x and y position: it is either v_1 or v_2 ;
- Region 1: below the grooves, inside the grating substrate, where the refractive index is again uniform ($v = v_1$).

3. Above and below the grooves:

By using the grating as a periodic operator and applying boundary conditions for the field at infinite, we can prove that light is reflected and transmitted at discrete angles, and that a Fourier sum of plane waves known as the Rayleigh Expansion can be used to express the total field which satisfies the wave equation in this region. Each propagating plane wave corresponds to a diffraction “order”, and once we know the angle of the incident light, we can determine the angles of the diffraction orders (Figure 3.2). At this point, the Rayleigh expansion still has unknown coefficients, and we need to determine these coefficients to find out how much energy is diffracted into each order.

4. Within the grooves:

However, the field within the grooves depends on the exact shape of the groove profile and the interaction of light within the material. It cannot be simply represented as a sum of plane waves, and the boundary conditions are complicated. There are two leading methods used to handle this. Both express the wave equation using Fourier expansions for the field and for the grating permittivity. (These expansions would theoretically be infinite sums, therefore they need to be truncated to be approximated using computer calculations. Special rules apply for accurately calculating the products of truncated Fourier series, discovered by Li in (TODO ref).)

- (a) In the “Rigorous Coupled Wave” (RCW) approach, the grating groove shape is sliced into thin layers (Figure 4.1) and approximated with vertical walls between layers (the “staircase approximation”). This simplifies the boundary conditions, so that at every layer the wave equation can be converted into a set of simultaneous linear equations and solved algebraically. The effect of each layer on the field is propagated to the next using matrix methods.

This approach is computationally efficient, and has been known to work accurately in TE polarization. However, in TM polarization, the results often do not match experimental measurements,

because the staircase approximation introduces sharp corners and artificially large electric field components at the step boundaries.

- (b) In the “Differential Method” approach, we numerically integrate the wave equation many times using different assumed initial values, to generate a complete orthogonal set of particular solutions. Then we use techniques of linear algebra to solve for the coefficients of the general solution that satisfy the boundary conditions along the grating interface.

5. Finally, most common grating structures consist of one (or often many) stacked layers⁷ (Figure 3.4). In classical optics, the *reflection matrix* and *transmission matrix* are conveniently used to propagate an incoming field through an optical layer. We can generalize this concept to gratings by defining a matrix which maps the Rayleigh coefficients of the incident field to the coefficients of the field that is reflected and transmitted by each layer. The matrices for each layer can then be multiplied together to find the effect of the complete grating; this is known as the “T-matrix” approach. While theoretically sound, the T-matrix becomes unstable in computer calculations because rounding errors introduce instability into diverging exponential functions. An alternative formulation called the “S-matrix” approach defines a matrix at each layer which represents the cumulative effect of *all layers below and including that layer* on the incident field; by definition, this matrix remains bounded and is safe to use for numerical calculations.

3.1.1 Simplifying Assumptions

Before we tackle the mathematics of grating theory, this section defines the geometry and terminology we’ll use throughout this text, and introduces some assumptions that simplify the problem. Figure 3.1 shows a side view of a reflection grating, in the following situation:

1. The mean surface of the grating is in the $x - z$ plane, with the grooves running parallel to the z -axis. The groove profile is periodic and repeats every distance d along the x -axis.
2. The grating is illuminated with a light ray travelling parallel to the $x - y$ plane (i.e.: within the plane of the page). This is referred to as “in-plane incidence”, and is typical of how most monochromators and spectrometers are used. (When the incident ray has a component in the z -direction, the diffraction peaks end up dispersed over the surface of a three-dimensional cone, and this is referred to as “conical mounting”.)

These first two simplifications reduce the grating problem to two dimensions, since the whole system is unchanged by translation along the z -axis.

Additionally, we assume that:

⁷For example, dielectric gratings with a metal coating used for soft x-ray beamlines, gratings with thin-film multilayer coatings, etc.

1. The incident light can be represented as a plane wave, infinite in extent.
2. The grating also stretches forever in the x - and z -directions.

Typical gratings used in soft x-ray devices are much much larger (typically: 40 mm) than their groove spacing d (typically: a few μm). As long as they are illuminated with collimated light having a beam width much larger than the groove spacing, both of these assumptions seem reasonable.

Finally, to simplify the electromagnetic field calculations, we assume that

1. The grating material is non-magnetic, with a permeability of μ_0 .
2. The dielectric constant ϵ of the grating material is the same in all directions.

(These last two assumptions are also necessary to keep us within a two-dimensional problem. If the material is non-isotropic, then the dielectric constant ϵ becomes a tensor $[[\epsilon]]$ and the problem requires a full 3D analysis.)

These assumptions make the grating theory much simpler to present in this chapter. However, it should be noted that at the expense of larger matrices and higher mathematical complexity, it is possible to express the same theory in the full three-dimensional case, which enables the analysis of exotic situations like conical mount gratings, crossed 2D gratings, and non-isotropic materials. [Ref: Neviere Ch. 5] provides a derivation of the full general 3D version.

As one final assumption, we assume that the grating surface exactly matches the periodic profile given by $y = g(x)$ in Figure 3.1. For real-world applications, this turns out to be the most limiting assumption, since actual gratings will vary from groove to groove due to imperfections in the manufacturing process, and their ideally smooth surfaces will have an unavoidable amount of random microroughness. Unfortunately, this assumption is necessary for any mathematical treatment; in Section 6.3 we look at the impacts of real-world imperfections on grating efficiency.

A few brief notes on notation:

- Quantities that change depending on the grating region are subscripted to indicate which region they are in. For example, k_2 and v_2 designate the wave vector and refractive index, and $\theta_{2,n}$ the angle of the n -th order ray, in Region 2 above the grating. Eventually, we will tackle layered gratings with many numbered regions, and the subscript convention will become very helpful.
- Angles are measured from the surface normal as shown in Figure 3.1. There are two different sign conventions in common use; we will use positive angles for both the incident ray (θ_2) and the diffracted ray ($\theta_{2,n}$) when they are on opposite sides of the surface normal. Transmitted rays ($\theta_{1,n}$) are also measured using positive angles from the $-y$ axis, as shown in Figure 3.1.⁸

⁸The sign convention for diffraction angles affects the sign in the right-hand side of the grating equation (3.61). In North American literature it is more common to measure all angles positive counter-clockwise from the surface normal; this creates a ‘+’ rather than a ‘−’ in the grating equation.

3.1.2 Electromagnetic field and polarization

In Figure 3.1, incoming light strikes the grating along wavevector \vec{k}_2 at an angle θ_2 from perpendicular to the grating plane.

$$\vec{k}_2 = v_2 \frac{\omega}{c} (\sin \theta_2 \hat{i} - \cos \theta_2 \hat{j} + 0 \hat{k}) \quad (3.1)$$

(We use v to designate the refractive index – in this case, in Region 2 above the grating, which is normally air or vacuum. $\omega = 2\pi f$ is the angular frequency of the light, and c is the speed of light in vacuum.)

The incoming light is a travelling electromagnetic plane wave with sinusoidal dependence on time. We can express the electric field vector using the complex exponential form:

$$\vec{E}_{incident} = \vec{A} \exp(i(\vec{k}_2 \cdot \vec{r} - \omega t)) = \vec{A} \exp(i k_2 (x \sin \theta_2 - y \cos \theta_2)) \exp(-i\omega t) \quad (3.2)$$

where the true (physical) field is contained in the real part. Since all fields will have the same harmonic dependence on time, we drop the $e^{-i\omega t}$ factor from here on. (The scalar k_2 is simply the magnitude of \vec{k}_2 , i.e.: $|\vec{k}_2| = v_2 \omega / c$.)

The electric field vector is always perpendicular to the direction of the wave \vec{k}_2 , but can have an arbitrary polarization determined by \vec{A} . This can always be expressed as a superposition of two orthogonal components:

- The TE (transverse electric) polarization represents the component of the electric field vector parallel to the z axis (i.e.: into the page). For a pure TE wave, the E_x , E_y , and B_z fields are always 0.
- The TM (transverse magnetic) polarization represents the component of the electric field vector in the $x - y$ plane (i.e.: the *magnetic* field vector is along z). For a pure TM wave, the E_z , B_x , and B_y fields are always zero.

In general, the grating problem will be solved by applying the Maxwell equations to the incident electric field, according to the boundary conditions imposed by the grating. By solving it separately for each polarization case (TE and TM), we can simplify these equations. In the end, we can superpose the results we calculate for the outgoing fields, weighted based on the actual polarization of the incident light.

3.1.3 Maxwell's equations for sinusoidal time-varying fields

Our assumptions in Section 3.1.1 mean that the gratings are not loaded with free charge, or carrying free currents. Therefore, two relevant Maxwell equations are:

$$\nabla \times \vec{E} = -\frac{\partial \vec{B}}{\partial t} \quad (3.3)$$

$$\nabla \times \vec{B} = \mu\epsilon \frac{\partial \vec{E}}{\partial t} \quad (3.4)$$

For sinusoidal time-varying fields, the electric field \vec{E} is proportional to $e^{-i\omega t}$, so the time derivatives reduce to:

$$\nabla \times \vec{E} = i\omega\mu\vec{H} \quad (3.5)$$

$$\nabla \times \vec{H} = -i\omega\epsilon\vec{E} \quad (3.6)$$

or, expressed in Cartesian coordinates:

$$\frac{\partial E_z}{\partial y} - \frac{\partial E_y}{\partial z} = i\omega\mu H_x \quad (3.7)$$

$$\frac{\partial E_x}{\partial z} - \frac{\partial E_z}{\partial x} = i\omega\mu H_y \quad (3.8)$$

$$\frac{\partial E_y}{\partial x} - \frac{\partial E_x}{\partial y} = i\omega\mu H_z \quad (3.9)$$

$$\frac{\partial H_z}{\partial y} - \frac{\partial H_y}{\partial z} = -i\omega\epsilon E_x \quad (3.10)$$

$$\frac{\partial H_x}{\partial z} - \frac{\partial H_z}{\partial x} = -i\omega\epsilon E_y \quad (3.11)$$

$$\frac{\partial H_y}{\partial x} - \frac{\partial H_x}{\partial y} = -i\omega\epsilon E_z \quad (3.12)$$

Since the grating and the incident light are uniform along the z -axis, all of the partial derivatives with respect to z are 0. For TE polarization, since E_x and H_z are 0, equations (3.7, 3.8, and 3.12) are decoupled into

$$\frac{\partial E_z}{\partial y} = i\omega\mu H_x \quad (3.13)$$

$$-\frac{\partial E_z}{\partial x} = i\omega\mu H_y \quad (3.14)$$

and

$$\frac{\partial H_y}{\partial x} - \frac{\partial H_x}{\partial y} = -i\omega\epsilon E_z \quad (3.15)$$

We can use (3.13) and (3.14) to eliminate H_x and H_y in (3.15):

$$\frac{i}{\omega\mu} \frac{\partial^2 E_z}{\partial x^2} + \frac{i}{\omega\mu} \frac{\partial^2 E_z}{\partial y^2} = -i\omega\epsilon E_z \quad (3.16)$$

Note that ϵ is a function of position $\epsilon(x, y)$, since it changes whether inside the grating or above the grating. Since

$$k^2(x, y) = v^2(x, y) \omega^2 / c^2 = \omega^2 \mu \epsilon(x, y) \quad (3.17)$$

we get a single second-order wave equation in E_z

$$\nabla^2 E_z + k^2 E_z = 0 \quad (3.18)$$

where $E_z = E_z(x, y)$ and $k^2 = k^2(x, y)$ are both functions of position.

For the case of TM polarization, the Maxwell equations (3.10, 3.11, and 3.9) reduce to

$$\frac{\partial H_z}{\partial y} = -i\omega\epsilon E_x \quad (3.19)$$

$$-\frac{\partial H_z}{\partial x} = -i\omega\epsilon E_y \quad (3.20)$$

$$\frac{\partial E_y}{\partial x} - \frac{\partial E_x}{\partial y} = i\omega\mu H_z \quad (3.21)$$

and an identical procedure produces the wave equation in H_z :

$$\nabla \left[\frac{1}{k^2} \nabla H_z \right] + H_z = 0 \quad (3.22)$$

$$\nabla^2 H_z + k^2 H_z = 0 \quad (3.23)$$

Due to the (near) symmetry of the Maxwell equations, the form of the wave equation is the same for the H_z field in TM polarization as it is for the E_z field in TE polarization. To solve the grating problem, we will need to find the solution to this wave equation in the presence of the grating boundary conditions.⁹

3.1.4 Periodicity of gratings and fields (aka, pseudo-periodic functions and the Fourier basis)

The periodic nature of the grating grooves immediately hints that we could represent them conveniently using a Fourier series. But can a Fourier expansion also be used to represent the fields E_z and H_z ?

Here we define $u = E_z$ when working in TE polarization, and $u = H_z$ when working in TM polarization; it represents the “generic field”. The grating can be imagined as an operator \mathbb{G} that transforms the incident field u_i into a diffracted field u :

$$u(x, y) = \mathbb{G} u_i(x, y) \quad (3.24)$$

Because the grating is periodic and extends forever, the operator \mathbb{G} is invariant (does not change) under translation by a grating period: $x \rightarrow x + d$.

$$u(x + d, y) = \mathbb{G} u_i(x + d, y) \quad (3.25)$$

Since the incident light arrives at an angle θ_2 , this translation will add an extra path distance $d \sin \theta_2$ to the incident wave u_i , for a phase change $e^{ik_2 d \sin \theta_2}$:

$$u_i(x + d, y) = e^{ik_2 d \sin \theta_2} u_i(x, y) = C u_i(x, y) \quad (3.26)$$

where the constant C has been matched to $e^{ik_2 d \sin \theta_2}$.

⁹Although the wave equation is the same, the boundary conditions for electric and magnetic fields are different at the grating boundary where ϵ and ν change suddenly – for example, the normal component of the electric field is discontinuous, while the normal component of the magnetic field is continuous. This leads to a difference in the TE and TM efficiency.

Because the set of coupled Maxwell partial differential equations (3.7 - 3.12) is linear, any solution multiplied by a constant C is still a solution:

$$u(x, y) = \mathbb{G}(u_i(x, y)) \quad (3.27)$$

$$C u(x, y) = \mathbb{G}(C u_i(x, y)) \quad (3.28)$$

$$C u(x, y) = \mathbb{G} u_i(x + d, y) \quad (3.29)$$

but since $\mathbb{G} u_i(x + d, y) = u(x + d, y)$ also,

$$C u(x, y) = u(x + d, y) \quad (3.30)$$

In other words, the total field translated by one period d is equal to its untranslated self, multiplied by a complex constant:

$$u(x + d, y) = C u(x, y) = e^{ik_2 d \sin \theta_2} u(x, y) = e^{i\alpha_0 d} u(x, y) \quad (3.31)$$

where we have defined

$$\boxed{\alpha_0 \equiv k_2 \sin \theta_2} \quad (3.32)$$

This is known as a *pseudo-periodic* relationship:

$$u(x + d, y) = e^{i\alpha_0 d} u(x, y) \quad (3.33)$$

since a true (strictly) periodic relationship would have the form:

$$v(x + d, y) = v(x, y) \quad (3.34)$$

However, we can easily create such a function by defining $v \equiv e^{-i\alpha_0 x} u$. As a legitimately periodic function, v can be represented as a Fourier series expansion on the grating period d :

$$v(x, y) = e^{-i\alpha_0 x} u(x, y) \quad (3.35)$$

$$v(x, y) = \sum_{n=-\infty}^{\infty} u_n(y) e^{i2\pi n x/d} \quad (3.36)$$

$$u(x, y) = e^{i\alpha_0 x} \sum_{n=-\infty}^{\infty} u_n(y) e^{i2\pi n x/d} \quad (3.37)$$

If we define

$$\boxed{\alpha_n \equiv \alpha_0 + 2\pi n/d} \quad (3.38)$$

we can express the total field as something that looks *very close* to a Fourier series expansion:

$$u(x, y) = \sum_{n=-\infty}^{\infty} u_n(y) e^{i\alpha_n x} \quad (3.39)$$

This is the Fourier basis for the total field $u = E_z$ or H_z , with an infinite number of Fourier coefficients u_n . (Eventually, we will need to truncate this series to work with it numerically.)

3.1.5 Deriving the Grating Equation

Equipped with a Fourier expansion for the total field and a wave equation, we can attempt to solve for the field. Figure 3.1 shows the coordinate system sliced into three regions:

- Region 2: Above the grooves where $y > a$, the impedance $k(x, y)$ is constant and proportional to the refractive index of the air/vacuum: $k_2(x, y) = v_2\omega/c$.
- Region 1: Below the grooves where $y < 0$, the impedance $k(x, y)$ is also constant and proportional to the grating's refractive index: $k_1(x, y) = v_1\omega/c$.
- Inside the grooves, the impedance is changing as a function of position: whether inside or outside of a groove. We ignore this difficult region for now and try to work with the uniform regions as much as possible.

Where $k(x, y)$ is constant, the wave equations for both TE (3.18) and TM polarization (3.22) reduce to:

$$\nabla^2 u + k^2 u = 0 \quad (3.40)$$

where $k = k_1$ above the grating, and $k = k_2$ below it. If we insert the Fourier expansion for the field $u(x, y) = \sum u_n(y)e^{i\alpha_n x}$ into the wave equation:

$$\nabla^2 \left(\sum_{n=-\infty}^{\infty} u_n(y)e^{i2\pi nx/d}e^{i\alpha_0 x} \right) + k^2 \sum_{n=-\infty}^{\infty} u_n(y)e^{i2\pi nx/d}e^{i\alpha_0 x} = 0 \quad (3.41)$$

$$e^{i\alpha_0 x} \sum_{n=-\infty}^{\infty} \left(\frac{\partial^2}{\partial y^2} + (k^2 - (\alpha_0 + 2\pi n/d)^2) \right) u_n(y)e^{i2\pi nx/d} = 0 \quad (3.42)$$

For this Fourier sum to be equal to zero, all of the coefficients must be zero:

$$\left(\frac{\partial^2}{\partial y^2} + (k^2 - (\alpha_0 + 2\pi n/d)^2) \right) u_n(y) = 0 \quad (3.43)$$

$$\left(\frac{\partial^2}{\partial y^2} + (k^2 - \alpha_n^2) \right) u_n(y) = 0 \quad (3.44)$$

This is a standard differential equation with the solution

$$u_n(y) = A_n e^{-i\beta_n y} + B_n e^{i\beta_n y} \quad (3.45)$$

where

$$\beta_n = \sqrt{k^2 - \alpha_n^2} \quad (3.46)$$

and A_n and B_n are unknown constants to be determined by the boundary conditions.

Special attention must be paid to the square root for β_n , depending on whether we are above or below the grating.

Above the grating

Above the grating, we are likely inside air or vacuum ($k = k_2$), so the refractive index and k would be real. Since $\alpha_n = \alpha_0 + 2\pi n/d$ will increase with n , there will be a finite number of n near $n = 0$ where $(k^2 - \alpha_n^2)$ will be a positive number. However, there will be an infinite number of n (approaching $n \rightarrow \infty$ and $n \rightarrow -\infty$) where $(k^2 - \alpha_n^2) < 0$. This creates two possibilities for β_n (which we label $\beta_n^{(2)}$ because we are in Region 2):

$$\beta_n^{(2)} = \sqrt{k^2 - \alpha_n^2} \quad (k^2 - \alpha_n^2) > 0 \quad (\text{finite occurrences, } \beta_n^{(2)} \text{ real}) \quad (3.47)$$

$$\beta_n^{(2)} = i\sqrt{\alpha_n^2 - k^2} \quad (k^2 - \alpha_n^2) < 0 \quad (\text{infinite occurrences, } \beta_n^{(2)} \text{ complex}) \quad (3.48)$$

Using this solution for the Fourier coefficients u_n , the total field is:

$$u(x, y) = \sum_{n=-\infty}^{\infty} A_n^{(2)} e^{i\alpha_n x - i\beta_n^{(2)} y} + \sum_{n=-\infty}^{\infty} B_n^{(2)} e^{i\alpha_n x + i\beta_n^{(2)} y} \quad (3.49)$$

This result is remarkable. The total field created above the grating is a finite sum of propagating plane waves (for all n where $\beta_n^{(2)}$ is real) and an infinite sum of decaying (when $\beta_n^{(2)}$ is complex) plane waves.

To expand on this conclusion: The first sum (with $A_n^{(2)}$ coefficients) are waves travelling in the $-y$ direction, down toward the grating. For the finite set of n for which $\beta_n^{(2)}$ is real, these are non-decaying, normal waves. There is also an infinite number of exponentially growing waves that explode as $y \rightarrow +\infty$, for the remaining n that cause $\beta_n^{(2)}$ to be complex.

Similarly, the second sum (with $B_n^{(2)}$ coefficients) represents waves travelling away from the grating, in the $+y$ direction. There is a finite set of propagating waves, and an infinite set of exponentially decaying waves that tend to zero as $y \rightarrow +\infty$.

The total field will have a unique solution only when the incident field u_i is totally specified. From the grating setup in Figure 3.1, we know that we only have a single down-going wave, corresponding to the incident plane wave; all of the $A_n^{(2)}$ for the other propagating waves must be 0. (We label this incident wave as $n = 0$.) We also need to reject the non-physical waves that explode as $y \rightarrow +\infty$, therefore the expansion of the field *above the grating* simplifies to:

$$u(x, y) = A_0^{(2)} e^{i\alpha_0 x - i\beta_0^{(2)} y} + \sum_{n=-\infty}^{\infty} B_n^{(2)} e^{i\alpha_n x + i\beta_n^{(2)} y} \quad (3.50)$$

The diffraction grating's reflected orders appear out of this expansion as the finite set of n , $\beta_n^{(2)}$, and $B_n^{(2)}$ values that create propagating plane waves travelling away from the grating. At this point, n can now be properly identified with the *diffraction order*. This is known as the *Rayleigh Expansion* for the diffraction field. Figure 3.2 shows this visually and mathematically.

Below the grating

The field below the grating ($y < 0$) can be expanded using the same technique. One complication is that for grating materials that absorb energy, the refractive index (and hence $k = k_1$) will be complex.¹⁰ In this

¹⁰In fact, this is the case for all materials at soft x-ray wavelengths.

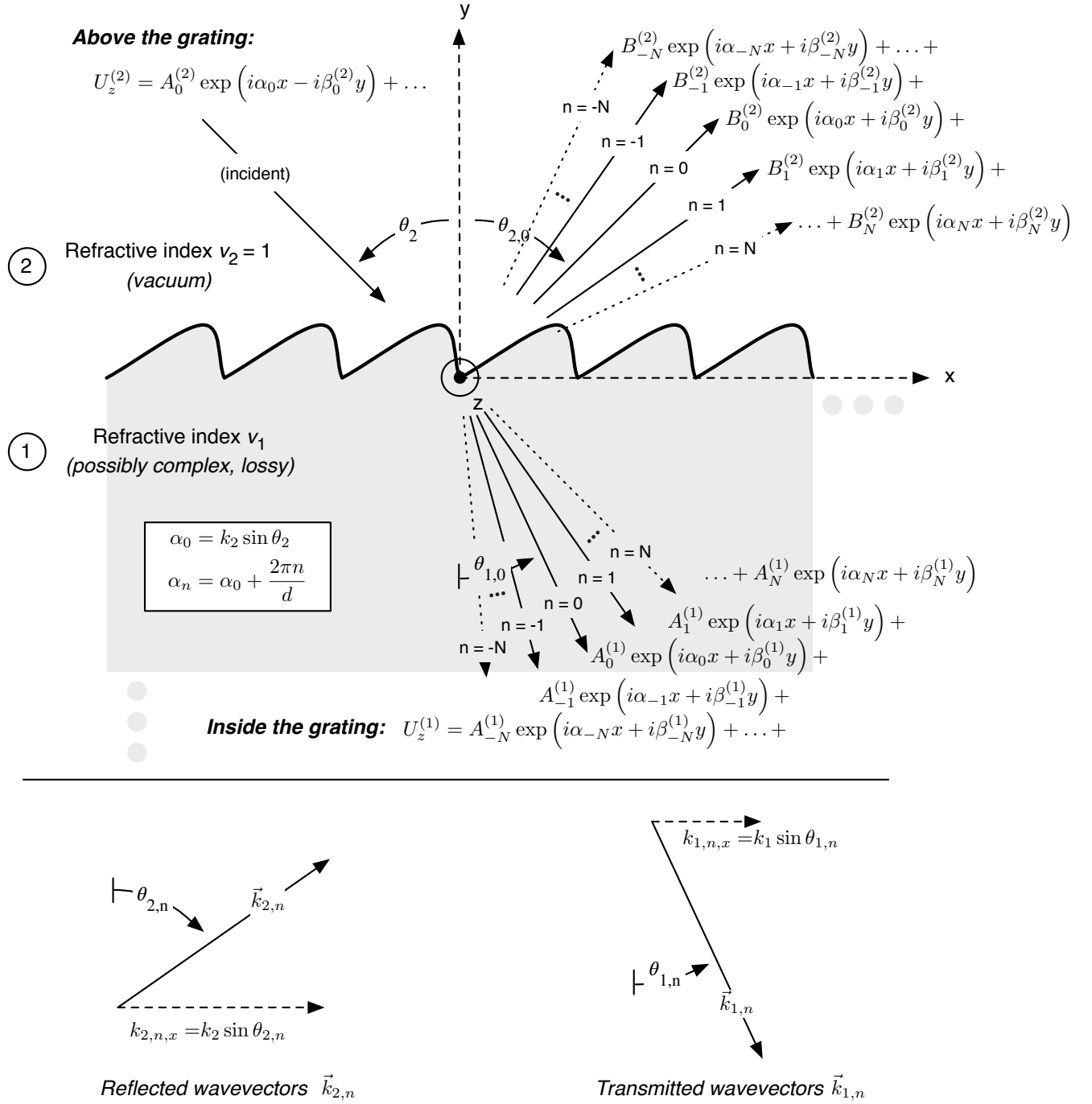


Figure 3.2: The Rayleigh expansion describes the electric field (TE polarization) or magnetic field (TM polarization) in homogenous media, above and below the grating. The terms in the expansion include a finite number of propagating plane waves – the diffraction orders – and an infinite number of decaying, or “evanescent” plane waves. From the geometry of the diffracted and transmitted wave vectors, we can derive the grating equation, but we need to solve the A_n and B_n coefficients to determine the efficiency of each order.

situation there are two possibilities for the square root $\beta_n^{(1)} = \sqrt{k_1^2 - \alpha_n^2}$. The correct choice can be made by requiring that the diffracted waves remain bounded when $y \rightarrow -\infty$. The result provides an expansion for the transmitted field, corresponding to the transmitted orders. These are also shown visually in Figure 3.2:

$$u(x, y) = \sum_{n=-\infty}^{\infty} A_n^{(1)} e^{i\alpha_n x - i\beta_n^{(1)} y} \quad (3.51)$$

The grating equations

These expansions for the reflected and transmitted fields show that as soon as the direction of the incident wavevector is fixed, the outgoing directions of light are determined. For the *reflected* orders, Equation 3.50 gives the x - and y -components of the wavevectors:

$$B_n^{(2)} e^{i(k_x x + k_y y)} = B_n^{(2)} e^{i(\alpha_n x + \beta_n^{(2)} y)} \quad (3.52)$$

$$k_x = \alpha_n \quad (3.53)$$

$$= \alpha_0 + \frac{2\pi n}{d} \quad (3.54)$$

$$= k_2 \sin \theta_2 + \frac{2\pi n}{d} \quad (3.55)$$

From the geometry analyzed in Figure 3.2, the x -component of the outgoing wavevector at angle $\theta_{2,n}$ is $k_2 \sin \theta_{2,n}$. Therefore

$$k_x = k_2 \sin \theta_2 + \frac{2\pi n}{d} = k_2 \sin \theta_{2,n} \quad (3.56)$$

and, after replacing the magnitude of the wavevector above the grating $k_2 = v_2 \omega / c = v_2 2\pi f / c = 2\pi / \lambda$, the famous grating equation (for reflected orders) is finally:

$$\frac{n\lambda}{d} = \sin \theta_{2,n} - \sin \theta_2 \quad (3.57)$$

(where we have assumed that $v_2 = 1$ because we are in free space, and λ is also the free-space wavelength.)

This is often called the *Fraunhofer Grating Equation*.

When $n = 0$, the grating equation reverts to the law of reflection ($\theta_{2,0} = \theta_2$, i.e.: the angle of reflection is equal to the angle of incidence.) This wave corresponds to a classically-reflected wave from a normal surface. The reflected orders that fall *between* the incident wave and the $n = 0$ reflection are referred to as *inside orders*; using our sign convention for diffraction angles, they correspond to $n < 0$. The *outside orders* ($n > 0$, see Figure 3.2) are diffracted at angles beyond the $n = 0$ reflection.

We can also use the same technique to determine the angles of the transmitted orders. Equation 3.51 gives the x - and y -components of the transmitted wavevectors:

$$A_n^{(1)} e^{i(k_x x + k_y y)} = A_n^{(1)} e^{i(\alpha_n x + \beta_n^{(1)} y)} \quad (3.58)$$

$$k_x = \alpha_n = \alpha_0 + \frac{2\pi n}{d} = k_2 \sin \theta_2 + \frac{2\pi n}{d} \quad (3.59)$$

From the geometry analyzed in Figure 3.2, the x -component of the outgoing wavevector at angle $\theta_{1,n}$ is $k_1 \sin \theta_{1,n}$. Therefore

$$k_x = k_2 \sin \theta_2 + \frac{2\pi n}{d} = k_1 \sin \theta_{1,n} \quad (3.60)$$

and, after again replacing k_1 , the magnitude of the wavevector below the grating $k_1 = v_1 \omega / c = v_1 2\pi f / c = v_1 2\pi / \lambda$, the transmission grating equation is:

$$\frac{n\lambda}{d} = v_1 \sin \theta_{1,n} - v_2 \sin \theta_2 \quad (3.61)$$

This time, instead of checking for the law of reflection, we can check that when $n = 0$, the transmission equation reverts to Snell's law of refraction ($v_1 \sin \theta_{1,0} = v_2 \sin \theta_2$).

Note: Simplifying β_n

Equations 3.56 and 3.60 provide a useful simplification for β_n . Since

$$k_2 \sin \theta_2 + \frac{2\pi n}{d} = k_2 \sin \theta_{2,n} = k_1 \sin \theta_{1,n} \quad (3.62)$$

we can go back to the expression for β_n , and easily show that

$$\beta_n^{(2)} = \sqrt{k_2^2 - \alpha_n^2} = \sqrt{k_2^2 - (\alpha_0 + 2\pi n/d)^2} \quad (3.63)$$

$$= \sqrt{k_2^2 - (k_2 \sin \theta_2 + 2\pi n/d)^2} \quad (3.64)$$

$$= \sqrt{k_2^2 - (k_2 \sin \theta_{2,n})^2} \quad (3.65)$$

$$= \sqrt{k_2^2 (1 - \sin^2 \theta_{2,n})} \quad (3.66)$$

$$= \sqrt{k_2^2 \cos^2 \theta_{2,n}} \quad (3.67)$$

$$= k_2 \cos \theta_{2,n} \quad (3.68)$$

Similarly, for the transmitted order,

$$\beta_n^{(1)} = k_1 \cos \theta_{1,n} \quad (3.69)$$

Finishing the grating problem

Based only on Maxwell's equations and an assumption of periodicity, we have shown that a grating reflects and transmits light into a set of discrete angles. Incredibly, this result is fully general – it does not depend at all on the shape or nature of the grating profile; all that's required is that it be periodic. Unfortunately, this impressive result still says nothing at all about the *grating efficiency*, or the *amount* of light diffracted into each order. We still do not know anything about the *amplitudes* B_n , A_n of the diffracted plane waves, and to determine these coefficients we will need to get down and dirty inside the grooves of the grating.

Within the grooves, the wave equations (3.18, 3.22) are much more difficult to solve due to the position-dependence of $k(x, y)$. The refractive index (and therefore the impedance k) will change whether inside or

outside of a groove, and if the grating shape is complicated, $k(x, y)$ will be a complicated function indeed. Several decades of intense research have produced a handful of methods for solving the full boundary-value problem, all of which are hampered by unique challenges of computational feasibility, numerical stability, and accuracy of approximations. Table (TODO) lists the most common methods, with references and areas of applicability.

Some methods are only applicable in specific cases. For example, for certain particular groove profiles, there exist coordinate transformations (“conformal mappings”) which simplify the boundary conditions so they can be solved analytically. In the following sections, we present an overview of two *general* methods which can handle arbitrary groove profiles. Before getting there, however, we take a closer look at defining grating efficiency.

3.2 Defining Grating Efficiency

In spectroscopy applications, the experimenter typically illuminates a grating with light and uses a single outgoing order ($n \neq 0$) to resolve the light by wavelength. If they are concerned about optimizing the amount of light delivered to their experiment, the “efficiency” question that matters to them is, “*How much light do I get out of the grating (in the useful order), compared to how much light went in?*” Fundamentally, this depends on how much energy is absorbed in the grating itself, and how energy is distributed between orders.

We can define the grating efficiency for a single order quite rigorously in the same way. For electromagnetic plane waves, the *Poynting Vector* represents the energy flux (or energy per unit area, W/m^2) carried by the wave:

$$\vec{S} = \vec{E} \times \vec{H} \quad (3.70)$$

This gives the instantaneous energy flux, which will oscillate in time with the wave. The *time-averaged Poynting vector* gives the average flux delivered over a full period of the wave. For harmonic waves, this turns out to be

$$\bar{S} = \frac{1}{2} \text{Re} \left(\vec{E} \times \vec{H}^* \right) \quad (3.71)$$

where \vec{H}^* denotes the complex conjugate of \vec{H} .

We define the grating efficiency formally as *the ratio of the total time-averaged Poynting flux – through a surface parallel to the mean grating plane – of the outgoing order ($\bar{S}_n^{(2)}$) relative to the incident wave ($\bar{S}^{(2)}$)*. Figure 3.3 highlights the surface Q_2 used for reflected efficiencies ($e_n^{(r)}$), which spans one grating period d in the x -direction, and has unit length in the z -direction. For defining transmitted efficiencies $e_n^{(t)}$, we use a

similar surface Q_1 at $y \leq 0$.

$$e_n^{(r)} \equiv \frac{\iint_{Q_2} \bar{S}_n^{(2)} \hat{y} \, dz dx}{\iint_{Q_2} \bar{S}^{(2)} \hat{y} \, dz dx} \quad (3.72)$$

$$e_n^{(t)} \equiv \frac{\iint_{Q_1} \bar{S}_n^{(1)} \hat{y} \, dz dx}{\iint_{Q_1} \bar{S}^{(1)} \hat{y} \, dz dx} \quad (3.73)$$

Time-averaged Poynting vectors:

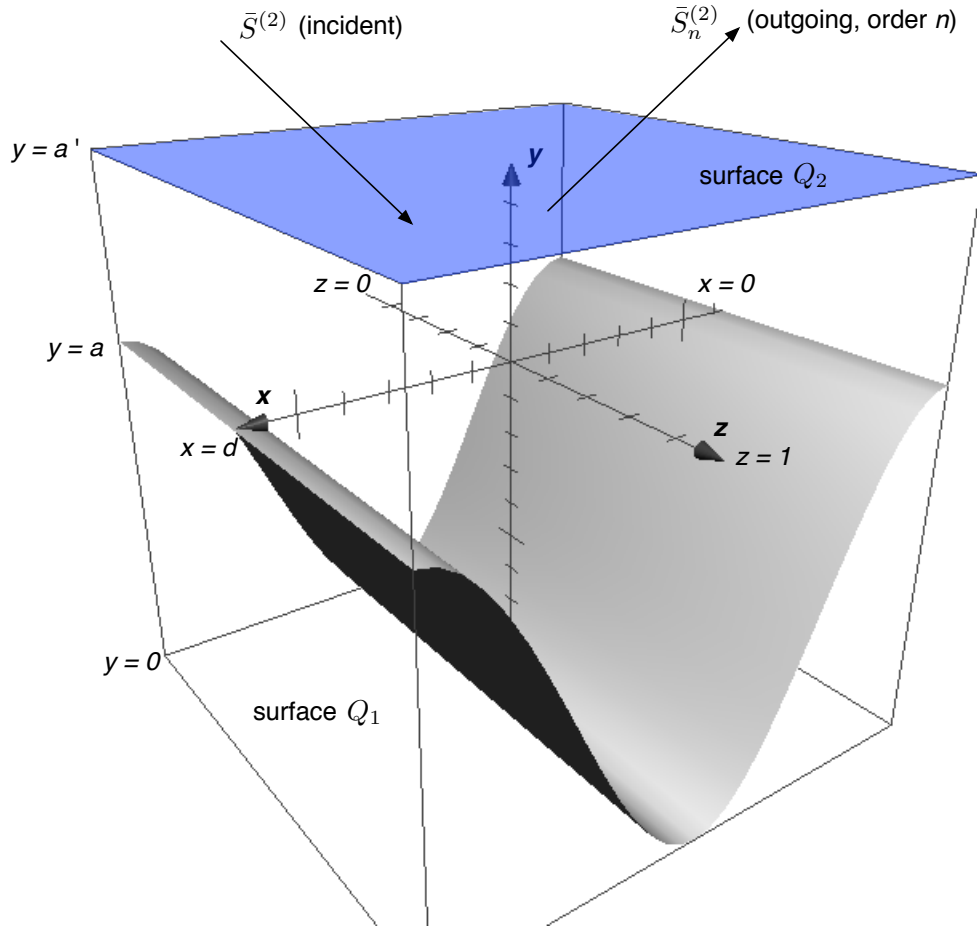


Figure 3.3: The total electromagnetic flux through this highlighted area (Q_2) is used to define the grating efficiency of a diffraction order n , as the ratio of the flux of the diffracted wave $\bar{S}_n^{(2)}$ compared to the incident wave $\bar{S}^{(2)}$.

It turns out that this definition for efficiency can be nicely expressed in terms of the coefficients in the Rayleigh expansion for the reflected and transmitted fields (3.50, 3.51), so that if we can solve for these coefficients, we'll have determined the grating efficiency:

Reflected Efficiencies

We know that the incident and diffracted orders are plane waves, so the magnetic field \vec{H} is related to the electric field \vec{E} as

$$|\vec{H}| = \frac{|\vec{E}|}{Z_2} \quad (3.74)$$

where $Z_2 = v_2 Z_0$ is the impedance of the space above the grating (usually free space, so $v_2 = 1$ and $Z_2 = Z_0 = 377\Omega$, the impedance of free space). Based on the Rayleigh expansion for the outgoing field (equation 3.50), the magnitude of the time-averaged Poynting vector for the *reflected order* is therefore

$$|\bar{S}| = B_n^{(2)} B_n^{(2)*} \eta_2 \quad (3.75)$$

where we have defined $\eta_2 \equiv 1/(2Z_2)$ in the case of TE polarization, and $\eta_2 \equiv 2Z_2$ for TM polarization. The direction of the vector is along the propagation direction, ie: at an angle $\theta_{2,n}$ to the y -axis, therefore the integrated flux through the surface is:

$$\iint_{Q_2} \bar{S}_n^{(2)} \hat{y} dz dx = \int_0^d \int_0^1 \bar{S}_n^{(2)} \hat{y} dz dx \quad (3.76)$$

$$= B_n^{(2)} B_n^{(2)*} \eta_2 d \cos \theta_{2,n} \quad (3.77)$$

For the incident wave, the integrated flux is similarly

$$\iint_{Q_2} \bar{S}^{(2)} \hat{y} dz dx = A_0^{(2)} A_0^{(2)*} \eta_2 d \cos \theta_2 \quad (3.78)$$

and so the reflected efficiency in order n is:

$$e_n^{(r)} = \frac{B_n^{(2)} B_n^{(2)*} \cos \theta_{2,n}}{A_0^{(2)} A_0^{(2)*} \cos \theta_2} \quad (3.79)$$

We can simplify this somewhat by choosing a unit amplitude for the incident field, i.e.: $A_0^{(2)} = 1\text{V/m}$ for the TE electric field, or 1A/m for the TM magnetic field. Also, since $\beta_n^{(2)} = k_2 \cos \theta_{2,n}$, we can simplify this to

$$e_n^{(r)} = B_n^{(2)} B_n^{(2)*} \frac{\beta_n^{(2)}}{\beta_0^{(2)}} \quad (3.80)$$

Transmitted Efficiencies

Gratings used in the soft x-ray regime are always used in reflection, due to the high absorption of materials at these wavelengths. However, since we're working on a general theory with application to all gratings, we can go through the same process for simplifying the transmitted efficiencies.

Again, we define $\eta_1 \equiv 1/(2Z_1)$ in TE polarization, and $\eta_1 \equiv 2Z_1$ in TM polarization, where $Z_1 = v_1 Z_0$ is the impedance of the grating substrate material. The same integrations over the surface Q_1 give the ratio

between the total transmitted and incident fluxes:

$$e_n^{(t)} = \frac{A_n^{(1)} A_n^{(1)*} \cos \theta_{1,n} \eta_1}{A_0^{(2)} A_0^{(2)*} \cos \theta_2 \eta_2} \quad (3.81)$$

In this case, the difference in impedance above and below the grooves causes η_1 and η_2 to remain in the formula, so the final simplification depends on polarization:

$$e_n^{(t)} = A_n^{(1)} A_n^{(1)*} \frac{\beta_n^{(1)}}{\beta_0^{(2)}} \quad (\text{TE Polarization}) \quad (3.82)$$

$$= A_n^{(1)} A_n^{(1)*} \frac{\beta_n^{(1)}}{\beta_0^{(2)}} \left(\frac{v_2}{v_1} \right)^2 \quad (\text{TM Polarization}) \quad (3.83)$$

3.3 Solving for efficiency

- Solving: Requires periodic representation of refractive index: only true at fixed (y). Needs computational methods

– key set of differential equations to solve... $d^2 E_n / dy^2 + k^2 E_n = 0$

3.3.1 Numerical Challenges

Integration of growing exponentials

- Integrating growing exponentials: floating point rounding error leads to runaway [reference: Neviere: S-matrix; Somebody: R-matrix]

Truncation of Fourier expansions

- Must truncate Fourier expansion. Problem in TM case: makes field discontinuous, where should be continuous. [reference: Li, FFF]

3.3.2 Applying boundary conditions within the groove region

- Highlighted methods for dealing with boundary conditions in groove region:

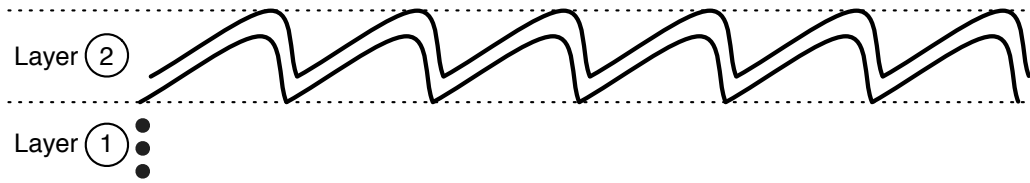
- RCWA: split into thin layers and make rectangular
- Differential method
- Table of methods, areas of applicability, and references

3.3.3 Handling stacks of gratings

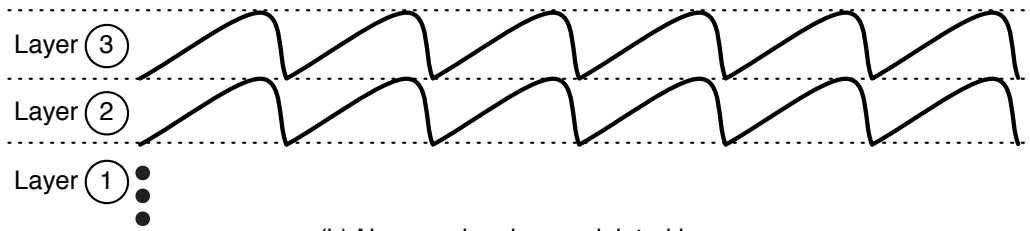
3.4 X-rays and materials: how do they interact?

(Especially: lossy metals) - Characterized: atomic scattering factor - f' *complex refractive index*

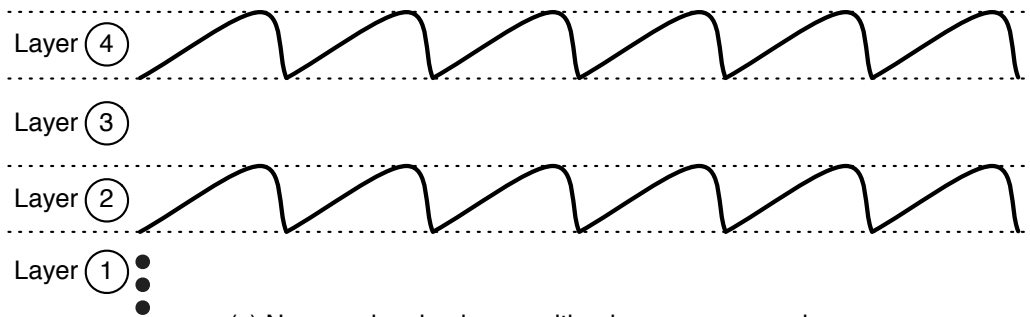
FIGURE 2e: plot of real and imaginary components... Metals at 100-1000eV.



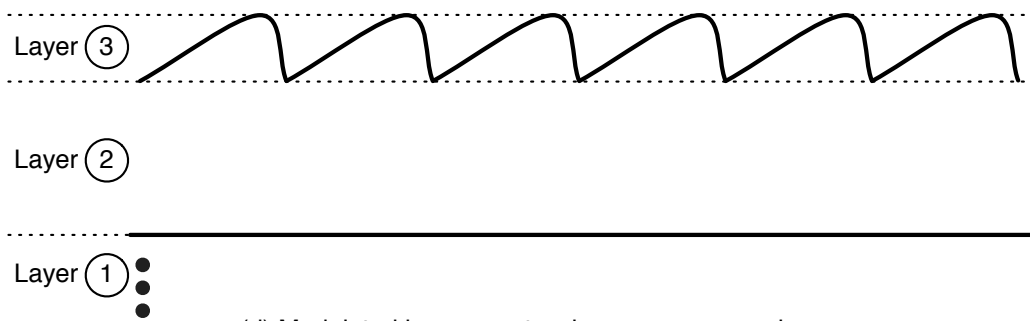
(a) Overlapping modulated layers



(b) Non-overlapping modulated layers



(c) Non-overlapping layers with a homogenous region



(d) Modulated layer over two homogeneous regions
(ex: grooves ruled into a metal-coated dielectric blank)

Figure 3.4: Arbitrarily-complicated structures can be handled by dividing the grating into layers, where each layer is either homogenous (constant refractive index), or modulated (with a refractive index that changes periodically as a function of x at any given height y).

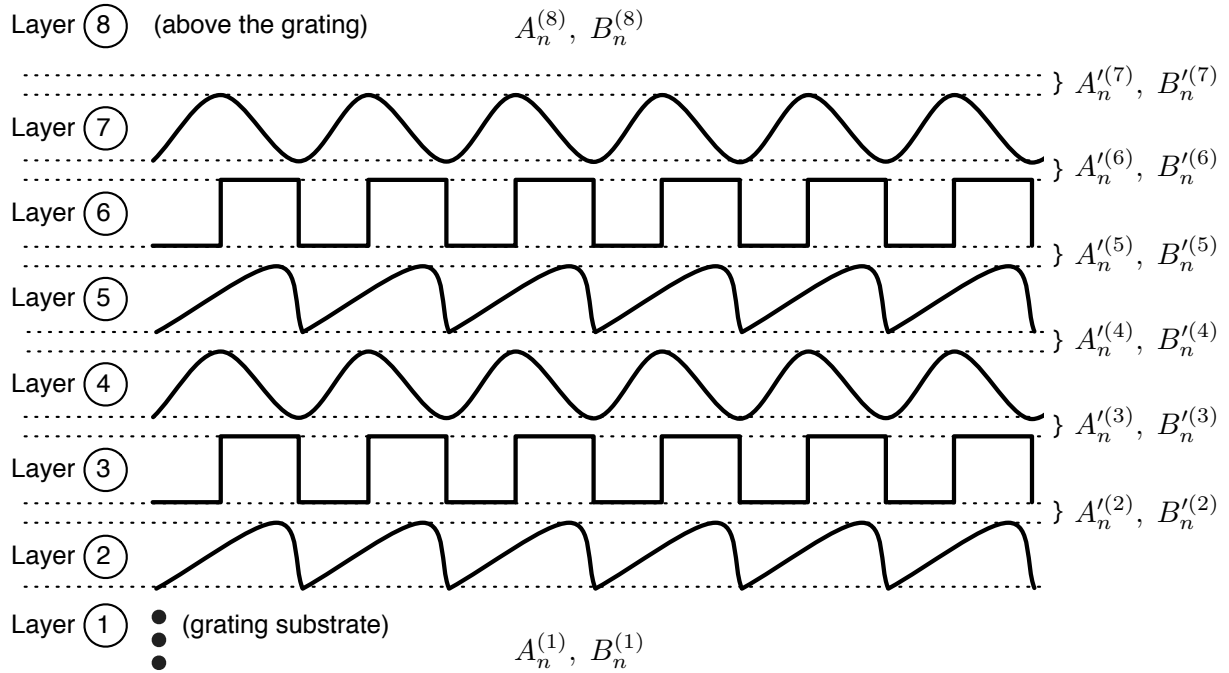


Figure 3.5: Modulated layers in a complicated stack of gratings. In between every layer, we can insert an imaginary, infinitely-thin homogenous layer where the Rayleigh expansion applies. The A'_n and B'_n expansion coefficients connect the boundary conditions between layers. Within each layer, the Rayleigh expansion does not apply – inside the grooves, the field cannot be represented as a simple sum of plane waves – and numerical methods are required to approximate it.

- RI Derived from Henke Data
- Reference CXRO calculator
- Note: total external reflection (overcome notoriously absorbing materials via grazing incidence)

Next chapter: look at the how this is applied, and what we can learn about grating efficiency using the theory

REMAINING QUESTIONS: numerical integration of WHAT. (A: 2nd order in TE; 1st-order in TM. Eqn II.2')

How to get coefficients for $k_2(x,y)$?

CHAPTER 4

IMPLEMENTATION OF THEORY: WHAT PEOPLE AND I DID TO IMPLEMENT THE THEORY USING COMPUTERS

Introduction: yadda yadda yadda (TODO)

4.1 Methods

4.1.1 Rigorous Coupled Wave method: GSolver

TODO

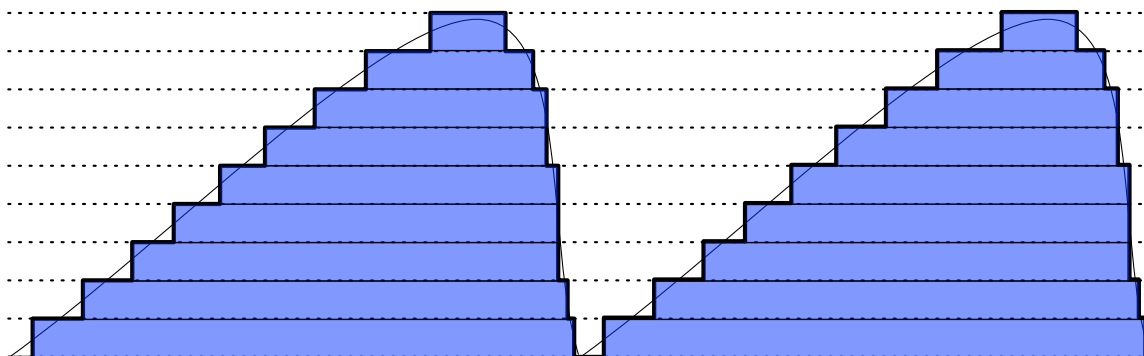


Figure 4.1: The RCW method approximates every real grating as a stack of rectangular gratings, where the boundary conditions are easy to solve and the problem can be reduced to algebraic methods.

4.1.2 Differential method: Gradif by Michel Nevieri

TODO

4.2 Improving the usability and efficiency of calculation methods

The Canadian Light Source purchased the Gradif code from Professor Nevieri and made it available for this project. However, there were two challenges involved in applying the code:

1. The code itself is an iteration on old Fortran program that provides no user interface. Instead, to calculate an efficiency data point for a grating at just one energy, approximately 30 numbers must be entered into a blank screen, with no prompts, in the correct order. These numbers define the grating geometry, the coating/layer thicknesses, the incidence conditions, the integration parameters, and also the complex refractive indices of the layers and the substrate.¹ As a result, using this program requires a time-consuming and error-prone process.
2. In the event of an error made during the data entry process, one of many grating parameters could end up outside the narrow region of convergence where the code is able to numerically integrate a solution successfully. When this happens, the program runs forever in an infinite loop, with no feedback that the calculation has failed. This region of convergence is not well established, so even when data entry errors are avoided, it is possible for a user to specify a valid grating that is – for example – too deep to be calculated. Without user feedback, it is impossible to know if the calculation is still running successfully, or if it has failed into this infinite loop.

To beat these two challenges, we built a web-based graphical interface, and carefully modified the Fortran source code to detect convergence failures.

4.2.1 Visual interface to the Gradif code

Figure 4.2 shows a screenshot of the graphical user interface (GUI) that we built to help us perform efficiency calculations quickly and efficiently. The interface serves as a wrapper to generate input for the Gradif code, manages running a set of calculations, and extracts the results.

The interface was implemented as a web-based application, so it can be used from anywhere through a browser, without having to distribute the Gradif code or install anything on a person’s individual computer. Users describe the grating parameters and application scenario through a form that prompts them for the necessary information based on the type of grating (Figure 4.2). The results automatically generate a plot, and users can also download data tables of their calculations. These tables are also archived so they can be retrieved later.

It supports the following features:

- **Grating types**

The interface supports rectangular, blazed, trapezoidal, and sinusoidal grating profiles; it prompts for the geometry parameters that are required in each case.

- **Order and polarization**

Users can configure which inside and outside orders should be calculated, as well as specify the polarization of the incident light: TE, TM, or natural light (un-polarized).

¹These last two values will change as a function of photon energy, since the refractive index varies with wavelength, so we need to look them up for each data point.

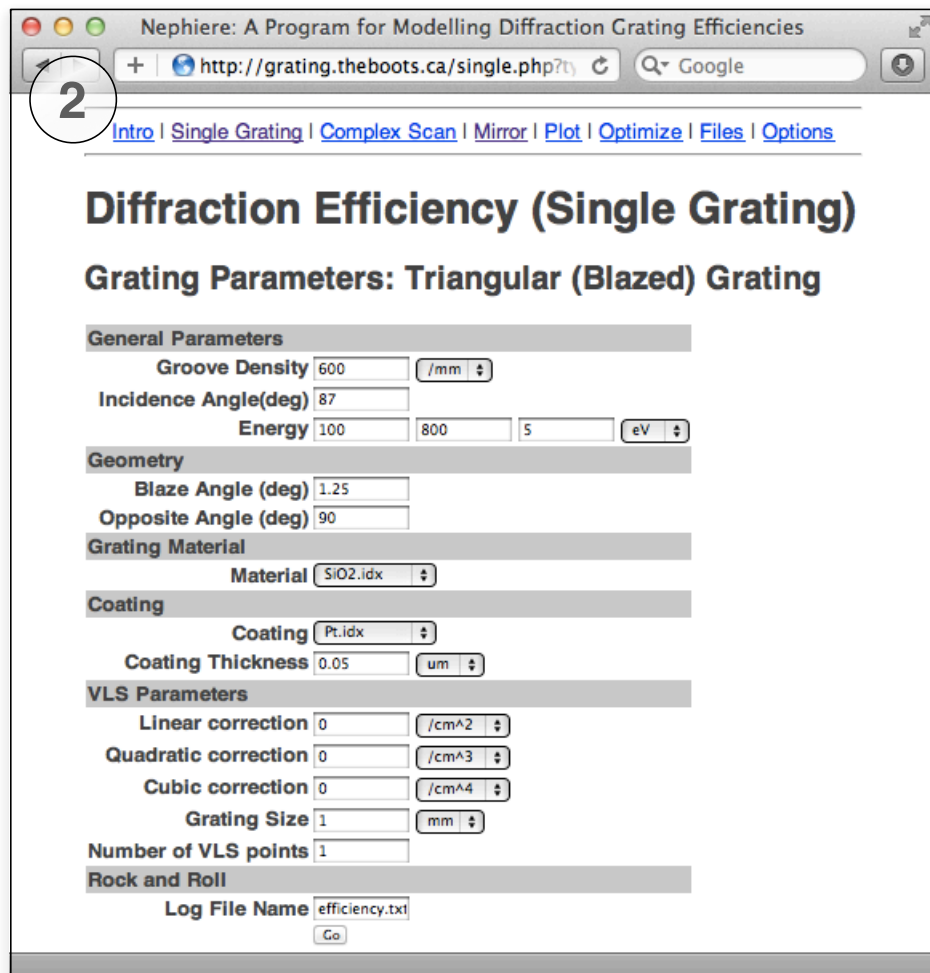
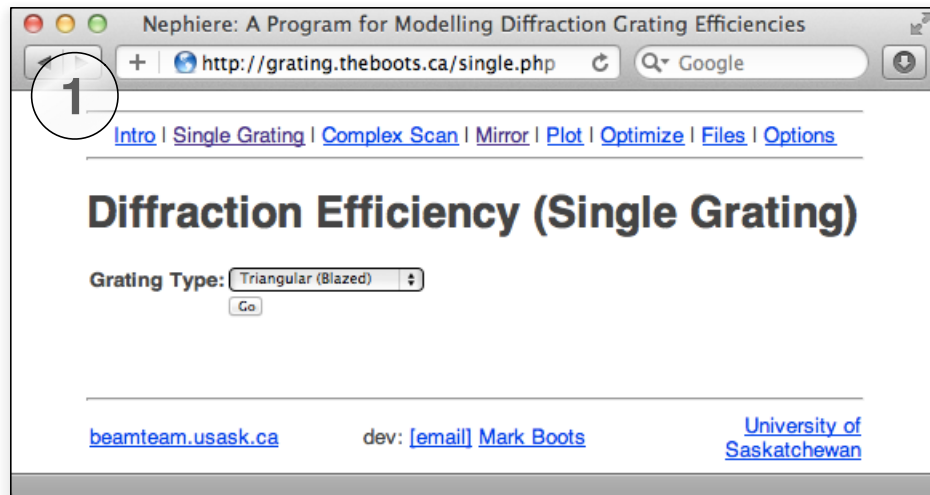


Figure 4.2: This web application provides a graphical user interface for calculating grating efficiencies. Forms prompt users for the grating parameters.

- **VLS gratings**

To model variable line space gratings, the interface accepts the VLS parameters in conventional notation (linear, quadratic, and cubic corrections) and uses these to calculate the groove density and corresponding efficiency at a user-determined number of points along the grating surface; the overall efficiency is taken as an average of these.

- **Efficiency plots as a function of wavelength**

The simplest way to use the interface generates a plot of the efficiency in the desired orders as a function of wavelength, holding all the other parameters constant (Figure 4.3). This is the most typical use-case for testing how a grating would perform in a beamline.

- **Complex scans over arbitrary grating parameters**

The interface also offers flexibility to test arbitrary relationships along incidence angle, energy, geometry, and other parameters. This feature is most efficiently used in conjunction with a spreadsheet or other data analysis program to fill in the grating parameters and interpret the data tables that are produced.

- **Database of optical materials and refractive index**

We also developed a database of common grating substrate and coating materials, so that the interface can automatically look up their complex refractive index as a function of photon energy. This information was calculated using the semi-empirical Henke data tables of the x-ray atomic form factor (TODO ref). The current library is valid from 30 eV to 10 000 eV, but is known to have limited accuracy in the immediate neighborhood of absorption edges.

- **Mirror reflectivity**

As an additional tool for beamline designers, we implemented the ability to calculate the reflectivity of a simple mirror using any of the materials in the refractive index database. Mirror reflectivities are computed as a function of incidence angle and photon energy using the complex Fresnel equations (TODO ref Modern Optics), and are subject to the same options for polarization.

- **Control of numerical precision**

An ‘Options’ page (Figure 4.4) allows users to configure the numerical precision used in the calculations. The two critical factors are the number of integration steps used in the numerical integration of the particular solutions for the $A_n^{(m)}$ and $B_n^{(m)}$ coefficients at each layer, and the number of Fourier coefficients N used before the sum is truncated. The defaults we chose ($N = 31$; 401 integration steps) have been found to produce accurate results reasonably quickly across the entire soft x-ray range, as long as the coating thickness is less than 0.5 μm . However, prudent designers should still do convergence tests for any high-stakes results, by repeating the calculations and comparing against efficiencies computed using larger values. This technique can also be used to find the minimum number of Fourier coefficients that are required before the results start to disagree. (This can be helpful to optimize the computation speed before running a large number of calculations on similar gratings at similar wavelengths.)

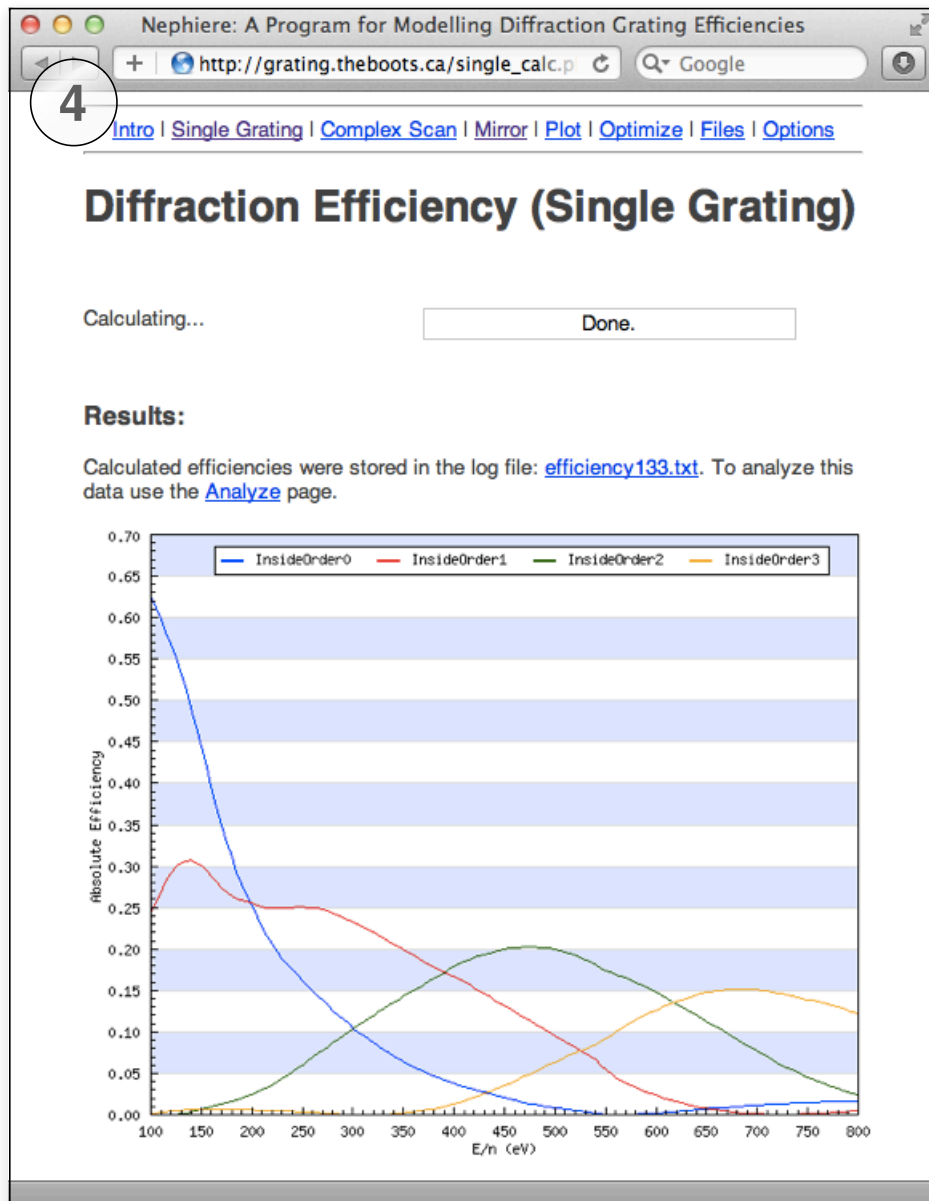
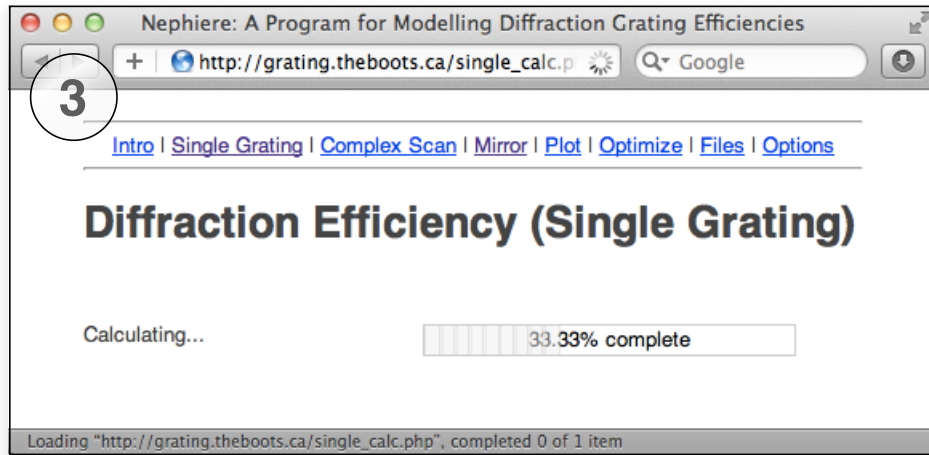


Figure 4.3: This web application provides a graphical user interface for calculating grating efficiencies. The results are plotted, and users can download a text-based table for further analysis.

4.2.2 Detecting convergence failures

The Fortran code that makes up the Gradif program was written using a 1970's-era programming approach, including prodigious use of global variables and GOTO statements. (These two features are now heavily discouraged in modern programming methodologies.) As a result, the code is hard to trace, but we were able to insert a counter to detect when a numerical integration fails to converge after multiple attempts. This allows the calculation to exit with an error message, rather than run indefinitely.

4.2.3 Open source, open access, and future work

Since we released the user interface under an ‘open-source’ license, it can be upgraded or enhanced by anyone with an interest in the beamline design community. Julian Miller, a summer student in the metrology department at the CLS, recently created an updated version of the interface to support multi-threaded calculations and add more options for incidence configurations. To the original ‘constant incidence angle’ mode, he added a ‘constant included angle’ mode, used in many monochromators, which tilts the grating as a function of photon energy to maintain a constant angle between the incident and outgoing beam in the desired order. Since every grating efficiency calculation (at a single energy) is independent, they can be run in parallel; this takes advantage of modern multi-core processors, and dramatically speeds up the creation of a user’s plot or data set. In the future, this could be extended even further to spread calculations over a cluster of computers, or on distributed hardware in a ‘cloud computing’ network.

Because the user interface runs as a web application, it can be (and has been) accessed by beamline designers from all over the world. As one example, it was used by Professor Coryn Hague to improve the design of a new beamline for the SOLEIL synchrotron (TODO find ref). The calculations can be requested and retrieved by anyone from anywhere, but they all run on a single server computer at the University of Saskatchewan. Unfortunately, the Gradif code itself is not open source, and while we are licensed to run it on this machine, recent communications from Professor Nevieri indicate that he is unhappy with this level of open access to results produced using his Gradif engine. As a result, we have temporarily disabled public access.

In the future, we plan to completely re-implement the core engine for calculating efficiencies, according to the theory outlined in this thesis. This will allow us to optimize the the computation speed by employing per-calculation multi-threading and a modern high-performance programming language. This will also allow us to distribute a completely open version of the whole system, un-encumbered by licensing issues. Finally, we plan to combine this with Julian’s work and other upgrades to the usability of the web interface.

Nephier: A Program for Modelling Diffraction Grating Efficiencies

http://grating.theboots.ca/options.php

[Intro](#) | [Single Grating](#) | [Complex Scan](#) | [Mirror](#) | [Plot](#) | [Optimize](#) | [Files](#) | [Options](#)

Options

Numerical Accuracy

Number of Integration Steps ('0' for automatic)

Number of Fourier Coefficients

Number of Internally-propagating Wavefronts

Orders of Interest

Inside Orders

Outside Orders

Polarization

Polarization

Output

Working Folder

Log Filename

Set Options

beamteam.usask.ca dev: [\[email\]](#) [Mark Boots](#) [University of Saskatchewan](#)

Figure 4.4: This ‘Options’ page configures the numerical precision of the calculations, the diffraction orders of interest, and the polarization of the incident light. It also sets some other house-keeping options for where users want to store their data.

4.3 General trends and factors affecting efficiency

With these tools in-hand, we move on to the next question: What can we learn from them about the efficiency of gratings, especially those used in the soft x-ray regime?

This section looks at the theoretical effects caused by changes to grating parameters: groove profile, shape (depth, duty cycle, blaze angle, etc.), line density, coating material, coating thickness, and incidence angle. We can think of the grating efficiency as a scalar function of this many-dimensional parameter space, but it is impossible to capture its complexity in a simple analytical equation. None the less, the results of this section should give beamline designers an understanding of trends along each dimension within this space, and how to apply these trends to the optimization of gratings.

We attempt to isolate the effects of each parameter as much as possible. However, many parameters are linked together so that they cannot be made independent. For example, as we show in Section 4.3.1, gratings with triangular profiles have an optimal *blaze angle* which aligns the outgoing diffraction order with the specular reflection for maximum efficiency. For this type of grating, changing only the groove density will change the outgoing diffraction angle, and therefore change the optimal blaze angle. Simply plotting the efficiency as a function of groove density while holding all other parameters constant would confuse the blaze effect with the density effect; instead, we correct for this by adjusting the angle to keep the grating “on-blaze” as we vary the groove density in Figure 4.12.

All of the calculations in this chapter were computed with the differential method, using the software interface described in the previous section. Unless otherwise noted, results are shown for randomly polarized (natural) light, which is an average of the TM and TE efficiency; at grazing incidence, we did not find substantial differences between the two polarization cases. When we refer to 1st and 2nd order efficiencies without further clarification, the inside orders ($n < 0$) are assumed.²

4.3.1 Effect of grating profile: groove shape

As we showed in Chapter 3, any kind of periodic groove structure will have a diffraction effect, regardless of the nature of the groove shape. However, the grating efficiency – particularly in the order the experimenter wants to use – depends substantially on the groove shape.

Five common groove profiles are shown in Figure 4.5: a classic rectangular profile, a triangular profile (also known as a “sawtooth” or “blazed” pattern), a trapezoidal profile, a sinusoidal profile, and an approximated triangular profile.

²At grazing incidence, the outside orders are usually suppressed completely, since they would end up inside the grating. In the Rayleigh expansion (Equation 3.50), they end up as evanescent (decaying) rather than propagating orders.

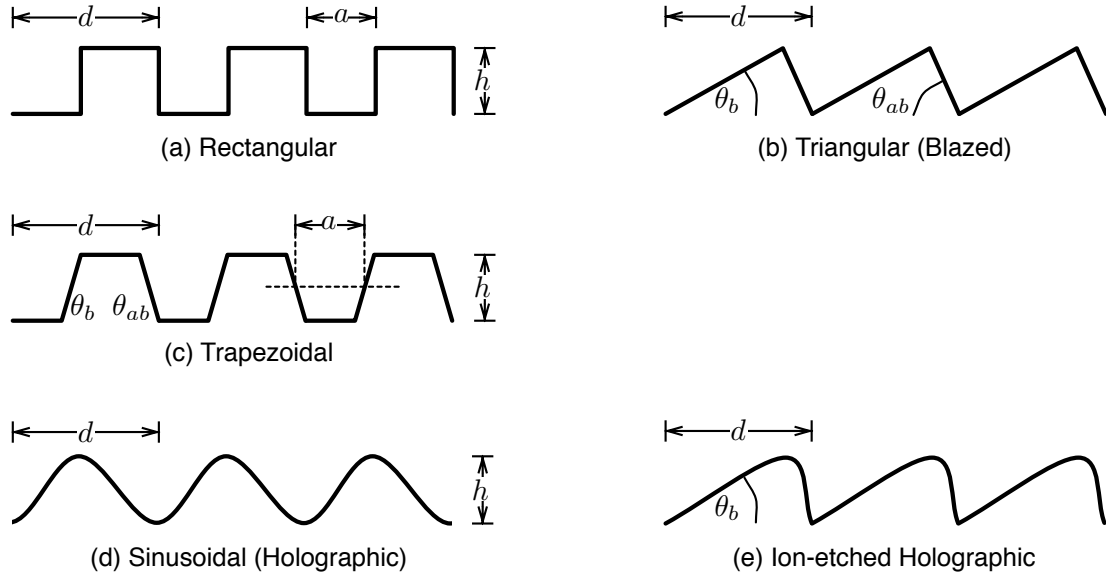


Figure 4.5: 5 common groove profiles and their geometry parameters. The rectangular profile (a) and triangular profile (b) are idealized versions of those produced by mechanical ruling. The trapezoidal profile (c) is usually produced accidentally while trying to rule a rectangular profile with an imperfect ruling tip. The sinusoidal profile (d) is the natural shape produced by holographic ruling; the result can be ion-etched to approximate a triangular profile (e).

Note on grating manufacturing techniques

These types of profiles emerged largely as a consequence of grating manufacturing techniques. To understand the impact of manufacturing on groove shape, we now take a brief look at two techniques for creating gratings: mechanical and holographic ruling.

Mechanical Ruling

In TODO, Henry Rowland invented a method for machining long, precise screws (TODO ref), and this enabled him to create a “ruling engine” (Figure 4.6) for mechanically scratching fine parallel lines into a layer of metal on a substrate material. His version was much more accurate than previous machines because it self-compensated for systematic errors in the screw pitch, and his efficient production of high-quality gratings “revolutionized spectroscopy” (TODO <http://www.aip.org/history/gap/Rowland/Rowland.html>). Today, there are several extremely precise ruling engines around the world, using diamond tips and interferometric position feedback to mechanically engrave groove densities approaching 3 000 lines/mm.³

The rectangular and triangular profiles in Figure 4.5 are a consequence of the shape of mechanical ruling tips. The trapezoidal profile is often produced accidentally when attempting to rule a rectangular profile with a non-ideal tip, as was the case for the gratings shown in Figures 4.22 and 4.23.

The setup and operation of mechanical ruling engines is a long, elite, and painstaking process; for gory details, see (TODO REF <http://gratings.newport.com/information/handbook/chapter3.asp>) by the Newport

³The Michelson ruling engine, now owned by the Newport Corporation, can rule up to an astonishing 10 800 lines/mm.

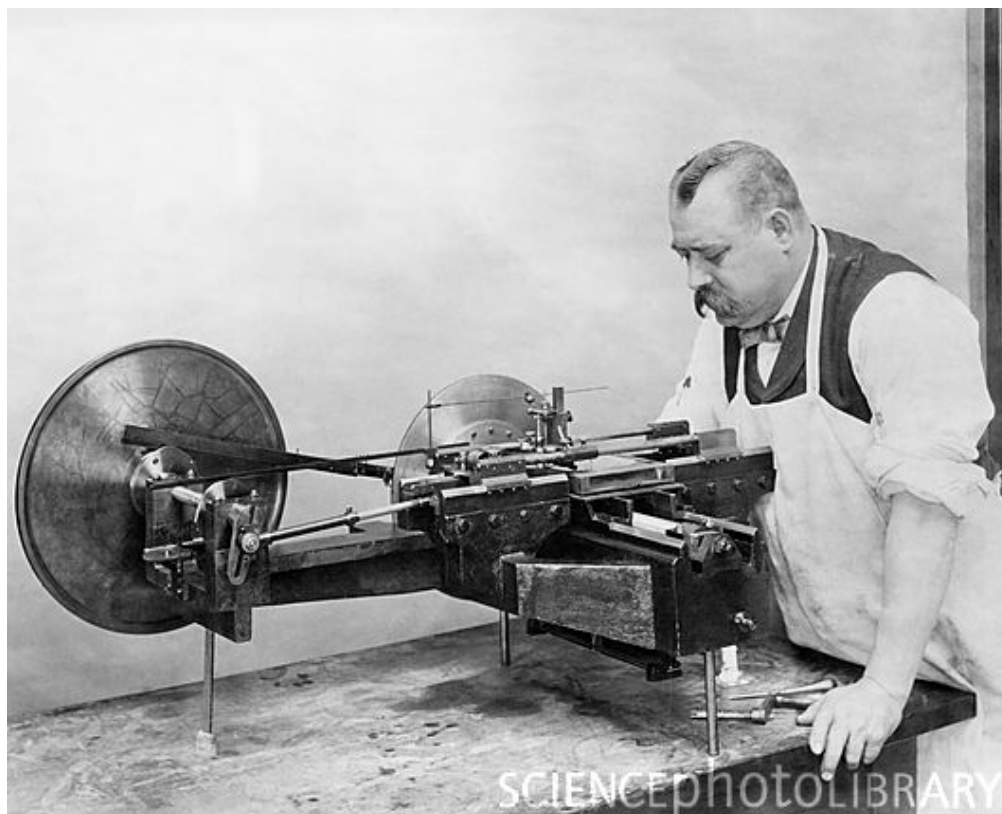


Figure 4.6: Henry Rowland's ruling engine, mechanically engraving a grating under the operation of his instrument maker Theodore Schneider. Photographed at Johns Hopkins University, Baltimore.
Image credit: EMILIO SEGRE VISUAL ARCHIVES/AMERICAN INSTITUTE OF PHYSICS/SCIENCE PHOTO LIBRARY (TODO ref <http://www.sciencephoto.com/media/150151/enlarge>)

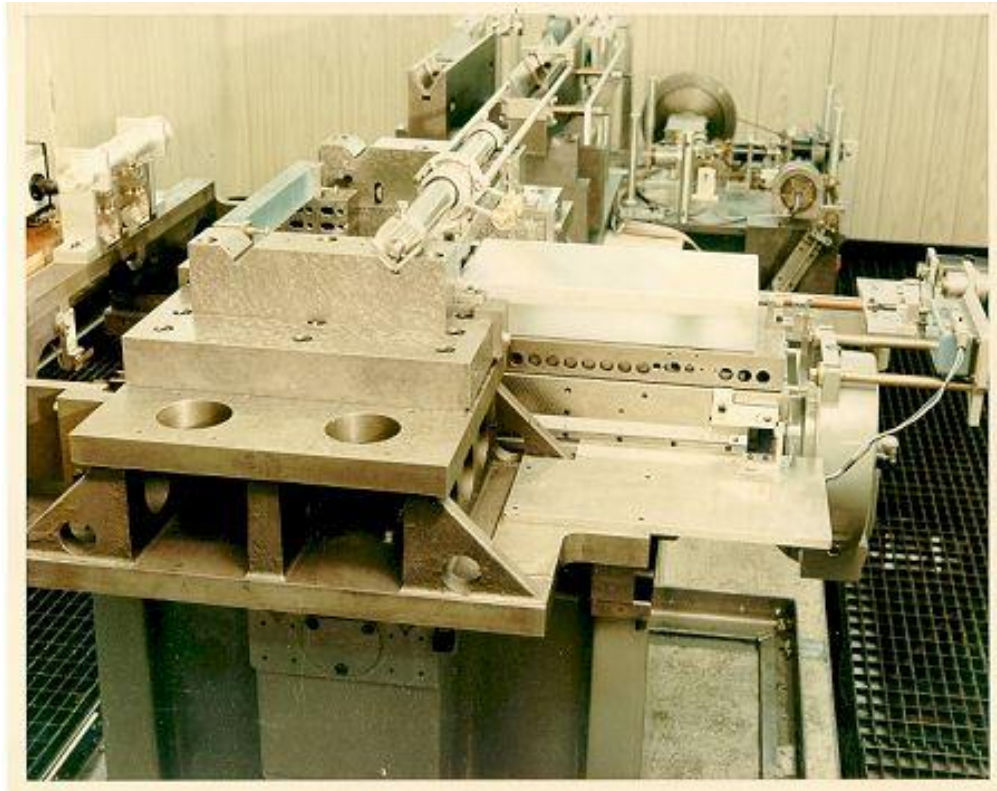


Figure 4.7: The MIT 'B' ruling engine, now owned and operated by Richardson Gratings (a division of the Newport Corporation). It can rule gratings up to 420 mm wide, with grooves up to 320 mm long. The maximum groove density is 1500 lines/mm. Equipped with a servo system for advancing the grating carriage and interferometric feedback using frequency-stabilized lasers, it is the most accurate ruling engine in the world. To control for thermal expansion of the engine, the room temperature is controlled to 0.005°C ; the system even compensates for changes in room air pressure since a change of just 2.5 mm of mercury will affect the refractive index of air (and therefore the interferometer wavelength) by one part per million. The entire engine is suspended from springs to dampen vibrations between 3Hz to 60Hz, which could otherwise be transmitted to the diamond tip. **Image credit:** DIFFRACTION GRATING HANDBOOK (TODO REF).

Corporation, which operates three ruling engines within its Richardson Grating Lab. To reduce the cost of ruled gratings, often a “master grating” is ruled mechanically and then used to create a mould for replicating other gratings; the groove shape is transferred using a thin layer of liquid resin which is hardened while in contact with the master grating surface (Figure 4.8).⁴

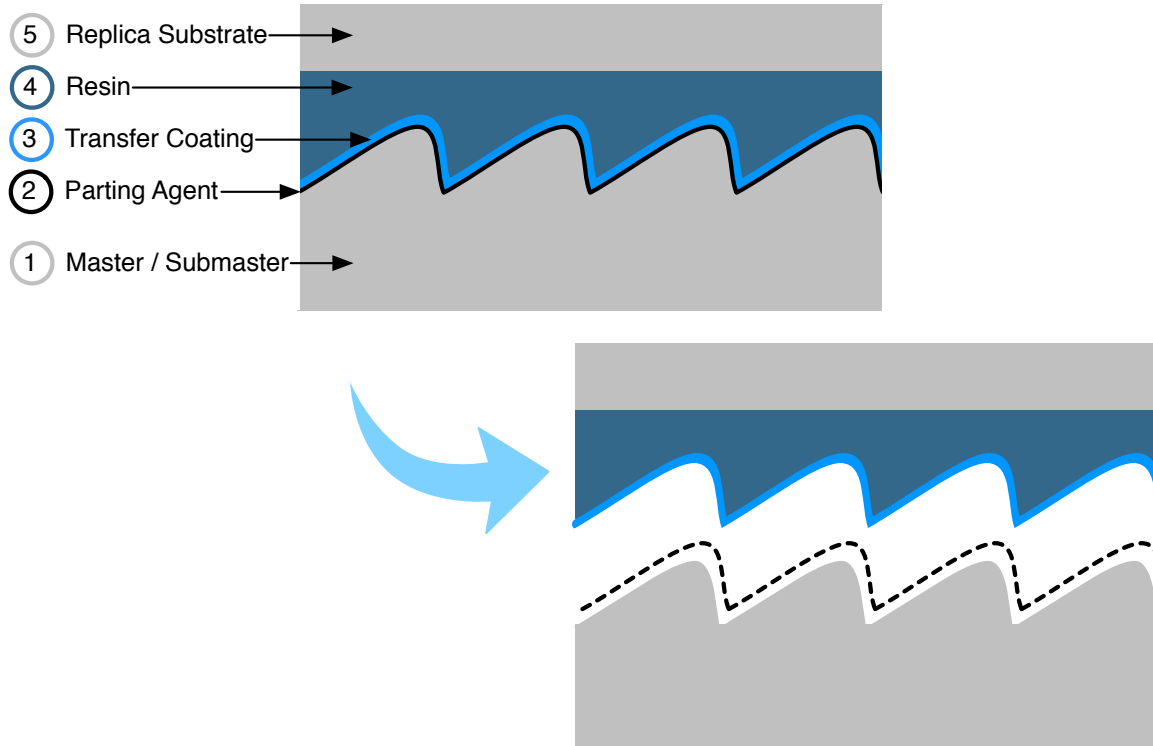


Figure 4.8: Master gratings can be replicated using a resin which hardens while in contact with the master (or subsequently, a submaster replicated from the first master). First, a parting agent (2) is applied to the surface of the master; it must be thin and uniform otherwise it will affect the profile. A metallic (aluminum or gold) coating about 1 μ m thick is then applied above the parting agent; this coating will eventually end up as the top surface of the replicated grating, and is called the *transfer coating* (3). Finally, the replica blank (5) is cemented from above using a resin ($\sim 10\mu$ m thick) that hardens under UV exposure or over time (4). Once the resin is cured, the gratings are separated at the parting agent layer, leaving the hardened resin in the shape of the grooves, with the metal coating adhered to the top. This will produce a mirror image of the master grating; to create a perfect replica, this first replica needs to be replicated again.

Holographic Ruling

A more recent technique was invented in the late 1960s for manufacturing gratings faster and with more repeatability. It uses two sources of coherent light to project a holographic interference pattern of regular standing waves onto a grating master. The grating master consists of a photoresist material that is either strengthened or weakened by exposure to light. After the master has been exposed to the interference pattern for a sufficient time, it is bathed in a developer chemical, which washes away either the exposed or unexposed

⁴The gratings used for the REIXS spectrometer were all master gratings. They were ruled directly into a smooth gold coating on top of a quartz grating blank, and then top-coated with an evaporated platinum or nickel surface.

parts, leaving behind a sinusoidal relief pattern that corresponds to the original intensity of light (TODO REF S. Lindau, "The groove profile formation of holographic gratings," Opt. Acta 29, 1371-1381 (1982).).

The last groove profile shown in Figure 4.5 represents an attempt to turn holographically-ruled sinusoidal gratings into triangular gratings using ion etching to partially eat away the groove surface while holding the finished photoresist master at an angle to the ion beam (TODO REF <http://www.tandfonline.com/doi/abs/10.1080/713819374>). Another technique for pseudo-blazed holographic gratings is known as Sheridan's Method (TODO REF N. K. Sheridan, "Production of blazed holograms," Appl. Phys. Lett. 12, 316-318 (1968).), which uses a transparent photoresist, exposed to the intersection of a coherent light source with its reflected self (Figure 4.9). Because the master is inclined relative to the interference pattern, the intensity profile is asymmetric and produces a lopsided sinusoidal shape.

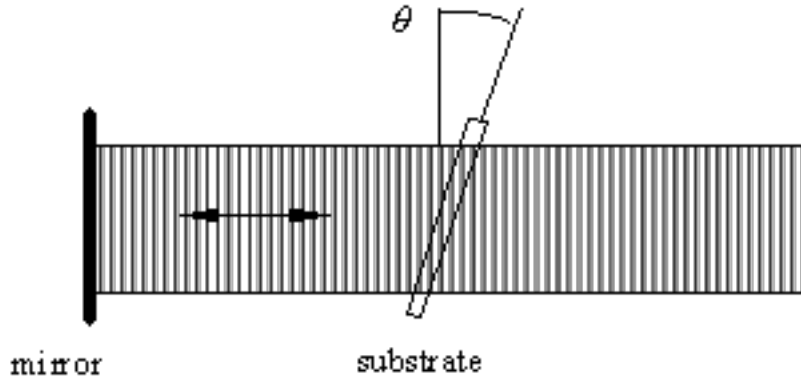


Figure 4.9: The Sheridan technique for recording pseudo-blazed holographic gratings uses a single light beam reflected back on itself to make a regular interference pattern of standing waves. The master substrate consists of a *transparent* photoresist material which is hardened or weakened by exposure to the light. By placing the substrate at an angle θ to the light path, the light and dark fringes are stretched out parallel to the grating surface; additionally, the angled incidence creates a lopsided sinusoidal intensity pattern that mimics blazed gratings. **Image credit:** DIFFRACTION GRATING HANDBOOK (TODO REF).

Profile geometry

Figure 4.5 shows the parameters that describes that describe the geometry of each profile. In addition to the groove spacing d , rectangular gratings are characterized by a groove depth h (or duty cycle) and a groove width a . Ruled triangular gratings are described by their blaze angle θ_b , and the opposite angle (or “anti-blaze angle”) θ_{ab} .⁵ Trapezoidal gratings are described by a groove depth h , a groove width a , and their blaze and anti-blaze angles θ_b and θ_{ab} . Sinusoidal gratings are fully described by just their groove depth h , and an assumption of a sinusoidal variation $y(x) = y_0 + \frac{h}{2} \sin(2\pi x/d)$.

⁵Ideally the anti-blaze angle should be 90° , but it is usually less than 30° due to constraints on the ruling tip shape.

Blazed optimization for triangular gratings

The triangular profile in Figure 4.5 (b) is much more than an accidental artifact of mechanical ruling. This shape is optimal for concentrating as much energy as possible into a single order, and therefore boosting the grating efficiency in that order. Intuitively, we might imagine that to increase efficiency, we should line up the direction of classical “reflection” off the majority of the grating surface with the direction of the diffracted ray. Still thinking classically, we might also want to minimize shadowing in the corners of the grooves.

The ideal blazed grating meets both of these criteria. By carefully choosing a blaze angle θ_b we can – at least at one wavelength of interest – line up the specular reflection of the angled surface with the diffraction direction in order n . Using the law of reflection from geometric optics ($\theta_{\text{incident}} = \theta_{\text{reflected}}$), we can easily⁶ derive the optimized condition for a blazed grating. From the geometry in Figure 4.10, where N' is normal to the angled surface:

$$\theta_{\text{incident}} = \theta_{\text{reflected}} \quad (4.1)$$

$$\theta_2 - \theta_b = \theta_{2,n} + \theta_b \quad (4.2)$$

$$\theta_{2,n} - \theta_2 = -2\theta_b \quad (4.3)$$

Applying a trigonometric identity to the grating equation (3.61):

$$n\lambda/d = \sin \theta_{2,n} - \sin \theta_2 \quad (4.4)$$

$$\frac{n\lambda}{2d} = \cos \left(\frac{\theta_{2,n} + \theta_2}{2} \right) \sin \left(\frac{\theta_{2,n} - \theta_2}{2} \right) \quad (4.5)$$

$$\frac{n\lambda}{2d} = \cos \left(\frac{\theta_{2,n} + \theta_2}{2} \right) \sin (-\theta_b) \quad (4.6)$$

$$(4.7)$$

or

$$\theta_b = -\arcsin \left(\frac{n\lambda}{2d \cos \left(\frac{\theta_{2,n} + \theta_2}{2} \right)} \right) \quad (4.8)$$

Textbooks and resources on beamline design universally provide this derivation and formula for the optimal blaze angle θ_b (TODO ref: CXRO x-ray data book, diffraction grating handbook, gratings slits and mirrors). Using efficiency calculations, we have confirmed that this intuitive argument is a very good approximation for what happens in the full electromagnetic picture; the actual ideal blaze angle is usually slightly but insignificantly lower. For a 1200 line/mm grating used at an incidence angle of 88 degrees with 400 eV photons in the first inside order ($n = -1$) (Figure 4.11), Equation 4.8 would recommend a blaze angle of 1.67°. We used this as the starting point to conduct a software optimization using efficiency calculations, and were only able to increase the 1st order efficiency from 16.2% to 16.8% by reducing the blaze angle from 1.67° to the optimal 1.46°.

⁶Setting up a ruling engine to correctly and accurately engrave this angle is another story...

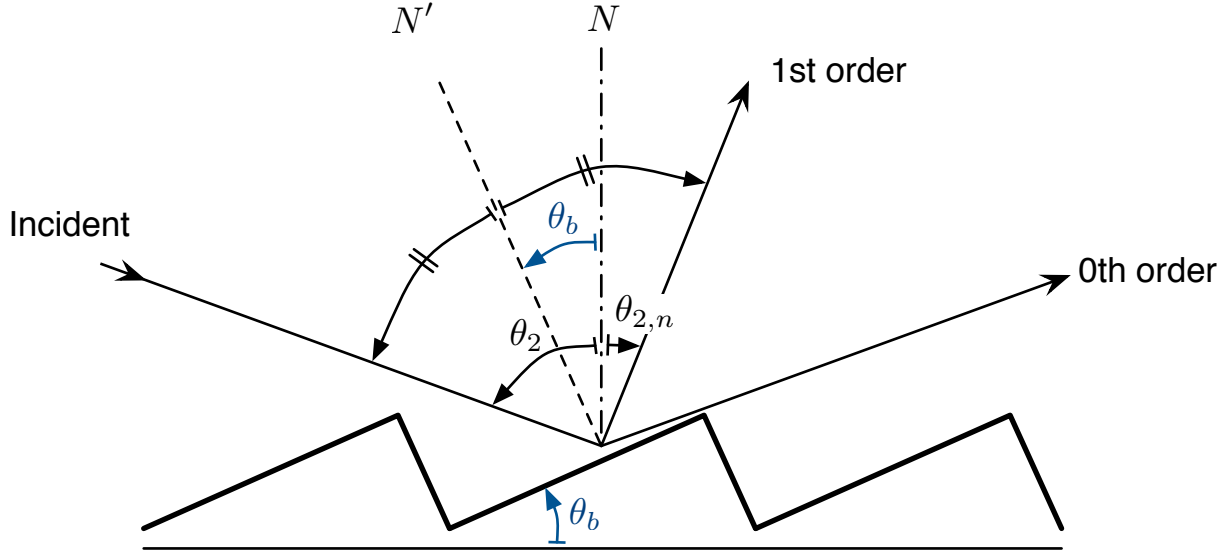


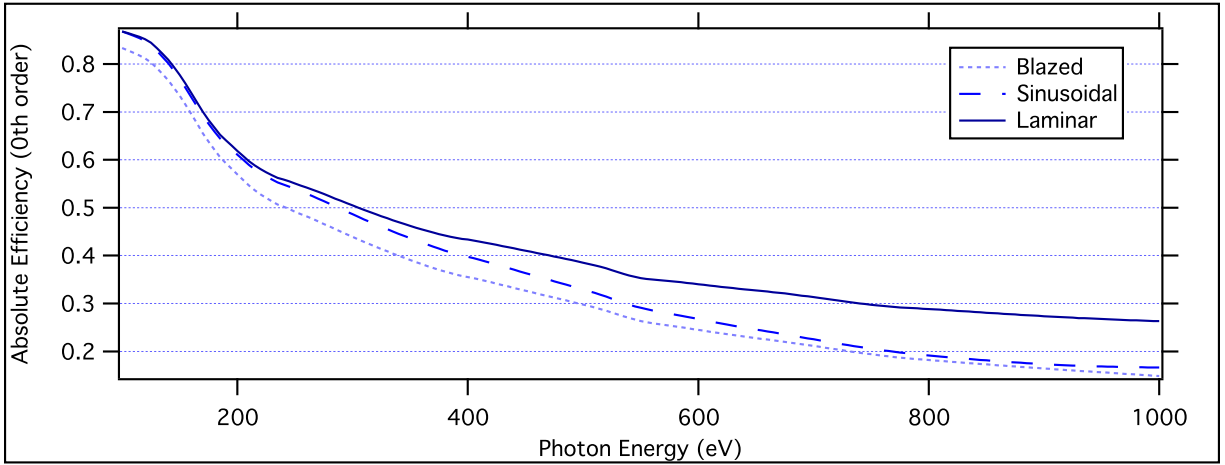
Figure 4.10: In the blazed condition, the desired order diffraction angle – in this case, 1st order – is aligned with the direction of specular reflection off the groove surfaces.

Because the blaze angle depends on the $n\lambda$ term in the grating equation, a grating optimized for a wavelength x in 1st order will also be optimized for a wavelength $x/2$ in 2nd order (or, in terms of energy, optimization for x eV in 1st order would imply optimization for $2x$ eV in 2nd order). We can confirm this for the blazed grating in Figure 4.11, where the 1st-order efficiency peak occurs at 450 eV, and the 2nd order efficiency peak occurs near 900 eV.

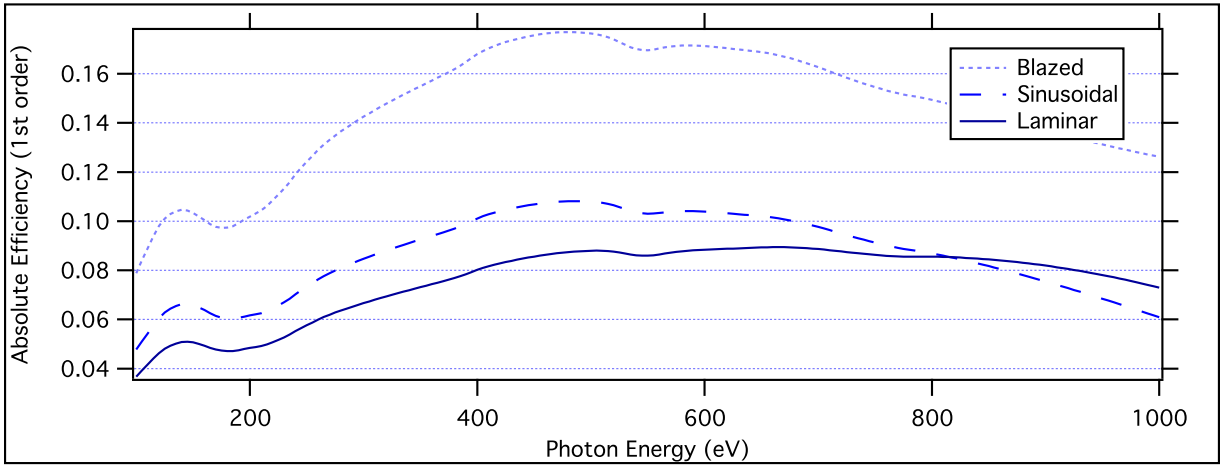
Efficiency comparison of common profiles

For comparison, Figure 4.11 shows the 0th order, 1st order, and 2nd order efficiency for three common grating profiles: blazed, sinusoidal, and rectangular (commonly referred to as *laminar*). All three gratings have a groove density of 1200 lines/mm, are shown at an incidence angle of 88 degrees, and have had their geometry optimized for maximum efficiency in 1st-order with 400 eV photons. (The coating is platinum, and the substrate is quartz [SiO₂].) The blazed grating was optimized by adjusting the blaze angle; the sinusoidal grating by adjusting the groove depth, and the rectangular grating by adjusting the groove depth and assuming a duty cycle of 50%.

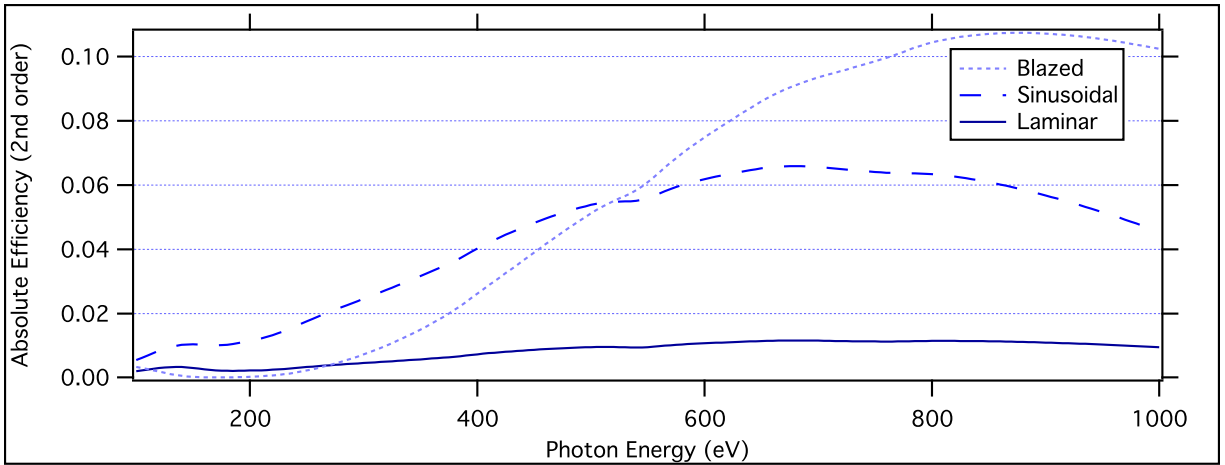
The blazed profile is substantially superior to both the sinusoidal and laminar alternatives. In first order, even though the efficiency curve peaks near the design energy of 400 eV, the performance is better across the entire range from 100 eV to 1000 eV (and beyond). The blaze effect causes this curve to be shifted up in energy by a factor of two in 2nd order, so that again the blazed grating out-performs the other profiles, but only above 500 eV. The sinusoidal grating has relatively flat efficiency across the energy range, even though it still shows the energy-dependence of its optimization for 400 eV. (we have chosen a platinum coating for these demonstrations since its reflectivity is relatively constant across the energy range; see Figure 4.16. The



(a) 0th Order



(b) 1st Order



(c) 2nd Order

Figure 4.11: 0th order, 1st order, and 2nd order efficiency of three different groove profiles, all optimized for use at 400 eV. The blazed grating is superior in both 1st and 2nd order. All gratings: 1200 lines/mm, Platinum coating. Blazed: 1.46° angle, 60° anti-blaze angle. Sinusoidal: 13.7 nm groove depth. Laminar (rectangular): 9.6nm groove depth, 50% duty cycle.

small universal dip in efficiency at 180 eV is due to a drop in the Pt reflectivity here.)

4.3.2 Effect of groove density

Because the groove density directly affects the angular dispersion, using a higher-density grating is the most direct path to designing a higher-resolution instrument (Section 2.2.2). Unfortunately, Figure 4.12 shows that increasing the groove density universally decreases the grating efficiency in all orders except the 0th order, even when the remaining parameters are adjusted to keep the grating optimized. This turns out to be true, not only in this example for two grating profiles, but as a general principle. Intuitively, we can argue that as the groove density approaches infinite, the grating will look more and more like a flat mirror – with microstructure becoming smaller and smaller. Therefore, it makes sense that the amount of light in the 0th-order specular reflection will increase at the expense of the diffracted orders.

Figure 4.13 explores the groove density effect in more detail, with an efficiency spectrum for a series of blazed gratings from 300 lines/mm to 2700 lines/mm, all optimized for 400 eV at 88° incidence. It confirms that as the groove density increases, the 0th order efficiency increases, and the $n \neq 0$ order efficiencies decrease. However, one fortunate outcome is that as the groove density increases, the width of the efficiency peak caused by the blazing optimization becomes wider; therefore, higher groove-density blazed gratings can be used optimally over a wider energy range than low-density gratings.

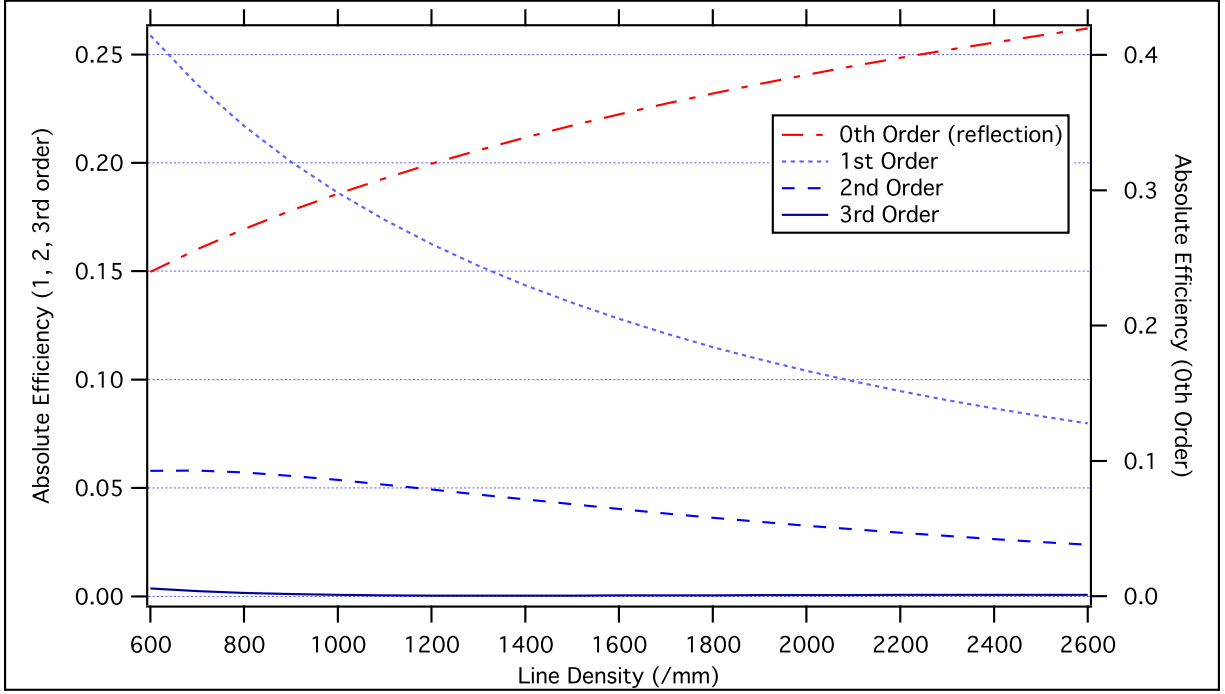
4.3.3 Effect of coating thickness

Gratings intended for use in soft x-ray instruments are manufactured on precision-ground blanks, usually consisting of fused quartz (SiO_2) or other amorphous glasses. The insulating (dielectric) blank is coated in a layer of metal, where the smoothness of the surface is absolutely critical. Often gold is used as a first coating, since it can be applied with very low roughness, and because it provides a soft layer in which to rule the grooves. If another type of coating is required (such as nickel and platinum, in our case), these coatings are applied on top of the gold after ruling.

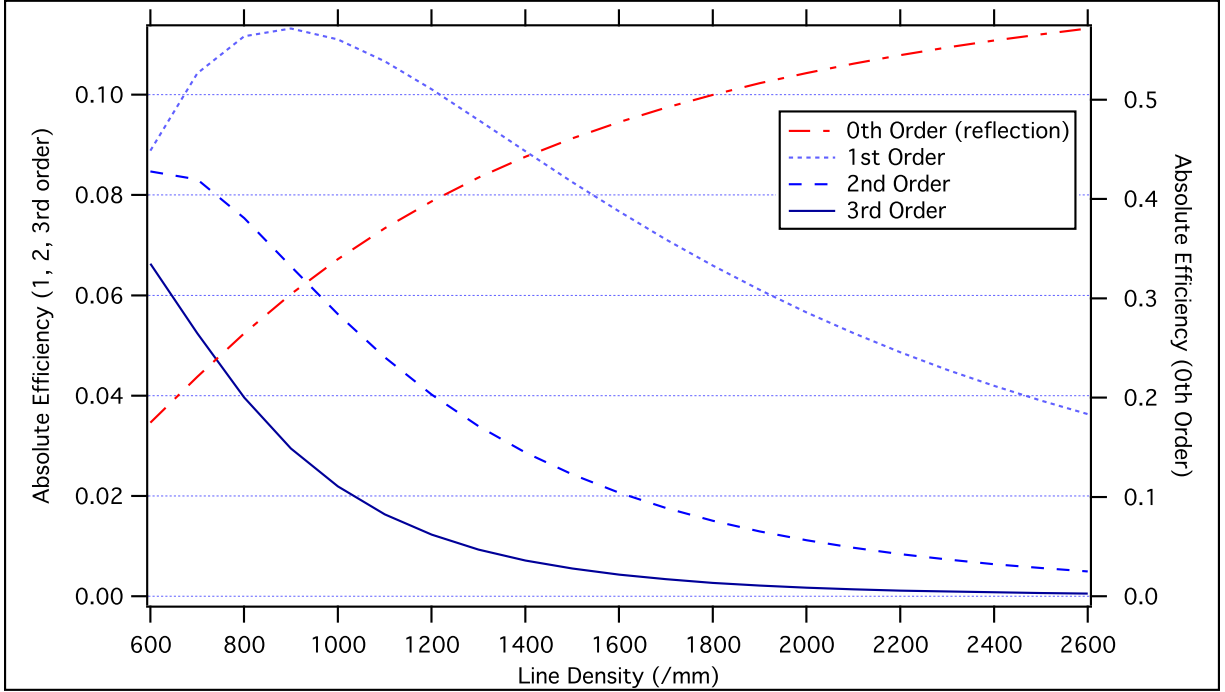
The required thickness of the coating is another question that can be answered by efficiency calculations. Thin coatings can be applied more smoothly than thick ones (TODO ref Gratings Slits and Mirrors), so the question is: how thick must a coating be for a given photon energy and incidence angle, so that photons are fully reflected or absorbed before reaching the substrate interface? If the coating is too thin, the absorption characteristics of the glass oxide substrate will start to show up in the efficiency spectrum.

Figure 4.14 shows calculations for various thicknesses of platinum coatings above an SiO_2 substrate, compared with a theoretical solid platinum grating of infinite thickness. The 0.5nm and 1nm coatings show the oxygen absorption edge at 525 eV, as well as significantly reduced reflectivity over the whole energy range. The 5 nm layer shows a thin-film interference effect that actually boosts the efficiency above 600 eV.⁷

⁷The sharp peak in this spectrum at 525 eV might be anomalous; the Henke data – from which we derive the complex refractive index for all these materials – is admittedly not accurate in the immediate vicinity of absorption edges.



(a) Blazed grating, maintaining the blaze condition as the groove density changes.
Platinum coating, 88-degree incidence, 400eV photon energy.



(b) Sinusoidal grating. Groove depth optimized at 1200 lines/mm; maintaining the depth-to-period ratio as the line density changes. Platinum coating, 88-degree incidence, 400eV photon energy.

Figure 4.12: Increasing the groove density always decreases the diffraction efficiency – at least for all the useful orders ($n \neq 0$). In these plots, we have tried to control for inter-related factors: For the blazed grating in (a), the blaze angle has been adjusted with the groove density (using Equation 4.8) to maintain the on-blaze condition. In (b), the sinusoidal grating depth was optimized at 1200 lines/mm, and then the depth-to-period ratio was maintained across changes to the groove density.

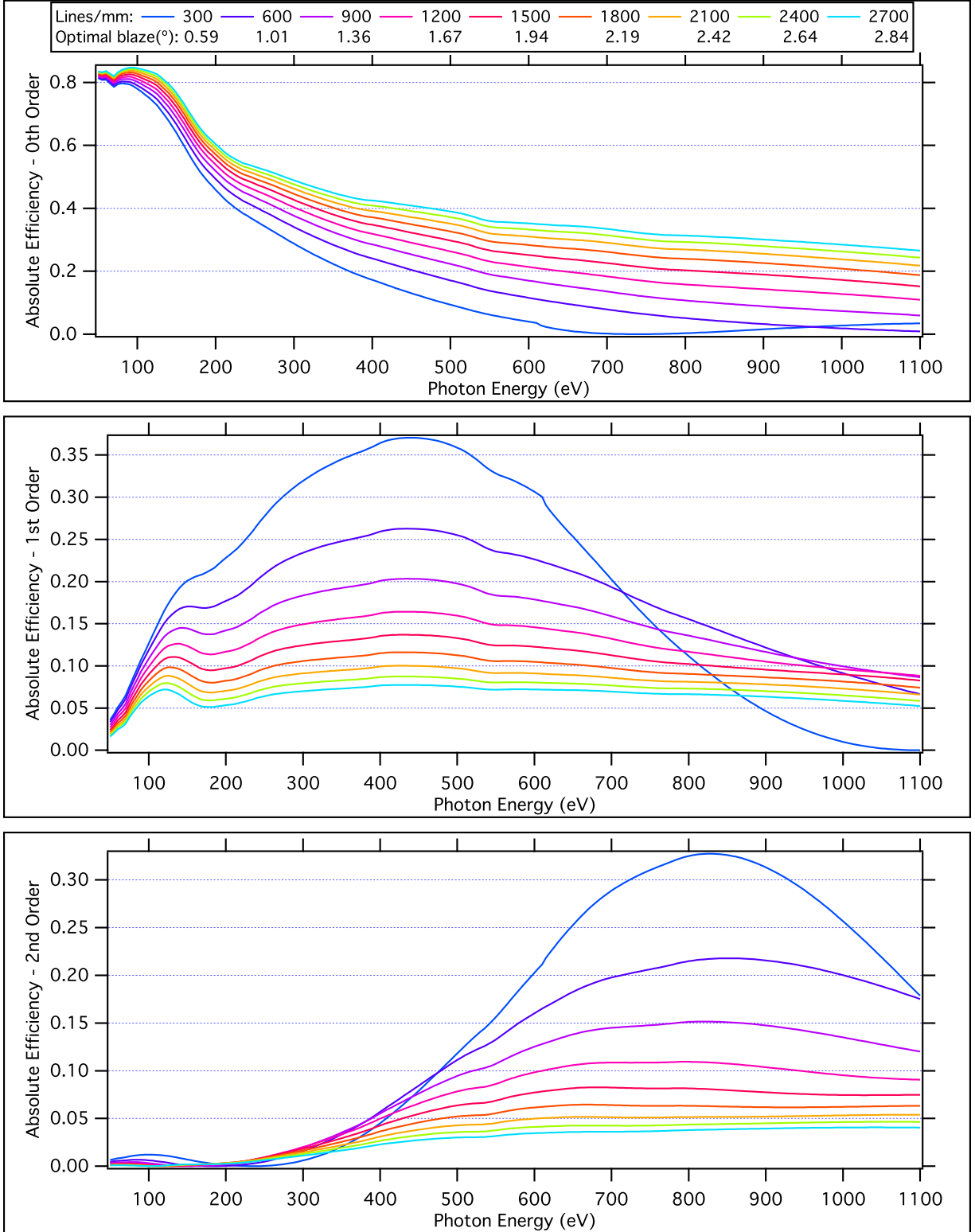
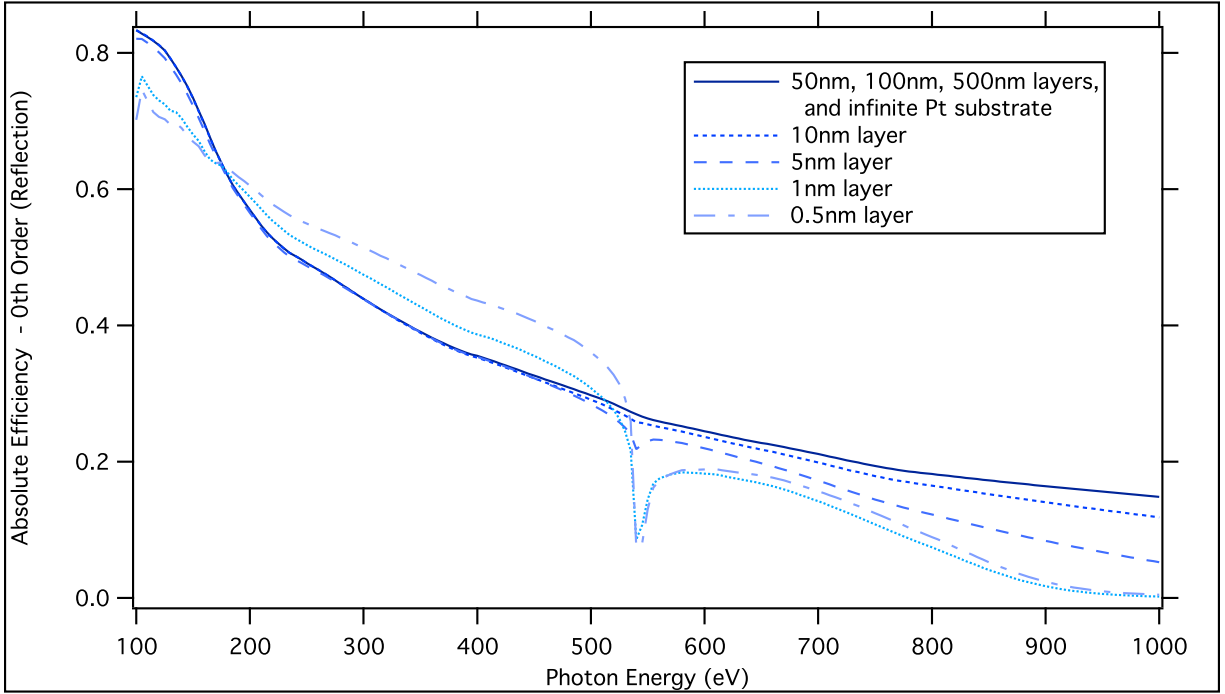
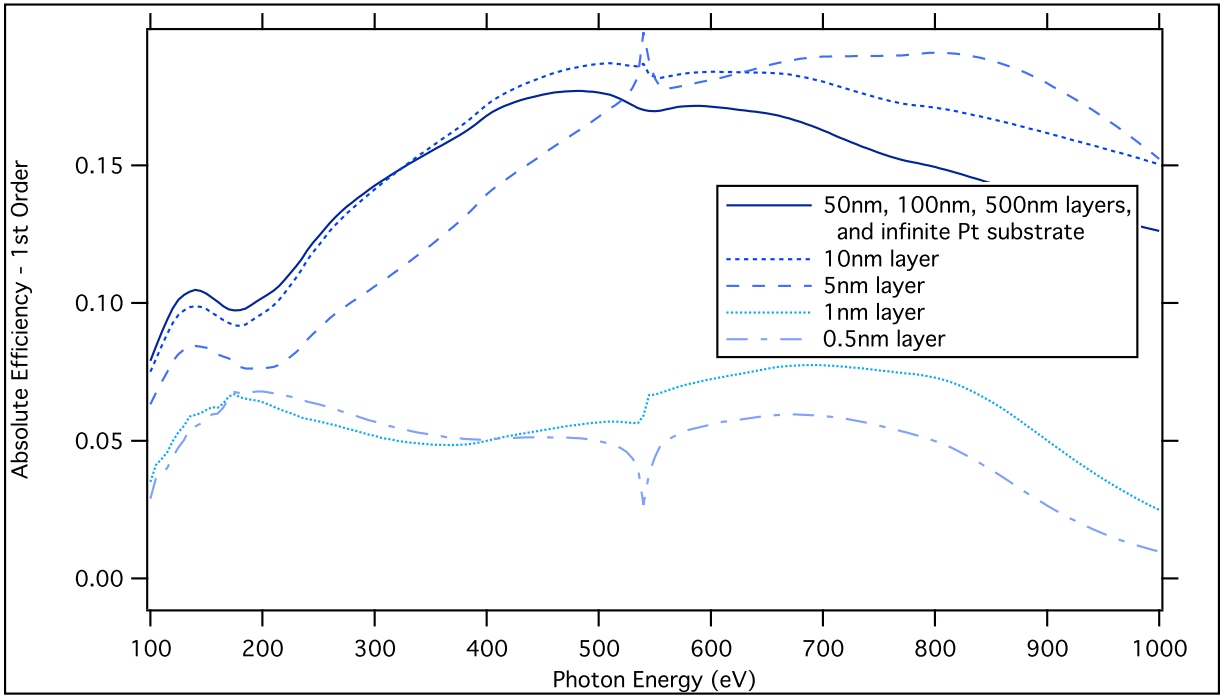


Figure 4.13: 0th order, 1st order, and 2nd order efficiency as a function of energy, for a range of groove densities from 300 to 2700 lines/mm. All gratings are triangular, platinum-coated, with an optimal blaze angle dependent on the groove density according to Equation 4.8. (Blaze angles are shown in the legend.) As the groove density increases, the maximum achievable efficiency drops, but the bandwidth of the blaze-optimization peak becomes wider.



(a) 0th Order



(b) 1st Order

Figure 4.14: In the soft x-ray regime under grazing incidence, metal-coated dielectric gratings are indistinguishable from pure metal gratings... as long as the coating is thicker than $\sim 20\text{nm}$ (although the exact thickness depends on the material, photon energy, and incidence angle). These calculations show Pt coatings of varying thickness over an SiO_2 substrate, as well as an infinitely thick pure Pt grating. (Blazed grating, 1200 lines/mm, 1.46° blaze angle, 88° incidence).

As we should expect, at a thickness of 50nm and above, the coated gratings become indistinguishable from an infinitely-thick platinum substrate.

In general, the required minimum thickness will depend on the photon energy, incidence angle, and the x-ray form factor of the coating material – all of which affect the x-ray penetration depth. These results show that for thin coatings, the efficiency calculations are able to rigorously incorporate the effects of interference and absorption at the interface with the substrate.

4.3.4 Comparison of coating materials

All materials suffer from inherently low reflectivity at soft x-ray energies. Even when gratings are used at grazing incidence, designers must carefully choose coating materials to maximize efficiency considering the desired wavelength range of the instrument. (This becomes particularly frustrating when a material with otherwise high reflectivity has an absorption edge right in the middle of the region of interest.)

To help in selecting materials, Figures 4.15 and 4.16 show several possibly grating coatings: carbon, nickel, gold, platinum, and iridium. (Figure 4.15 shows the reflectivity of a plain mirror made out of these materials over the energy range from 100 to 1000 eV, at 88° grazing incidence. Figure 4.16 compares the mirror reflectivity with the 0th order and 1st order efficiency of a sinusoidal grating, which had its groove depth optimized for 400 eV.)

The heavy precious metals (Au, Pt, Ir) are commonly chosen for grating coatings because they have a relatively constant reflectivity over this energy range. This is because their core-level electrons are so tightly bound that their strongest absorption features occur well above the soft x-ray range. (For example, the Pt K 1s absorption edge is at 78.4 keV.) Their outer-shell electrons fall within the soft x-ray range (for example, the platinum N and O transitions), but these absorption features are not nearly as strong, and therefore do not seriously affect the reflectivity. Gold has better reflectivity than Pt and Ir below 200 eV, and also has the previously-mentioned desirable property of being easy to apply smoothly and rule mechanically. Above 200 eV, platinum has been the de-facto choice for high-energy wide-bandwidth gratings for many years. Iridium (and rhodium, not shown) actually have even better reflectivity and corrosion resistance than platinum, and are becoming standard coating options with some manufacturers.

In contrast, carbon and nickel offer much higher reflectivity over some parts of this energy range, but unfortunately have strong absorption features right in the middle. The carbon K 1s absorption edge at 284 eV makes it restricted to, but excellent for, low-energy applications. The nickel L₂/L₃ edges do not occur until 870/853 eV, and Figure 4.16 seems to suggest that nickel would be the clear winner over much of the soft x-ray range. This prompted us to use it for two of the REIXS spectrometer gratings, with one obvious but unforeseen consequence (Section ??).

Not shown in these plots, silicon also has a very high reflectivity up to its L₂/L₃ absorption edge at 100 eV. Therefore, bare (uncoated) SiO₂ mirrors are often used for extreme ultra-violet (EUV) and very low-energy soft x-ray beamlines (TODO REF Gratings, Slits and Mirrors); Si-coated gratings might be useful here as

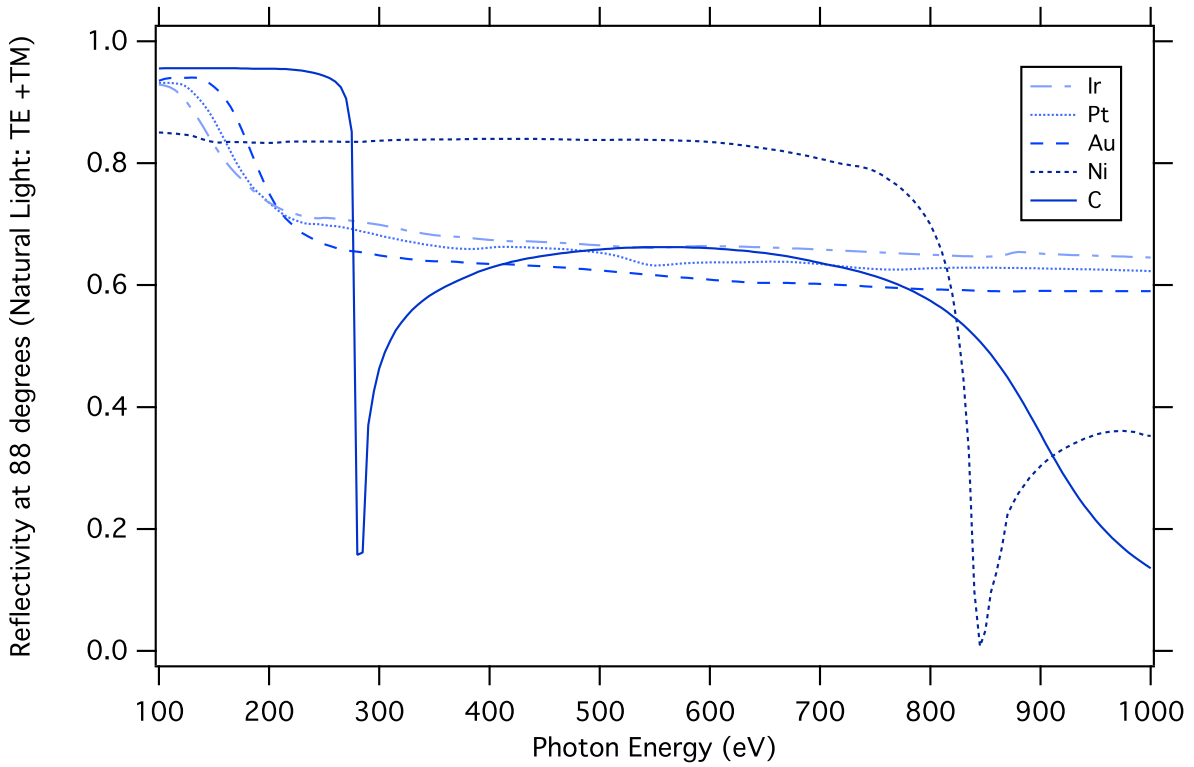


Figure 4.15: The reflectivity of a pure mirror at grazing incidence (88°), as a function of photon energy. Lighter elements like carbon and nickel have the highest peak reflectivity, but have strong absorption features. Heavier metals, particularly those within the platinum group, have reasonable reflectivity over the entire soft x-ray region of interest. Up to 200 eV, gold has a higher reflectivity than Pt and Ir.

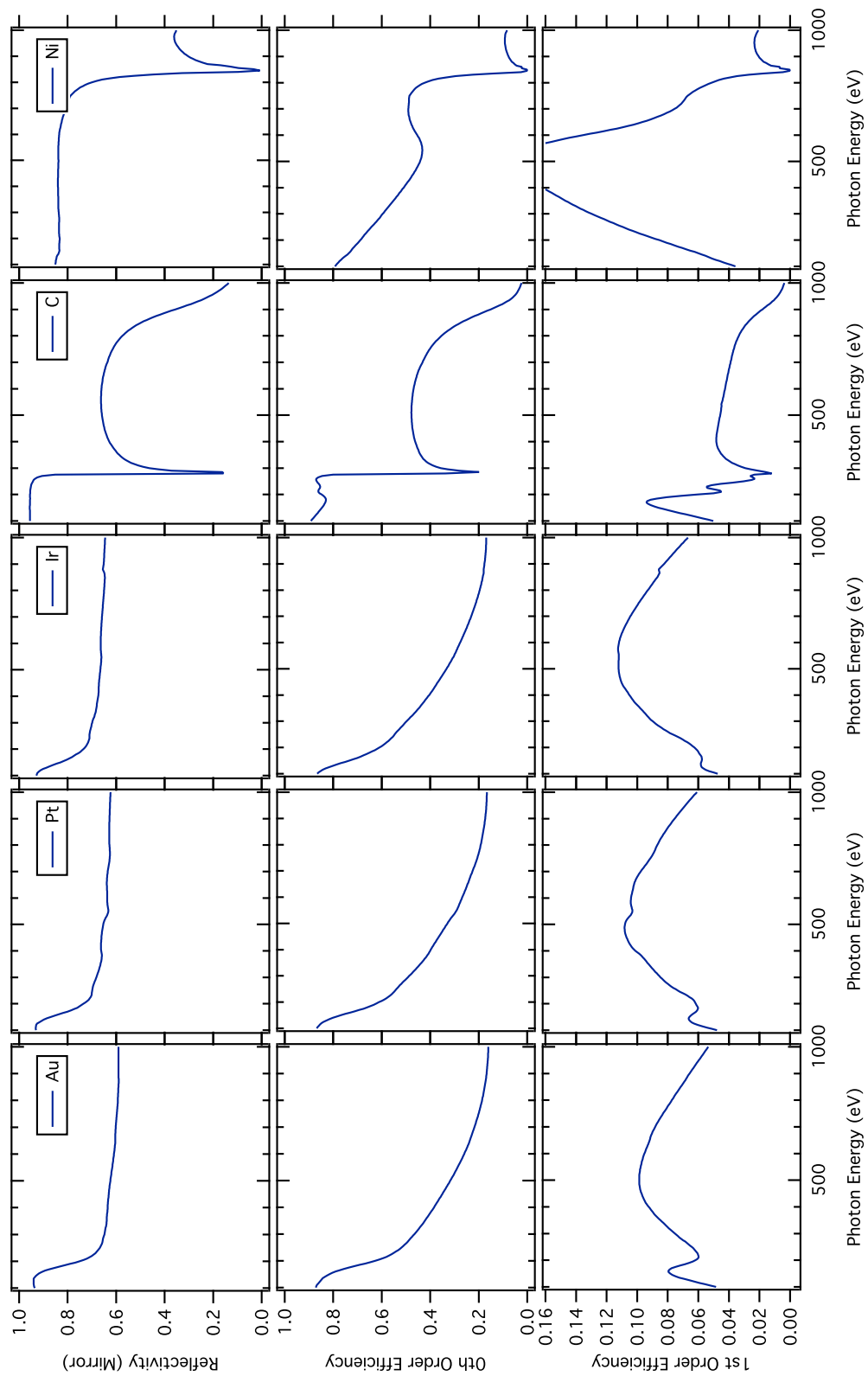


Figure 4.16: A comparison of the mirror reflectivity, 0th order, and 1st order efficiency for different coating materials, as a function of photon energy. (Gratings: Sinusoidal profile, 88° incidence angle, 1200 lines/mm, 13.7 nm groove depth.) Note that the 1st order efficiency has energy-dependent features that are not visible in the simple reflectivity.

well.

4.3.5 Effect of photon energy / wavelength

The energy-dependence (or wavelength-dependence) of grating efficiency has been shown in many of the previous plots, where we have displayed the efficiency as a function of photon energy. However, it is impossible to isolate trends for this relationship on its own, because the photon energy is inherently coupled to the grating efficiency in multiple ways. For starters, the complex refractive indexes of grating materials always vary as a function of energy. Additionally, the photon energy also determines the angle of the outgoing diffraction orders, which can be seen in both the Rayleigh expansion for the total field, and in the simplified grating equation (Equation 3.61). Therefore, optimizations for geometry parameters that depend on outgoing angles – like the blaze angle and groove depth – are inherently coupled to the photon energy. The plots in Figure 4.16 highlight this by showing the difference between the energy-dependent reflectivity of a plain flat mirror, versus the more complicated diffraction efficiency.

4.3.6 Effect of incidence angle

In the soft x-ray regime, the real part of the refractive index for metals is less than unity. This means that the phase velocity for light in the material is actually *faster* than the speed of light in a vacuum.⁸ As mentioned in Section 2.2.3, we can exploit this lucky phenomenon to increase the reflectivity of gratings and mirrors by using them at grazing incidence, to create what is sometimes referred to non-rigourously as “*total external reflection*” (TER).

Total internal reflection (TIR) happens in conventional materials when a light ray travels from a slower optical medium (refractive index n_1) toward a faster optical medium (refractive index $n_2 < n_1$). Snell’s law of refraction would relate the angles of the incident (θ_1) and transmitted (θ_2) waves:

$$n_1 \sin \theta_1 = n_2 \sin \theta_2 \quad (4.9)$$

$$\sin \theta_2 = \frac{n_1}{n_2} \sin \theta_1 \quad (4.10)$$

By choosing an incident angle θ_1 for which there is no possible solution to θ_2 , we can ensure that there is no transmitted wave – the incident wave must be completely reflected.

$$\frac{n_1}{n_2} \sin \theta_1 > 1 \quad (4.11)$$

This will happen for all incident angles θ_1 beyond a critical angle:

$$\theta_{\text{critical}} = \arcsin\left(\frac{n_2}{n_1}\right) \quad (4.12)$$

⁸The non-zero imaginary part of the refractive index ensures that the transmitted wave decays and is absorbed, therefore Einstein’s speed limit is not violated.

In the case of soft x-ray mirrors and gratings, if we make a *very large approximation* and ignore the imaginary component of the mirror's refractive index, the same situation happens when light from the (slower) vacuum is incident on the (faster) medium of the mirror.⁹ Here the vacuum refractive index is $n_1 = 1$, and the mirror refractive index is $n_2 < 1$. (For example, at 410 eV, the real part of the refractive index of platinum is $\tilde{n} = 0.99321$.) We can therefore calculate the critical angle for *total external reflection*; for incident angles larger than this, there should be no transmitted wave into the mirror:

$$\theta_{\text{critical}} = \arcsin(\tilde{n}) \quad (4.13)$$

(where \tilde{n} is the real part of the mirror's complex refractive index.) Critical angles for the coatings in Figure 4.16 at 410 eV are given in Table 4.19.

Because we ignored the imaginary component ($i\beta$) of the full refractive index ($n = \tilde{n} + i\beta$), the concept of TER is just an approximation for what happens in the rigorous electromagnetic picture. The imaginary component represents absorption of the electromagnetic wave within the material, and as a result, no soft x-ray mirrors are ever totally reflecting – Figure 4.17 shows that a reflectivity of 1 only occurs at complete grazing incidence (90°). For those that are interested, (TODO REF modern optics) gives a rigorous derivation of reflection and transmission at interfaces with absorbing materials: the reflection coefficients for TE and TM polarization, off a material with complex refractive index n at incidence angle θ , are known as the *complex Fresnel equations*:

$$\cos \phi \equiv \sqrt{1 - \frac{\sin^2 \theta}{n^2}} \quad (4.14)$$

$$r_{TE} = \frac{\cos \theta - n \cos \phi}{\cos \theta + n \cos \phi} \quad (4.15)$$

$$r_{TM} = \frac{-n \cos \theta + \cos \phi}{n \cos \theta + \cos \phi} \quad (4.16)$$

In general, the reflection coefficients r_{TE} and r_{TM} are also complex, so they give both the amplitude and phase shift of the reflected electric field vector. The reflectivity R is given by the squared magnitude of the reflection coefficient:

$$R_{TE} = |r_{TE}|^2 = r_{TE} \cdot r_{TE}^* \quad (4.17)$$

$$R_{TM} = |r_{TM}|^2 = r_{TM} \cdot r_{TM}^* \quad (4.18)$$

These are plotted in Figure 4.17 as a function of incidence angle for a perfect platinum mirror at 410 eV.

Moving from mirrors to gratings, Figure 4.18 shows the effect of incidence angle on diffraction efficiency for several different geometry profiles. Even though TER is a crude approximation, this figure does confirm that the grating efficiencies in the 0th, 1st, and 2nd orders are indeed extremely low below platinum's “critical

⁹This assumption is necessary because Snell's law in the form $n_1 \sin \theta_1 = n_2 \sin \theta_2$ only makes sense for real n . If n_1 and θ_1 were real, but the mirror's n_2 was complex, this would require a complex “angle” θ_2 , which would have no easy physical interpretation.

Table 4.1: Critical incidence angles for “total external reflection” at 410 eV for the mirror and grating coatings shown in Figure 4.16.

Material	θ_{critical} for TER (°)
Carbon (C)	85.92
Nickel (Ni)	83.20
Gold (Au)	83.85
Platinum (Pt)	83.32
Iridium (Ir)	83.10

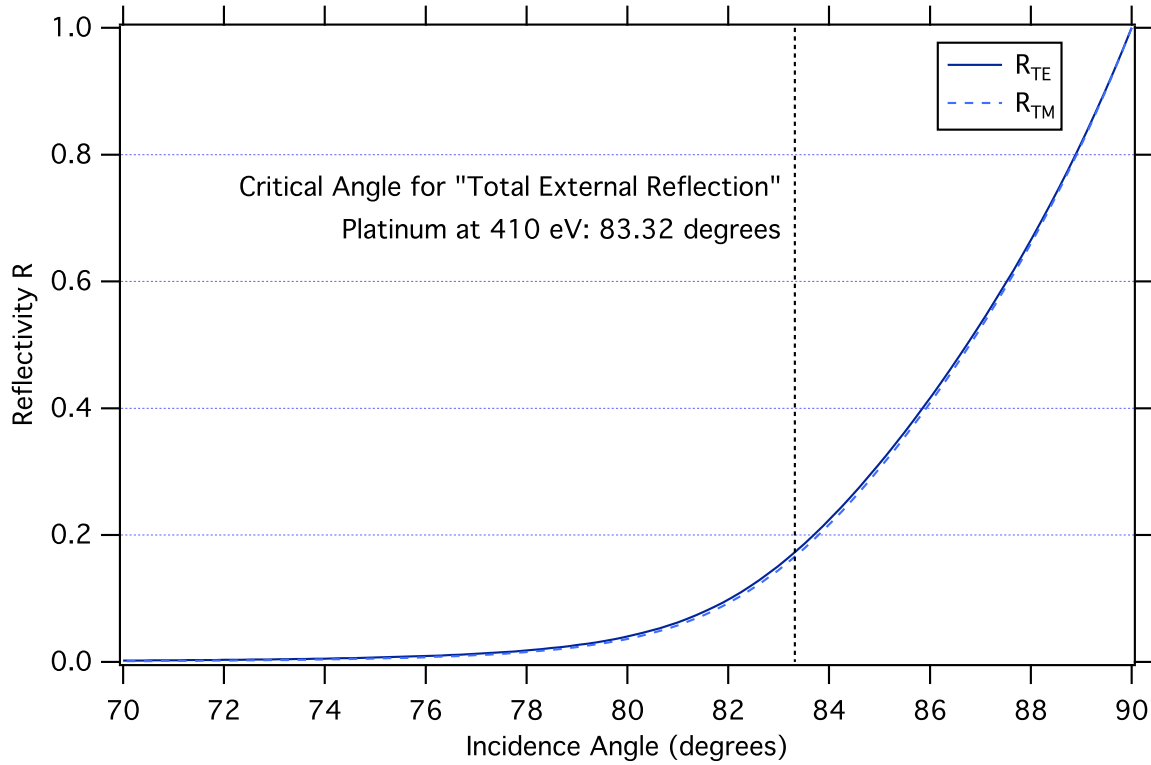


Figure 4.17: The reflectivity of a perfect platinum mirror as a function of incidence angle at 410 eV, calculated using the complex refractive index and the complex Fresnel equations. The “total external reflection” approximation suggests a critical angle of 83.3° for total reflection, but due to absorption within the material, the reflectivity only reaches 1 at complete grazing incidence (90°). There is no substantial difference between TE and TM polarization.

incidence angle” of 83.3° . By comparison with the mirror plot in Figure 4.17, we might expect that as the incidence angle becomes more and more grazing, the efficiency should increase continuously...and that is certainly the case for the $n = 0$ order. However, this turns out to be not true for the remaining orders; *there is actually an optimal incidence angle below 90° where efficiency is maximized*. At first glance, it might seem like this is an accidental side-effect of the blazed optimization; since the optimal blaze angle depends on the incidence angle, it might have been possible that all the gratings in Figure 4.18 had their geometry optimized for a sub- 90° incidence angle. However, by exploring the effect of incidence angle on efficiency over a range of blaze angles, Figure 4.19 dispels this idea; it shows that for $n \neq 0$ orders, there is indeed an optimal incidence angle, which depends only on the groove density and the energy.

Figure 4.19 contains a take-away message for instrument designers: if an arbitrary incidence angle is required for some external reason, the blaze angle can be adjusted to optimize for that incidence. However, in the absence of constraints, there does exist a unique optimal incidence angle (and corresponding blaze angle), typically between 87° and 88° , where the efficiency reaches an absolute maximum.

TODO: test with groove density. Does it depend on diffraction eqn?

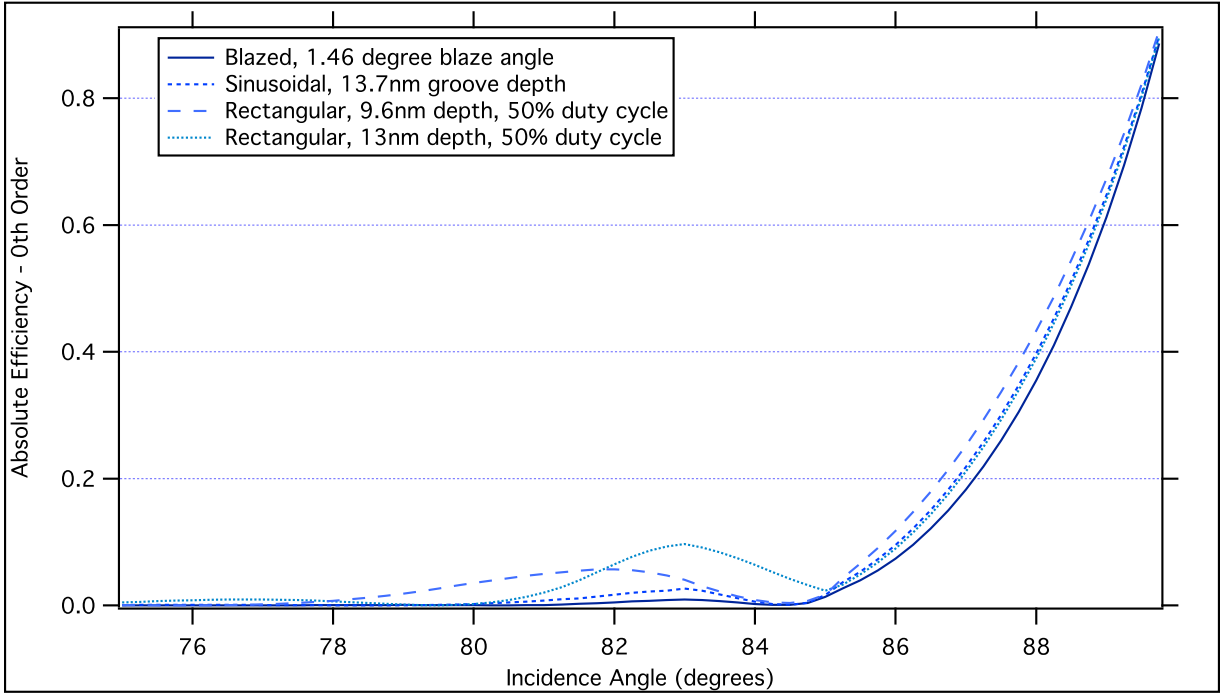
4.3.7 TODO Applications to beamline and instrument design

- Observation: blaze angle and groove depth can be used to optimize efficiency for a constrained incidence angle. However, while 0-order reflectivity increases with grazing incidence, there IS an optimal incidence angle (usually between 87 and 88 degrees), which does not depend on the grating material, and depends somewhat on the incident energy (increases with energy).

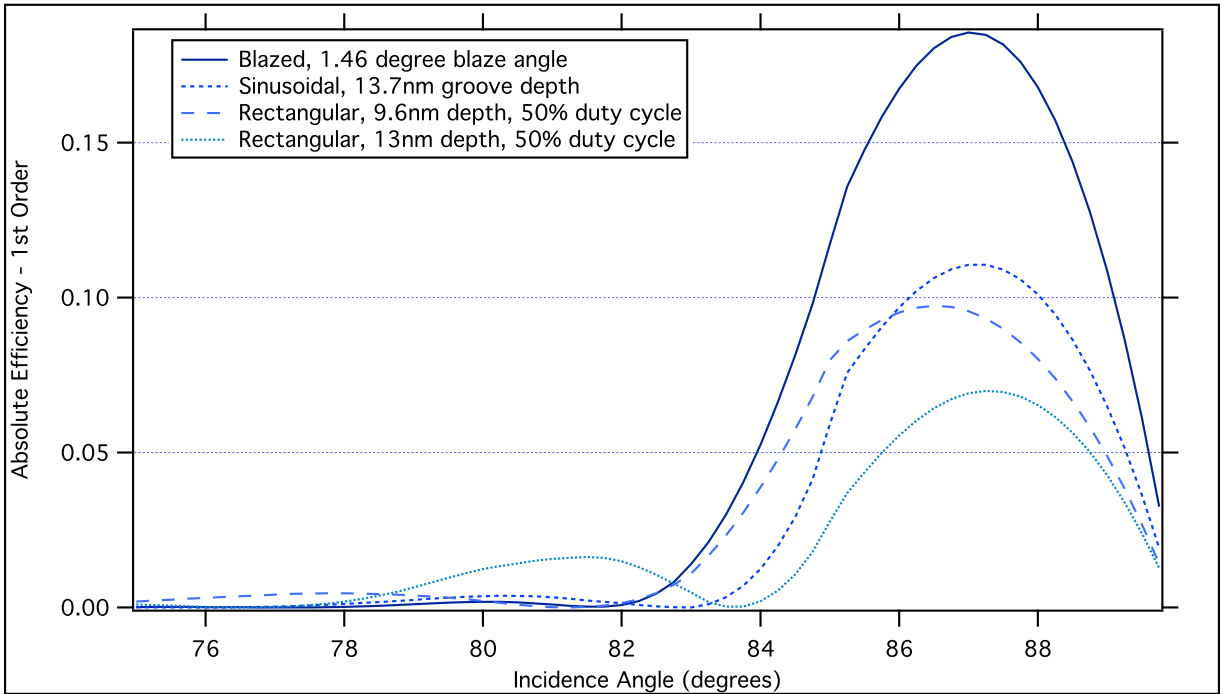
Practical application: This optimal incidence angle provided the starting point for the incidence angles used in the REIXS spectrometer, and explains why the lower-energy gratings (LEG, IMP) use lower (more normal) incidence angles than the high-energy gratings. TODO if time: determine way to calculate optimal incidence angle. Is this just a TE or TM effect? NO... te and tm behave the same.

Highlighted conclusions: - blazed is idea for narrow energy range and constant incidence angle. In case of spectrometer, definitely the right choice. For mono... No constant incidence angle. Still better than sinusoidal if not? Find out.

- Optimal incidence angle
- always blazed: (show whether better than sinusoidal for CIA monochromator)
- consider 3rd order rather than increasing groove density (manuf. limit) –j, next chapter.
- blazed gratings: when optimizing for low energies (near 100 eV): create narrow efficiency peaks. when optimized for higher energies, the peaks are wider and the gratings can be more general.



(a) 0th Order



(b) 1st Order

Figure 4.18: The effect of incidence angle on diffraction efficiency for various grating profiles. While the 0th order efficiency/reflectivity always increases as the incident light becomes more grazing, there is an optimal incidence angle below 90° for higher-order light. The critical angle for total external reflection in Platinum is 83.3° ; clearly both the 0th-order and 1st-order efficiency drop off significantly below this angle. (Gratings: 1200 lines/mm, platinum coating, 400 eV; blaze angles and profiles as indicated.)

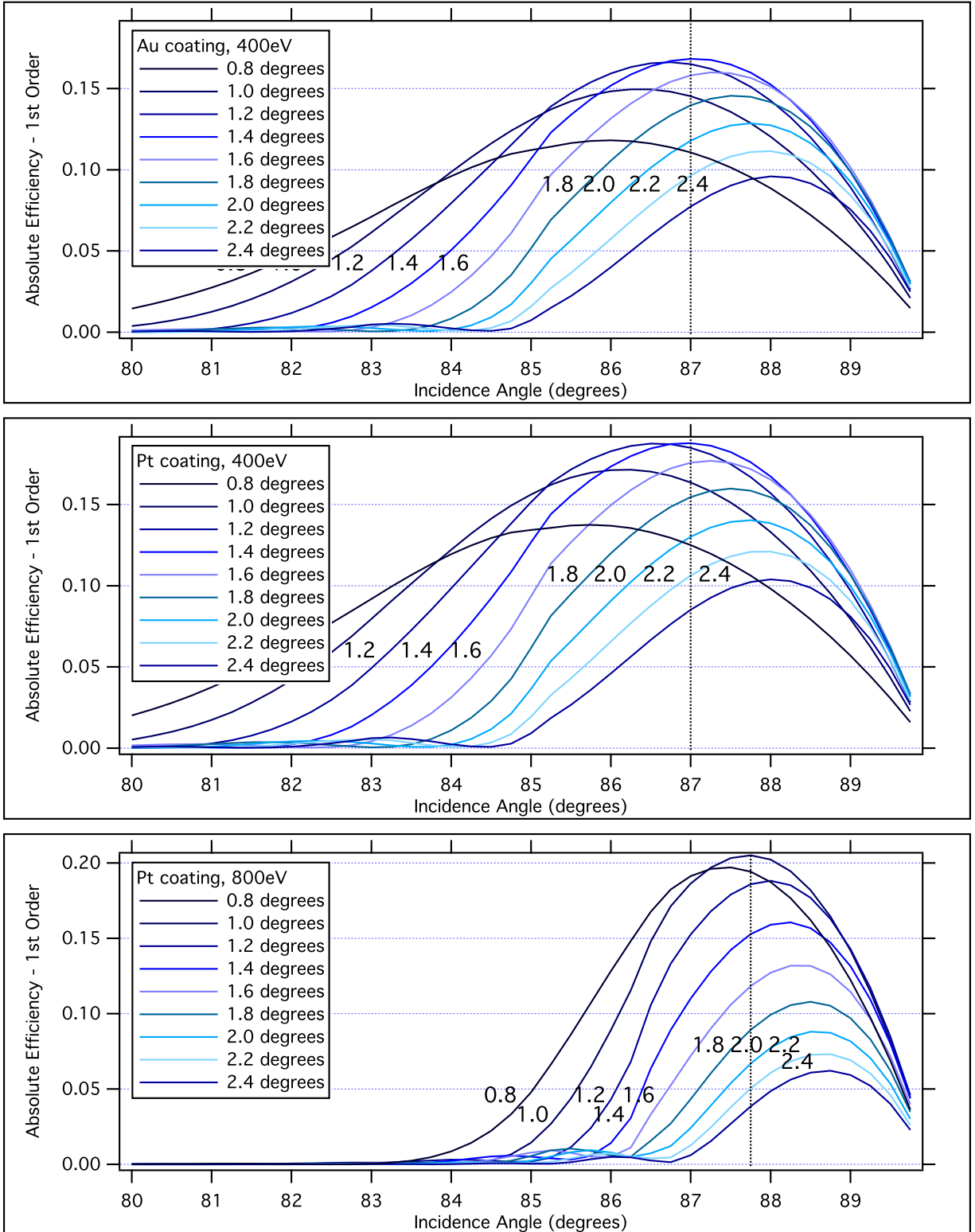


Figure 4.19: While the blaze angle can always be used to tune a grating for a required incidence angle, there is still a particular *optimal* incidence angle that – when combined with a corresponding optimized blaze angle – would produce the highest achievable efficiency. This optimal angle doesn't seem to depend on the material, but only on the groove density and energy. (Gratings: all 1200 lines/mm; coatings, blaze angles, and energies as indicated.)

4.4 Validation: comparison of theory to experimental results

Based on this theoretical survey of the factors affecting grating efficiency, we have provided some recommendations to beamline designers. For these results to be trustworthy, we need to confirm that the theoretical methods in Chapter 3 – and the software implementation described in this chapter – accurately describe gratings in the real world. (We go onward in Chapter 5 to use these tools to design the gratings and optical layout for the REIXS beamline spectrometer; before starting that project, we clearly needed our own validation of the software’s accuracy.)

The published literature on soft x-ray gratings does not contain many measurements of real-world diffraction efficiency, partly due to the difficulty of completing these measurements, and partly because – on receiving brand new gratings – most beamline builders would rather install them as quickly as possible and start doing their own science, rather than spend time on another beamline characterizing the gratings. This is unfortunate for two reasons. Beamline scientists often do not know the efficiency of their machines, or even whether the gratings they have received are optimal. Additionally, grating theorists do not have a large set of experimental results for validating their calculation methods in the soft x-ray regime.

We were able to find one study by M. Bowler at the SRS light source (TODO REF Bowler) with a recent set of efficiency measurements done on four gratings, representing three different types of grating profiles, which turned out to be ideal for comparing with theoretical calculations. The gratings consisted of one blazed grating with 1440 lines/mm, one laminar grating with 600 lines/mm, and two attempted-laminar gratings that ended up with trapezoidal sides of approximately 57° . All of the gratings were well-characterized by the manufacturer after ruling, allowing for accurate geometry inputs into the theoretical calculations. (The study also conducted efficiency calculations using the differential method, but we duplicated these calculations as a double-check on our implementation.)

Figures 4.20 through 4.23 show the experimental measurements from (TODO REF), combined with our own calculations of the grating efficiency. Table 4.2 provides the geometry parameters, derived from the manufacturer’s measurements.

Table 4.2: Geometry parameters and incidence configuration for the gratings in Figures 4.20 to 4.23. The geometry measurements were taken at the center of the grating; accurate characterization of these gratings after ruling made them ideal for comparing with theoretical calculations. CIA stands for “constant included angle” – a mounting configuration which maintains a constant angle between the incident direction and 1st order.

Profile	Density (lines/mm)	Geometry Parameters	CIA ($^\circ$)
Blazed	1440	Blaze angle: 2.2° , anti-blaze: 12.8°	160
Rectangular	600	Depth: 22.2 nm, valley width: 1.12 μm	167
Trapezoidal	300	Depth: 49.3 nm, valley width: 2.46 μm , side angle: 57°	167
Trapezoidal	390	Depth: 54.0 nm, valley width: 1.39 μm , side angle: 57°	160

Note on incidence angle

Unlike the constant incidence angle efficiency curves we have been using up to this point, these gratings were designed for use in constant-included-angle monochromators, where the deviation angle ($\theta_2 + \theta_{2,n}$) between the incident beam and the useful order n is held constant. Therefore, these plots show the efficiency as a function of energy, with an incidence angle that also varies according to this constraint as a function of energy along the x -axis.

Comparison to theory

Of particular interest are the 1st and 2nd order results for the blazed grating in Figure 4.20, since we settled on blazed gratings for the design in Chapter 5. The agreement in the shape and amplitude of the efficiency spectra is very good; we can expect that the real-world efficiency would be slightly lower than predicted due to surface roughness and other effects described in Section 6.3. The agreement for the laminar profile in Figure 4.21 is also very good. Figures 4.22 and 4.23 show a tendency for the calculated results on the trapezoidal gratings to be shifted toward lower energies with respect to the measurements, although the shift is less than 20 eV. Overall, the close agreement between the theoretical and measured efficiencies shown here gives us a high degree of confidence in applying the grating software to optimize real-world beamlines.

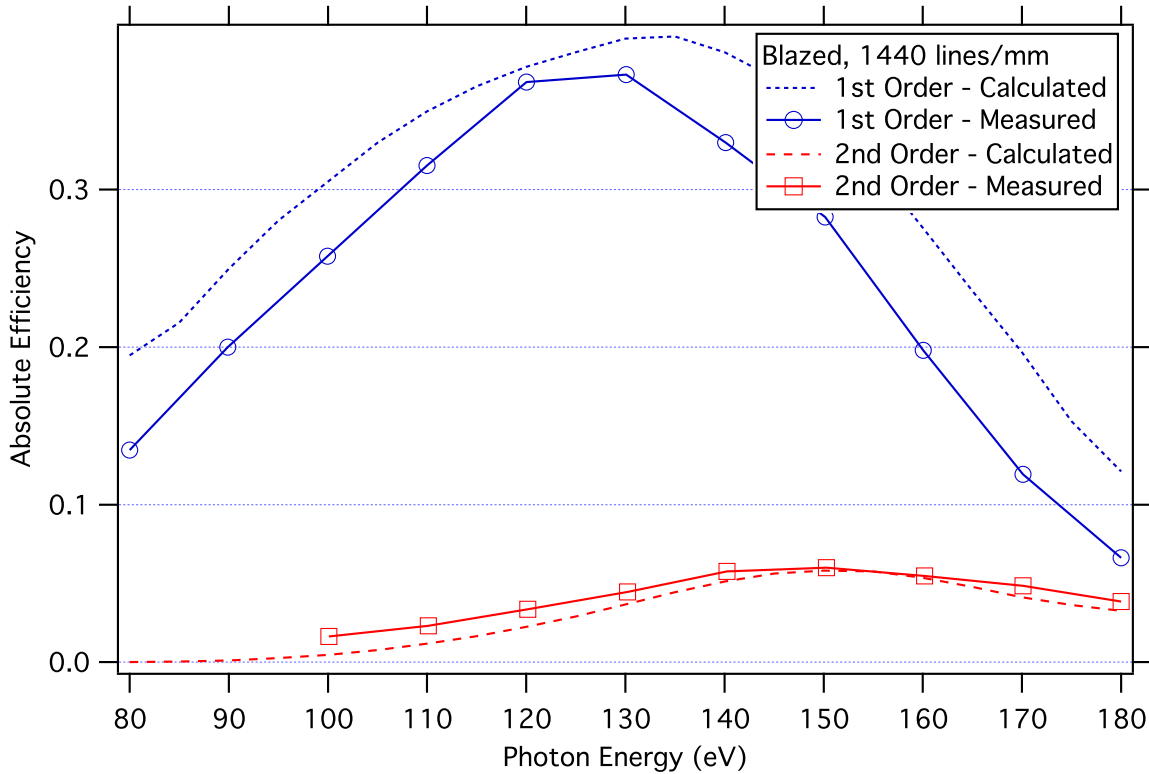


Figure 4.20: Comparison of grating efficiency calculations to diffractometer measurements. Blazed grating, 1440 lines/mm, 2.2° blaze angle, 12.8° anti-blaze angle. Incidence: 160° constant included angle to the 1st inside order.

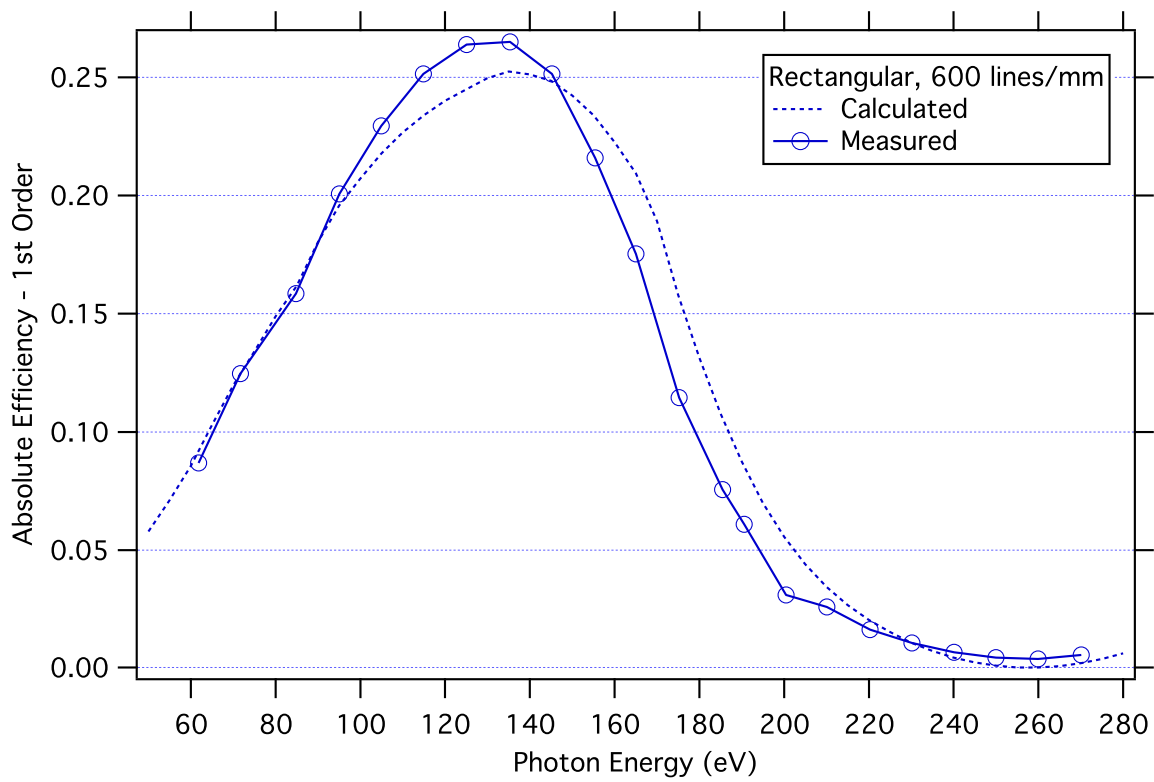


Figure 4.21: Comparison of grating efficiency calculations to diffractometer measurements. Rectangular grating, 600 lines/mm, 22.2 nm depth, 1.12 μm valley width. Incidence: 167° constant included angle to the 1st inside order.

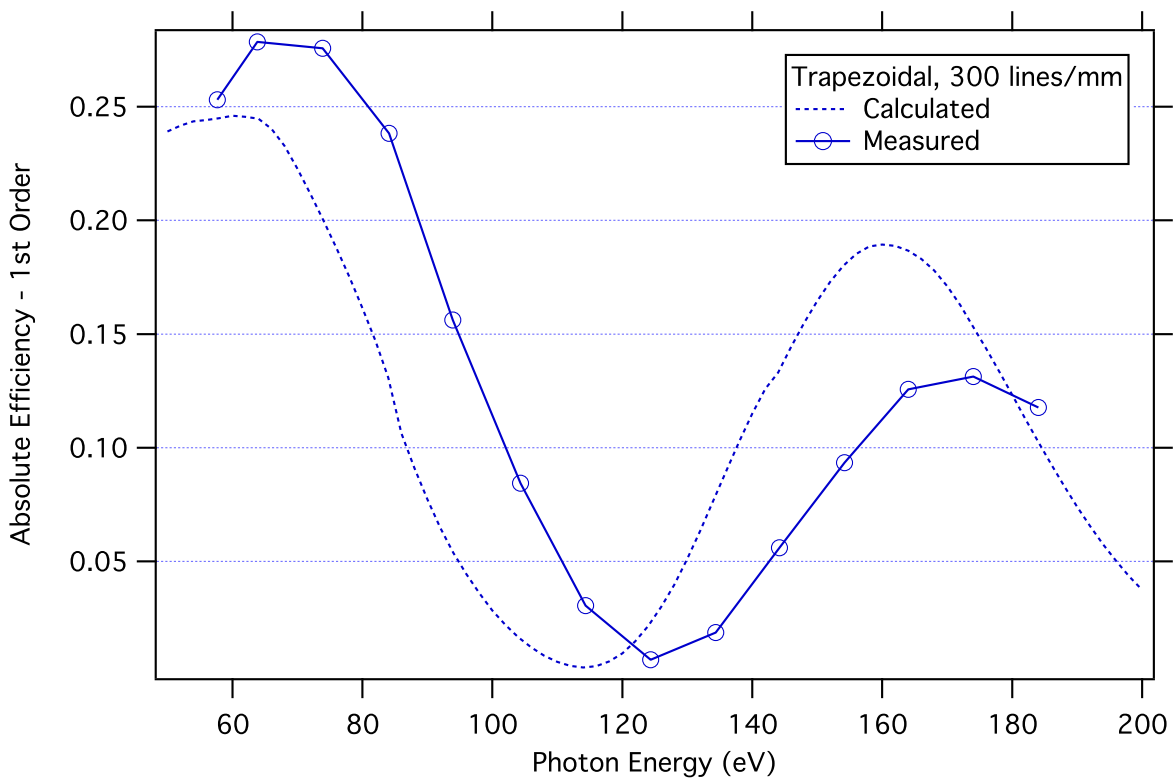


Figure 4.22: Comparison of grating efficiency calculations to diffractometer measurements. Trapezoidal grating, 300 lines/mm, 57° side angles, 49.3 nm depth, 2.46 μm valley width. Incidence: 167° constant included angle to the 1st inside order.

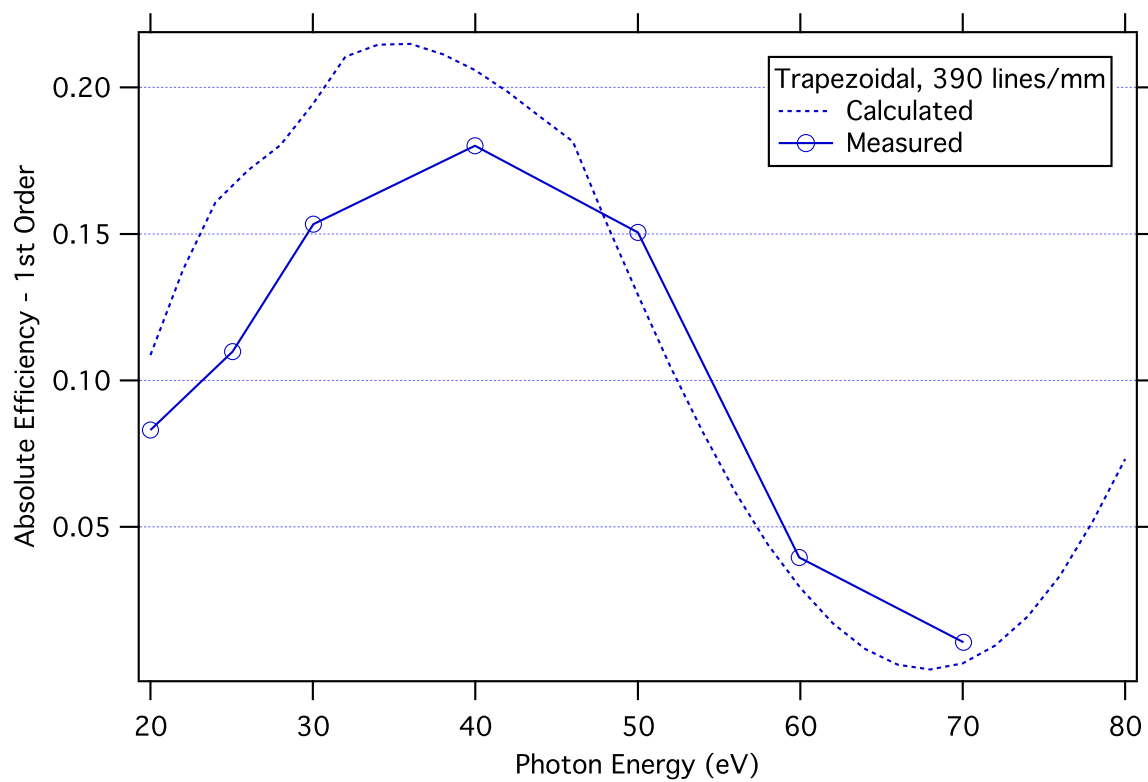


Figure 4.23: Comparison of grating efficiency calculations to diffractometer measurements. Trapezoidal grating, 390 lines/mm, 57° side angles, 54 nm depth, 1.39 μm valley width. Incidence: 160° constant included angle to the 1st inside order.

CHAPTER 5

DESIGN: HOW DAVID AND I APPLIED THESE TOOLS TO MAKE THE REIXS SPECTROMETER OPTICAL DESIGN

5.1 Application to spectrometer design

Up to this point, we have covered the theoretical formulation of grating efficiency, introduced a software tool for efficient calculations, and used this tool to understand how various parameters and conditions affect a grating's performance. We have also validated the calculation results by comparing with efficiency measurements on a set of real-world gratings.

In this chapter, we describe how we applied these results to the design of the soft x-ray emission spectrometer for the REIXS beamline at the Canadian Light Source.

5.1.1 Design goals

The REIXS beamline at the CLS is intended to facilitate a high-throughput user science program in the field of material science. Academic users will apply for beamtime on their own projects through a peer-reviewed proposal process, and will be awarded shifts on the beamline based on the comparative scientific merit of their proposal. These shifts will typically range from as short as eight hours, to as long as a week. (A fraction of the total beamtime will be set aside for industrial clients, who purchase beamtime or analytical services from the facility.)

From the point of view of the beamline designers, the intention of supporting a general user program led to some high-level goals. We wanted to ensure that the spectrometer would have “general-purpose” characteristics, making it applicable for a wide variety of emission experiments. Efficiency was extremely important, in order to minimize the time required for individual scans, maximize the total user throughput of the beamline, and make the spectrometer useful for dilute samples. At the same time, we wanted to push the resolving power of the machine to be competitive with the highest-resolution spectrometers currently in existence. (If we could somehow exceed world-record resolution without sacrificing these other goals, there could even be a possibility of making new discoveries that would be invisible on current machines.)

The design goals were also influenced by the current focus of the material science research group in the Physics Department at the University of Saskatchewan, with interests in organic biomaterials (DNA and

peptides), organic semiconductor and photonic materials, and transition metal oxides.

The performance of the spectrometer was to be derived from the following key strengths:(TODO ref David's thesis)

1. Superior optimization of the design to specific spectral windows of interest, for analysis of materials containing

- silicon (Si L β emission edge, 92 eV),
- carbon (C K α_1 emission edge, 277 eV),
- nitrogen (N K α_1 emission edge, 392 eV) and
- oxygen (O K α_1 emission edge, 525 eV),

while maintaining acceptable performance for

- soft x-ray transitions in transition metals (L α, β and M α, β edges, 600 eV - 1100 eV).
2. A focus on best achievable performance, instead of a compact, mechanically simple or low-budget design.
 3. A mechanical design allowing for superior alignment and calibration.
 4. An optical design based on careful, knowledgeable balancing of the tension between efficiency and resolution.

The final key strength was achieved through extensive teamwork with David Muir, who used ray tracing techniques to quantify and optimize the resolution of our design. His full analysis of spectrometer focussing and resolving power is published in his M.Sc. thesis; some relevant areas of overlap are summarized briefly in this chapter, but for full details we would refer interested readers to (TODO ref).

Together, we set a quantitative goal for both efficiency and resolution: 10% efficiency and 2000 resolving power at all the emission lines of interest. The design constraints were set by the maximum mechanical length of the spectrometer – the physical space available on the beamline floor was limited to 3m at the time – and the endstation budget of approximately \$1 million.

5.1.2 Comparative examples

Before starting work on the REIXS spectrometer, we examined the designs of existing spectrometers at facilities around the world. (Given that we had never designed a soft x-ray spectrometer before, this was a natural starting point, and one that would ensure that – for lack of original ideas – we would design a machine at least as good as any other in existence.)

We analyzed a variety of machines covering a spectrum of design goals, from mechanical compactness and simplicity of grating/detector motion, to maximum resolution. It turned out to be difficult to accurately

compare the stated resolution of the different machines, due to differences in the resolving power criterion and variability in the spatial resolution of their detectors. David resolved this by modelling the optical layout and conducting ray-trace simulations for each one. To decouple the detector performance – which affects the final resolution but is not related to the optical design – from the pure optical performance, we simulated them using a standardized detector with a hypothetical spatial resolution of 20 μm .

Figure 5.1 shows this normalized comparison of spectrometer resolution. For machines offering a choice of gratings, the plot shows the performance attainable by each grating. Among these machines are the SXF spectrometer from Beamline 8.0.1 at the Advanced Light Source (Figure 2.6); another Rowland circle spectrometer, the commercially-available Gammadata XES350 (TODO REF); and several recent variable line spacing (VLS) designs (TODO REF). Unfortunately, we were not able to compare the efficiency for these designs, because the exact grating groove parameters – for existing spectrometers – are rarely known or published.

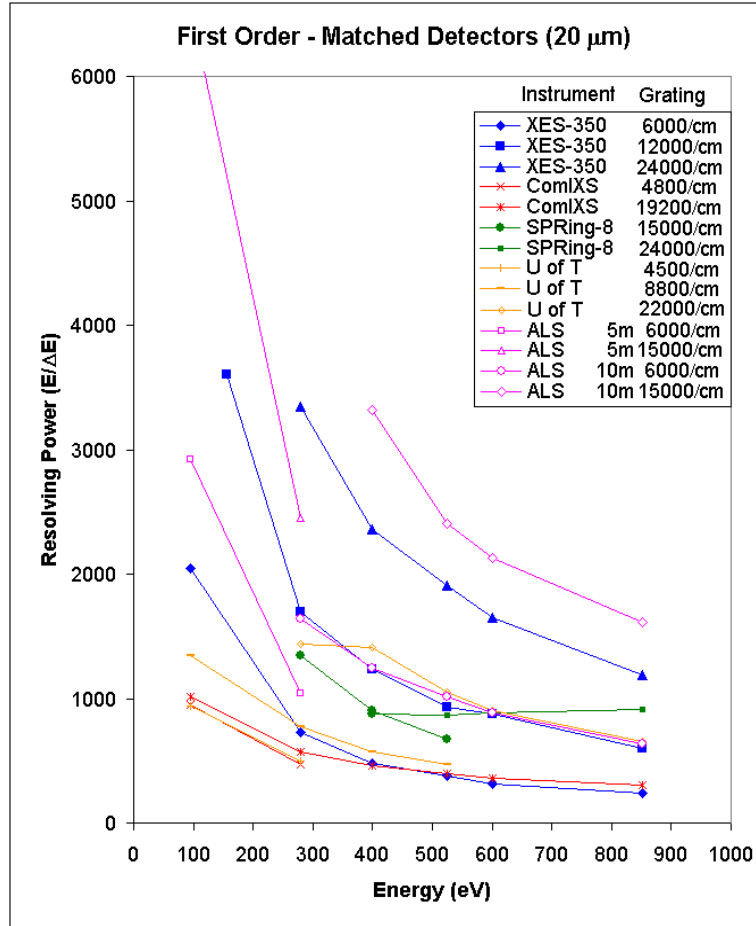


Figure 5.1: Resolving power performance comparison of existing spectrometer designs, calculated with all detectors having a 20 μm pixel size. The legend specifies the spectrometer and grating choice (size and/or line density). Image from (TODO REF: David Muir M.Sc. thesis.)

5.2 Design Process

The first step in the design process was to choose the focussing configuration of the spectrometer. Based on our comparison of existing designs, we selected the Rowland circle configuration for the reasons in Section 5.2.1.

To determine the number of grating choices to offer, we started by assuming one grating optimized for each emission line of interest: Si (92 eV), C (277 eV), N (392 eV), O (525 eV), and the transition metal range (600 - 1100 eV) optimized for Fe (725 eV). Eventually, after completing the subsequent steps in the design process, we found that we could merge the medium energy gratings (277, 392 eV) and high energy gratings (525, 725 eV), since there was considerable overlap in their performance. This allowed us to add a fourth grating, intended to cover a large energy range with extremely high efficiency, for studying dilute samples; we called this one the “impurity” (IMP) grating. Later, we added two more gratings, intended to offer impressively high resolution, in the medium energy (HRMEG) and high energy (HRHEG) range; these 3rd order gratings are described in Section 5.3.

Table 5.1: Gratings chosen for the REIXS spectrometer, with their target energies used for optimization, the energy ranges they will be able to cover, and the final optimized grating parameters

Grating	Optimization Energy (eV)	Energy Range (eV)	Groove Density (lines/mm)	Incidence Angle (°)	Coating	Blaze Angle (°)
1st order						
Low Energy (LEG)	92 eV (Si)	30 - 300	600	86	Au	1.85
Impurity (IMP)	400 eV (N)	75 - 750	900	87	Ni	1.11
Medium Energy (MEG)	400 eV (N)	250+	1200	88	Ni	1.48
High Energy (HEG)	725 eV (Fe)	400+	2000	88	Pt	1.52
3rd order						
High Res Medium Energy (HRMEG)	280 eV (C)	280+	1800	88	Ni	4.85
High Res High Energy (HRHEG)	725 eV (Fe)	525+	2600	88.25	Pt	4.05

The next step was to determine the grating parameters (line density, profile) and the optical geometry (incidence angle, distances, grating radii, etc.), subject to the focussing constraints, to reach our target resolution and efficiency. Table ?? describes all of the overlapping parameters in a Rowland circle spectrometer that affect resolution, geometric efficiency, and/or grating efficiency; almost universally, increases in one goal result in decreases in the others.

Because of the inherent tension between resolution and efficiency, attempts to establish the parameters for the gratings prompted a carefully-choreographed, swashbuckling duel between the Forces For Efficiency and the United Resolutionary Front. This battle became an iterative process, inherently involving a degree of trial-and-error and continuous refinement. In retrospect, the design process we would recommend for future designs is summarized in Figure 5.2. The final grating parameters that effect efficiency are shown in Table 5.1.

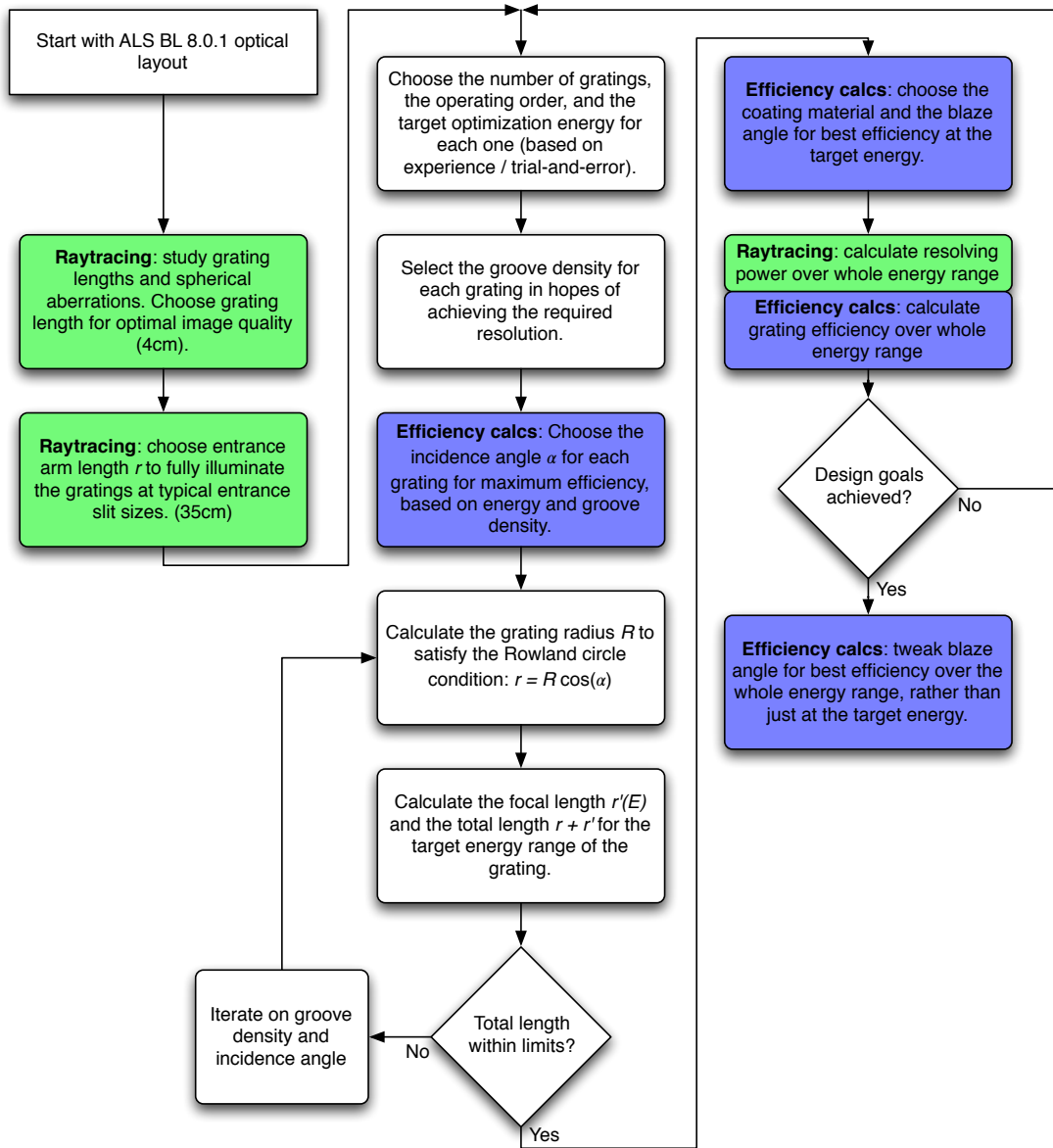


Figure 5.2: Approximation of the process used to design the optics of the REIXS spectrometer.

5.2.1 Justification of design choices

Rowland circle vs. VLS design

We mentioned in Chapter 2 that spectrometer optics must focus as well as disperse light. Some of the designs we surveyed achieved this using VLS gratings, while others employed spherical gratings in the “Rowland circle” configuration. Fortunately, this provided us with a good basis for comparison.

According to (TODO REF david’s thesis), the main advantage of VLS gratings is to control the shape of the focal curve – the path in space that the detector must travel along to keep the spectrometer focussed as a function of energy. A flat focal curve simplifies the mechanical design, since the detector then only needs to move along one axis. As Figure 5.3 shows, the VLS correction also shortens the focal curve, so that to handle the same energy range, a spectrometer can be made more compact. Unfortunately, a compact focal curve places the detector closer to the grating and inherently reduces the resolution – as a result, all of the VLS designs we surveyed required very high spatial resolution detectors to maintain just average resolution (TODO REF Table 3.3). TODO review current leading spectrometers at ESRF, SLS... VLS with very long arms.

The VLS technique can also be used to minimize aberrations (astigmatism, coma, etc.), but these can only be fully corrected at a single energy; for a general-purpose spectrometer, this is not helpful.¹ Using VLS corrections also removes the flexibility to operate the spectrometer in higher orders: since the formulas for the correction terms depend on the diffraction order, VLS spectrometers behave erratically outside of their design order.

Figure 5.4 compares the detector image of three adjacent energy lines, for a comparable VLS and Rowland circle spectrometer. While requiring a longer focal curve and more complicated detector motion, the Rowland design offers far higher resolution for the same nominal groove density; it would take a large increase in efficiency-robbing line density for the VLS design to keep up with it. Therefore, since we were not constrained by physical size², we selected a Rowland circle optical layout – similar to the ALS Beamline 8.0.1 SXF spectrometer, as the basis for our design.

Choice of profile: blazed vs. rectangular / sinusoidal

Back in Chapter 2, we saw that optimally blazed gratings have almost double the efficiency of sinusoidal gratings, and even more than that of rectangular gratings (Figure 4.11). Since the ideal blaze angle is energy-dependent, we saw that this optimization comes at the cost of having an efficiency peak centred on the target energy, and comparably lower efficiency outside the peak. However, for high groove densities and high optimization energies, the peaks are wide enough to span the entire soft x-ray range. For low groove

¹After completing our Rowland circle design, an external consultant attempted to optimize it by adding VLS terms to correct aberrations. While this worked well at the optimization point of 200 eV, the detector image became heavily defocussed just 50 eV away (TODO REF, Figure 5.1).

²At least, we were not constrained beyond the 3 meter limit of the beamline space

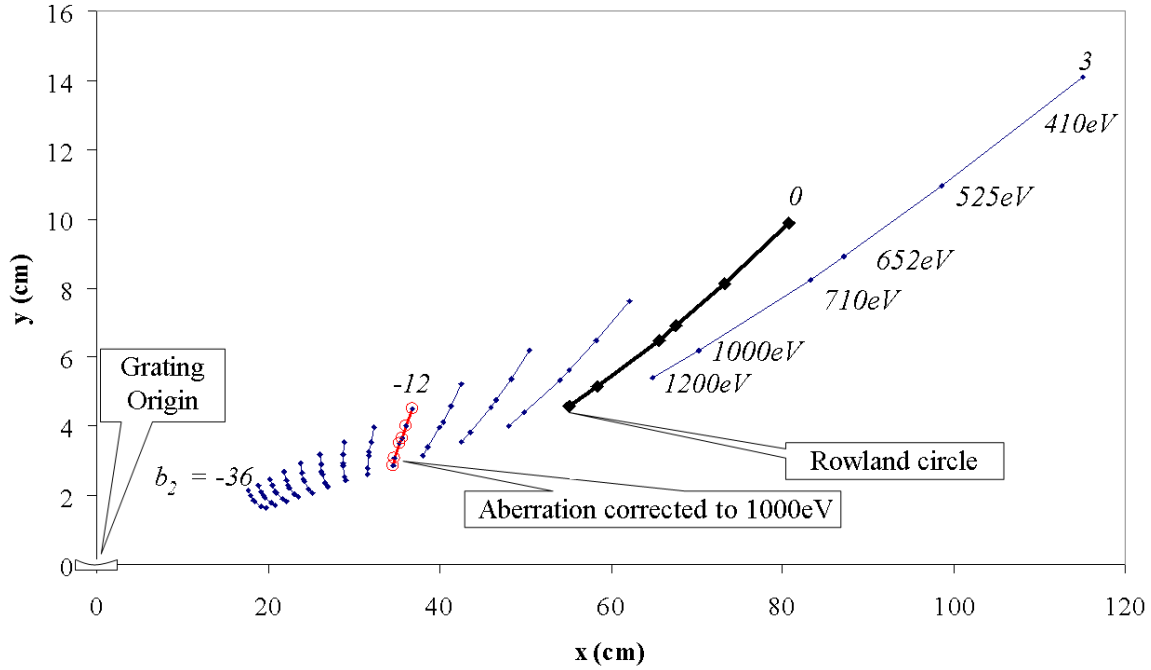


Figure 5.3: The focal curve is the path in space the detector needs to move along to maintain focussing as a function of energy. This plot shows the effect of the b_2 VLS correction term: with a b_2 of 0, the focal curve is the same as the Rowland circle focal curve. A specific b_2 value of -12 (highlighted in red) straightens the focal curve, which could simplify the detector mechanics, but also shortens the focal distance and reduces the resolution at the detector. Image from (TODO REF Figure 2.17)

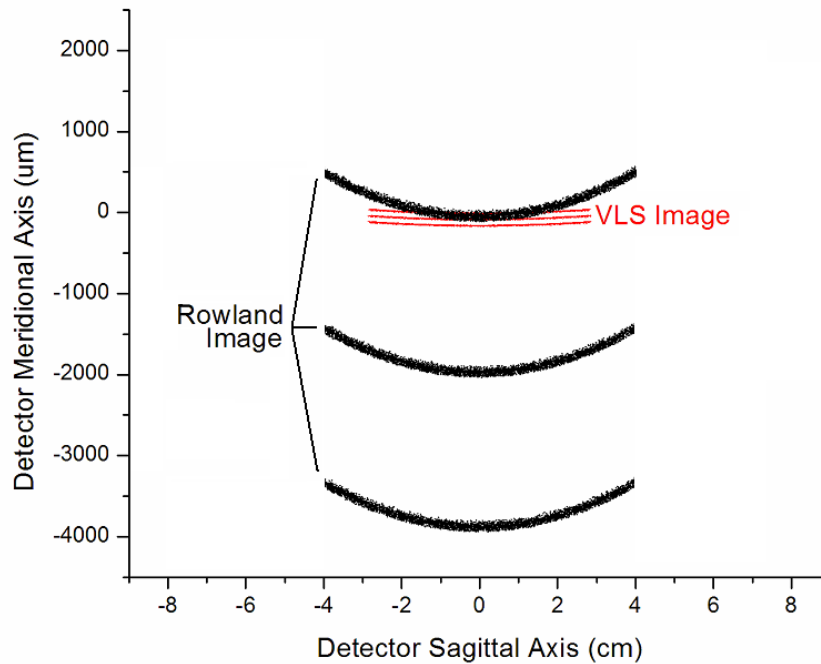


Figure 5.4: Variable line space (VLS) corrections reduce aberrations that cause curvature, as seen in these ray-traced detector images of three adjacent emission lines. However, the increase in resolution due to better focussing is not able to make up for reduced dispersion across the surface of the detector, as compared to the Rowland circle alternative. Image from (TODO REF Figure 2.18)

densities and low optimization energies – as would be the situation for the LEG – the peak bandwidth is smaller, but still easily covers the design energy range of this grating.

For each grating, we selected blaze angles corresponding to the target energies in Table 5.1, according to Equation 4.8. We then used the efficiency software to further optimize the blaze angle at this energy, using the analytical θ_b as a starting point. We then calculated the efficiency curves for these profiles, as well as for optimized sinusoidal and rectangular alternatives, and confirmed that the blazed profile was indeed the clear winner for all the gratings. (For some of the gratings, we tweaked the blaze angle at the end of the design process, since we were willing to accept a small reduction in efficiency at the target energy, in exchange for higher overall efficiency integrated across the whole energy range.)

Ruled vs holographic gratings

Section 4.3.1 gave an overview of mechanical ruling and holographic grating manufacturing techniques. To make a pragmatic decision between these two options, we needed to consider the impacts of real-world manufacturing issues. Common errors which happen during ruling and holographic manufacturing are shown in Figure 5.5.

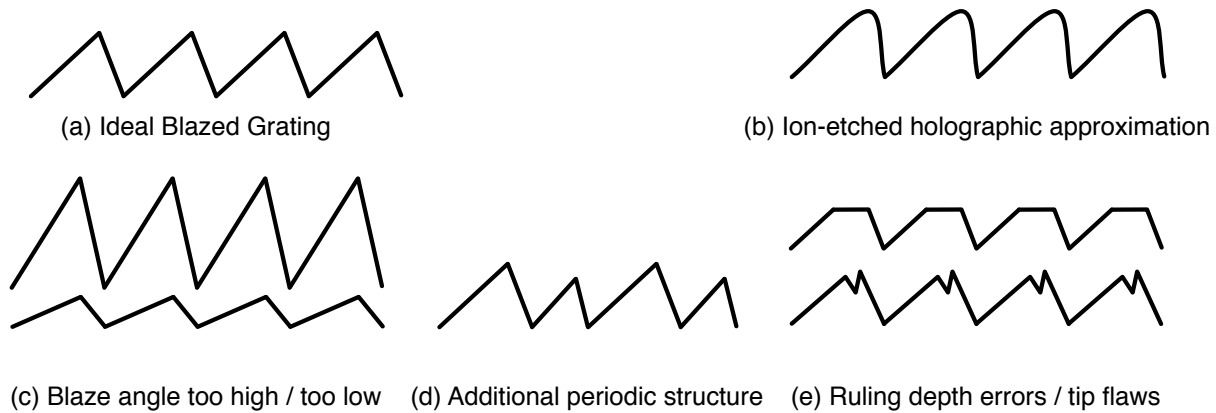


Figure 5.5: Common errors in the manufacture of ruled and holographic gratings. Holographic exposure creates a sinusoidal profile; subsequent ion-etching (b) can only approximate a triangular profile. Ruled gratings can suffer from blaze angle errors (c), or errors due to the shape and/or depth of the diamond tip (e). If the ruling engine introduces periodic errors in the groove position, this additional structure (d) superimposes additional diffraction patterns (ghosts).

Mechanical ruling engines are designed to be precision machines, but they must be carefully set up and operated to avoid errors. Achieving the specified blaze angle – critical to efficiency – must be accomplished during setup by aligning the diamond tip, ruling a test section of the grating, analyzing the resultant blaze angle with a microscope, adjusting the tip, and tediously repeating this process. Without sufficient quality control, the blaze angle can end up high or low by a few tenths of a degree, which could completely eliminate the blazing advantage.

Another concern is whether the grooves end up uniform, and the groove geometry is maintained, across

the entire grating. This is essential to both the efficiency and the resolution. If the ruling process creates errors that vary periodically over a series of grooves, this will insert additional periodic structure into the grating and create “ghosts” in the final spectrum: an additional diffraction pattern superimposed over the desired one, with intensity peaks again given by the grating equation, but at a different period. Errors with a period on the same order as the groove spacing create “Lyman ghosts”, which end up far from the spectral lines. Errors with periodicities on the order of millimetres create “Rowland ghosts”, which appear close to and symmetric around the desired spectral lines.

One additional flaw that can occur with ruled gratings happens when the diamond tip fails to penetrate far enough into the metal surface to create the desired profile, resulting in something that looks like Figure 5.5 (e). The profile can also be corrupted by irregularities in the diamond tip, or by bits that break off or are picked up during the ruling process. (One common manufacturing error is for the tip to pick up a shard of metal, and carry it with it for several thousand trips across the grating; this creates an inefficient stripe across an otherwise acceptable grating.) Finally, for maximum efficiency, the anti-blaze angle should be as close to 90° as possible, but in most cases the shape of the ruling tip forces it to be below 30° . (The blazed grating in Figure 4.20 had an anti-blaze angle of 12.8° .) According to the theoretical calculations in Figure ??, the anti-blaze angle does not start to seriously affect the efficiency until it goes below ~ 4 times the blaze angle, ie: 5° for a blaze angle of 1.5° .

Holographic gratings overcome many of these disadvantages. They are not susceptible to ghosting, since their grooves are all formed simultaneously, with a period as regular as the wavelengths of an electromagnetic wave.³ They can also be ruled faster and more inexpensively – mechanical ruling can take weeks for one grating – so that flaws can be corrected by trial-and-error. Despite these advantages, holographic gratings have their own manufacturing challenges. In some cases, variation in the sinusoidal groove depth happens because the intensity of the interference pattern changes across the width of the grating. Traditionally, holographic techniques also have not been able to produce groove densities as high as mechanical ruling engines. The most significant drawback to holographic gratings, however, is their inability to create a true blazed profile, even when using ion etching or the Sheridan method (Figure 5.5 (b)). For this reason alone, we chose mechanical ruling for all six of the spectrometer gratings.

In future work, it would be helpful to characterize the typical groove shape of real-world ion-etched holographic gratings, and update the grating efficiency software to support this additional profile; this could allow for more informed decision-making on whether to use or reject holographic ruling.

³However, modern interferometrically-controlled ruling engines can inscribe grooves with such precision that they have also virtually eliminated ghosting.

5.3 High-resolution (3rd order) design

5.3.1 Options for reaching extreme resolution

We mentioned in Section 2.2.2 that the two general ways to increase the resolution of a spectrometer design (besides choosing a better detector) are to move the detector further away from the grating, or to increase the angular dispersion of the grating. Increasing the detector distance requires adjustments to the focussing scheme, and severely reduces geometric efficiency.⁴ This option also is not an option when the constraints on the machine size have been reached. The other method – increasing the angular dispersion – can either be achieved using the groove density, or the diffraction order. As we saw in Figure 4.13, higher groove densities reduce the grating efficiency, and are also constrained by manufacturing limits.⁵

So this leaves three related questions for a designer trying to achieve extreme resolution: what do you when you have hit the machine size limit *and* the groove density manufacturing limit? And is taking these parameters all the way to their limits actually the optimal solution for maintaining efficiency at high resolution? What are the consequences of designing intentionally for a higher diffraction order?

All existing soft x-ray spectrometers seem to be designed for 1st order operation, based on the assumption that diffraction efficiencies in higher orders are too low to be useful. (We have seen users force some Rowland circle designs into 2nd order, when trying to temporarily tease out higher resolution.) Although it had never been done before, our survey of efficiency trends hinted that it might actually be more efficient to use gratings in 3rd order, than to triple their groove density or extend the machine size. Based on these results, we attempted to add ultra-high-resolution capabilities to the REIXS spectrometer, by considering gratings specifically optimized for 3rd order operation.

5.3.2 Justification for 3rd order design

A combination of grating efficiency calculations and ray tracing simulations showed that this novel 3rd order design would actually be the *only* way to dramatically increase the resolution of our spectrometer, within the mechanical length constraints that existed at design time. Figure 5.6 shows why the 3rd order design makes sense from an efficiency perspective. From Equation 2.4, we can easily see that switching from 1st order ($n = -1$) to 3rd order ($n = -3$) has the same effect on the angular dispersion (and resolution) as tripling the groove density. The conventional assumption on higher order operation is that even when properly blazed, higher order efficiencies are extremely low compared to the first order. However, we found that at

⁴In a Rowland circle design, ray trace testing (TODO) showed us that the geometric efficiency is proportional to the inverse cube of the detector distance. The reduction in sagittal angle captured by the detector causes the first reduction. The grating radius R needs to be increased to maintain focussing, and with spherical gratings, this further increases the sagittal dispersion. The entrance distance r also needs to be increased, causing a reduction in the solid angle captured by the grating. This could be compensated by increasing the grating size, but the total grating size is constrained by limits on spherical aberration.

⁵While some ruling engines can now reach extremely high groove densities approaching 10 000 lines/mm, the groove quality and accuracy suffers. For soft x-ray gratings, 3 000 lines/mm seems to be a current effective limit for both mechanical and holographic ruling.

certain points along the efficiency curve, the 3rd order grating efficiency would actually be *higher* than for an equivalent-resolution grating with three times the groove density operated in 1st order. Not only that, but in most cases the hypothetical triple-groove density alternative would be moot: it would be impossible to manufacture such a grating.⁶

Figure 5.6 is based on the efficiency curves for the two 3rd order gratings we ended up adding to the design. For the 1800 line/mm HRMEG grating (a), designed for outstanding resolution near the carbon emission line (280 eV), the efficiency in 3rd order is actually higher than for an equivalent-resolution 5400 line/mm grating optimized for 1st order. (Even with this advantage, we point out again that it would be impossible or very difficult to rule a 5400 line/mm grating with sufficient quality to achieve this theoretical efficiency.) One interesting thing to note is that this advantage in 3rd order efficiency persists even for appropriately-optimized sinusoidal gratings, shown in red.

For the 2600 line/mm HRHEG grating (b), the 3rd order efficiency is comparable, but not quite higher, than its hypothetical equivalent 7800 line/mm 1st order grating. In this case, however, the 3rd order design is really the only possibility; it would be practically impossible to manufacture the 7800 line/mm grating.

5.4 TODO Coating choices:

- DATA 4f: plot reflectivities over range for: Au, C, Ni, Pt, Ir, Ag, etc [use DATA 3g]
- Choices within regions of interest

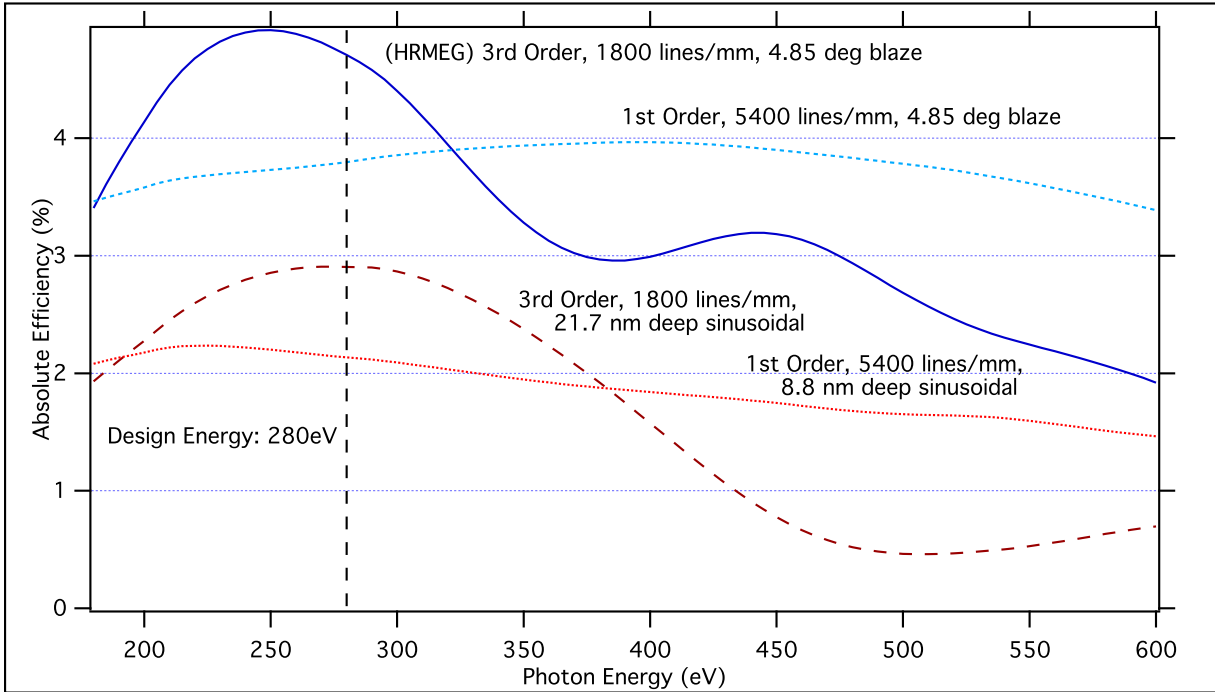
5.5 TODO: Optimization and Tolerancing

- simple hill-climbing [with constraints]
- tolerance limits based on 15% relative drop; c

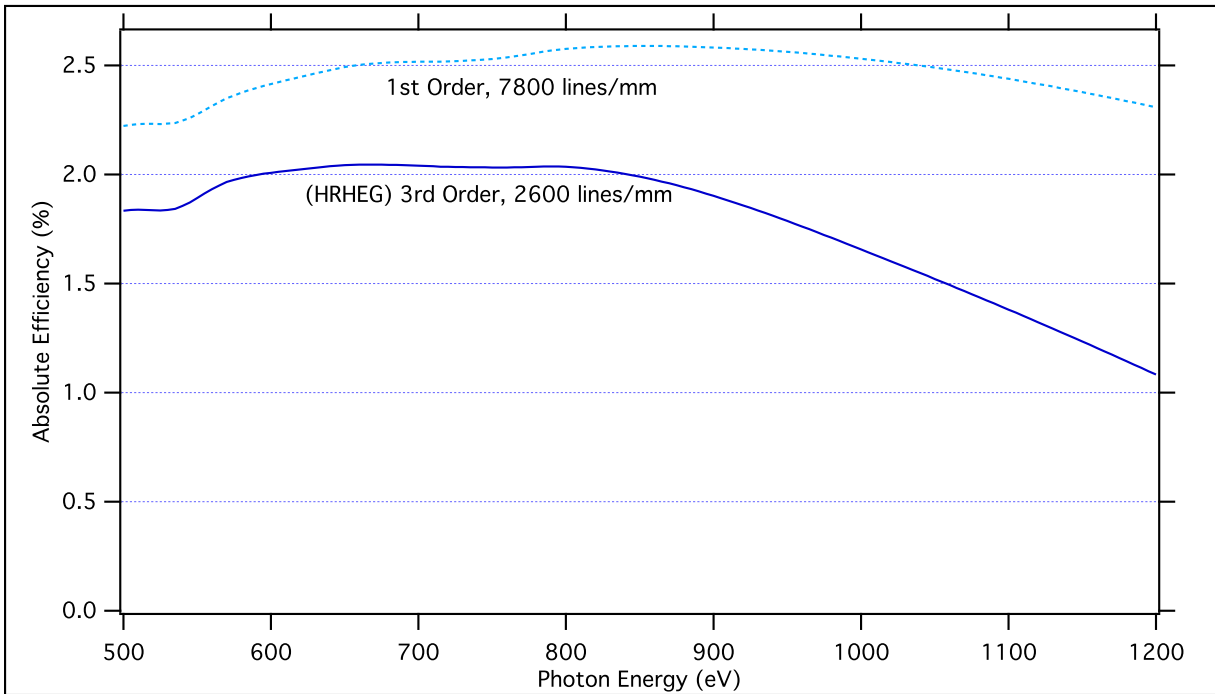
5.6 Summary of Final Design

By combining efficiency and resolution calculations to carefully manage the trade-off between these two goals, we were able to exceed our design targets of 10% efficiency and 2000 resolving power at all the emission lines of interest, using the LEG, MEG, and HEG gratings. The addition of the impurity (IMP) grating added extremely high efficiency over a large portion of the soft x-ray energy range, and the two 3rd order gratings added massive resolving powers of 14 000 and 10 000 at the carbon and iron lines. (Although their efficiency is substantially lower than the other gratings, the novel usage of the 3rd order was the only way to achieve this kind of resolution within our physical size constraints.)

⁶Even if it was possible to rule such an ultra-high density grating, decreases in the groove quality would reduce the real-world efficiency through stray light processes described in Section 6.3. In Chapter 6, we characterize our own manufactured gratings and find a general reduction in real-world efficiency with increasing groove density, as the ruling process struggles to keep the grooves clean and properly formed.



(a) The 3rd order HRMEG (1800 lines/mm), and an equivalent-resolution 1st-order grating (5400 lines/mm - difficult or impossible to manufacture). The 3rd order efficiency advantage persists even for sinusoidal gratings without the blazing advantage.



(b) The 3rd order HRHEG (2600 lines/mm), and an equivalent-resolution 1st-order grating (7800 lines/mm - impossible to manufacture).

Figure 5.6: At some points along the efficiency curve, the grating efficiency is actually higher in 3rd order than it would be in 1st order for an equivalent-resolution grating with three times the groove density... assuming you could even manufacture such a grating. HRMEG and alternatives: nickel coating, geometry as indicated. HRHEG and alternative: platinum coating, blaze angle of 4.05° .

Table 5.2 shows the predicted resolving power and grating efficiency of our design for all the edges of interest. For those interested in resolution, Figure 5.7 compares the resolving power of our design to the competitors in Figure 5.1. The final optimized grating parameters are included in Table 5.1. In Figures 5.8 through 5.10, we show the theoretical predicted efficiency in 1st, 2nd, and 3rd order for all six gratings. In Chapter 6, we compare these efficiencies with the real-world diffraction performance of the manufactured gratings.

Table 5.2: Predicted resolving power (RP, $E/\Delta E$) and grating efficiency (Eff) of the REIXS spectrometer at the emission lines of interest. Values are listed for all gratings where the emission energy lies within the detector’s motion range. (Resolving power results are taken from (TODO REF david’s thesis).)

	1st Order Gratings								3rd Order Gratings			
	IMP		LEG		MEG		HEG		HRMEG		HRHEG	
	RP	Eff	RP	Eff	RP	Eff	RP	Eff	RP	Eff	RP	Eff
Si (92 eV)	4693	7.4%	2986	38.7%	10146	5.3%	15580	3.6%				
C (277 eV)	1722	29.1%	1032	3.8%	3646	19.6%	5752	6.7%	14066	4.7%		
N (392 eV)	1226	34.1%			2528	22.8%	4039	9.8%	10227	3.4%	16510	1.5%
Fe (725 eV)	731	23.4%			1588	17.7%	1595	12.2%	6238	0.9%	9468	2.1%

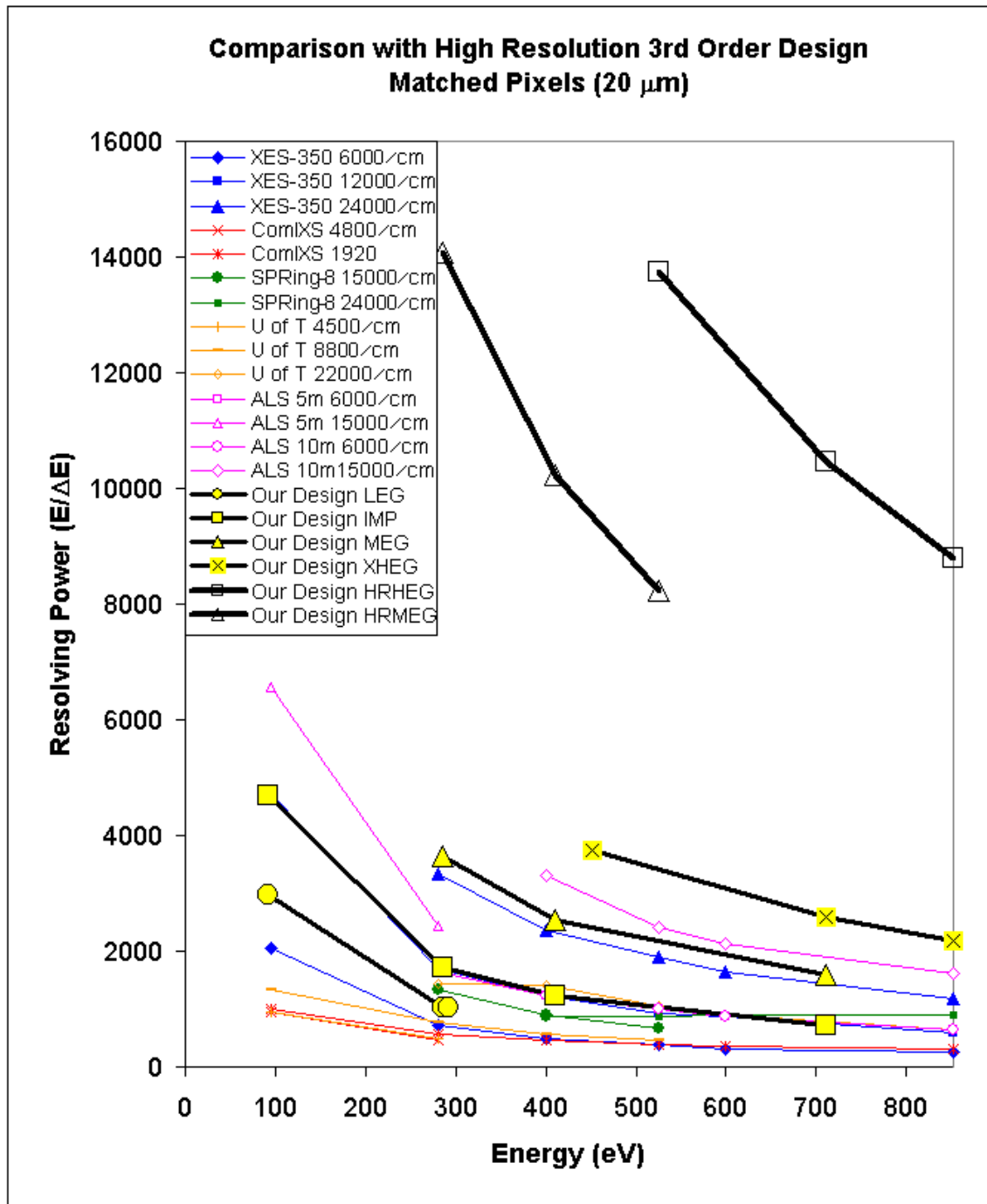
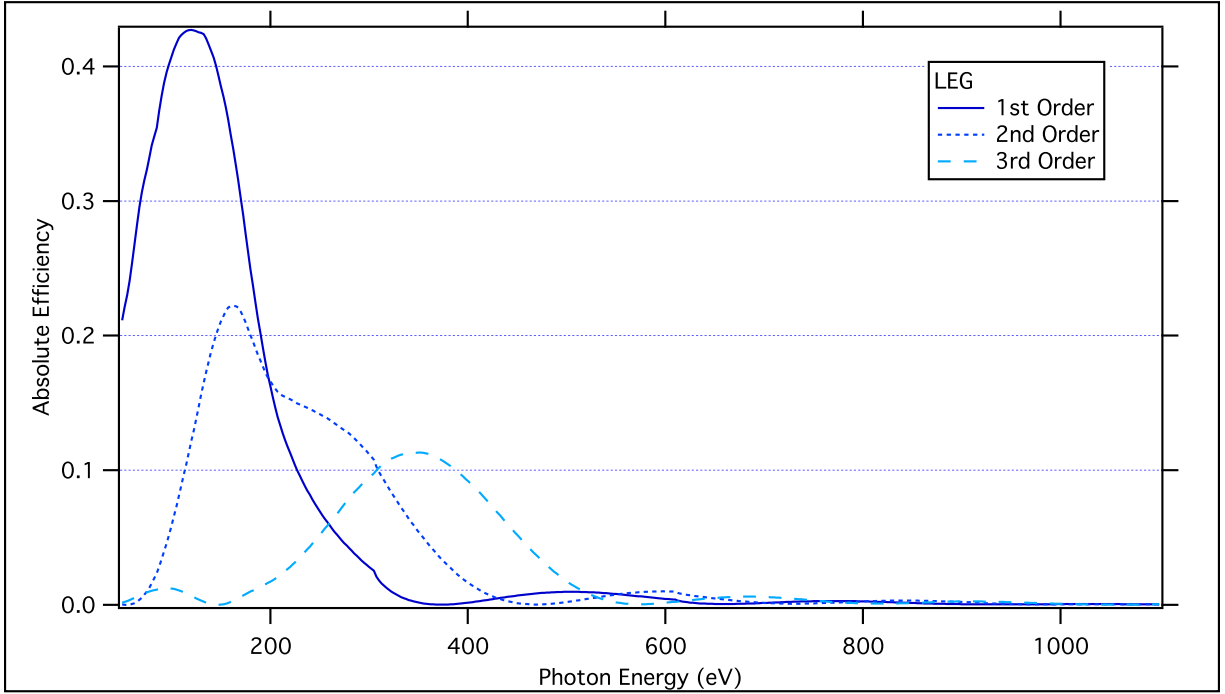
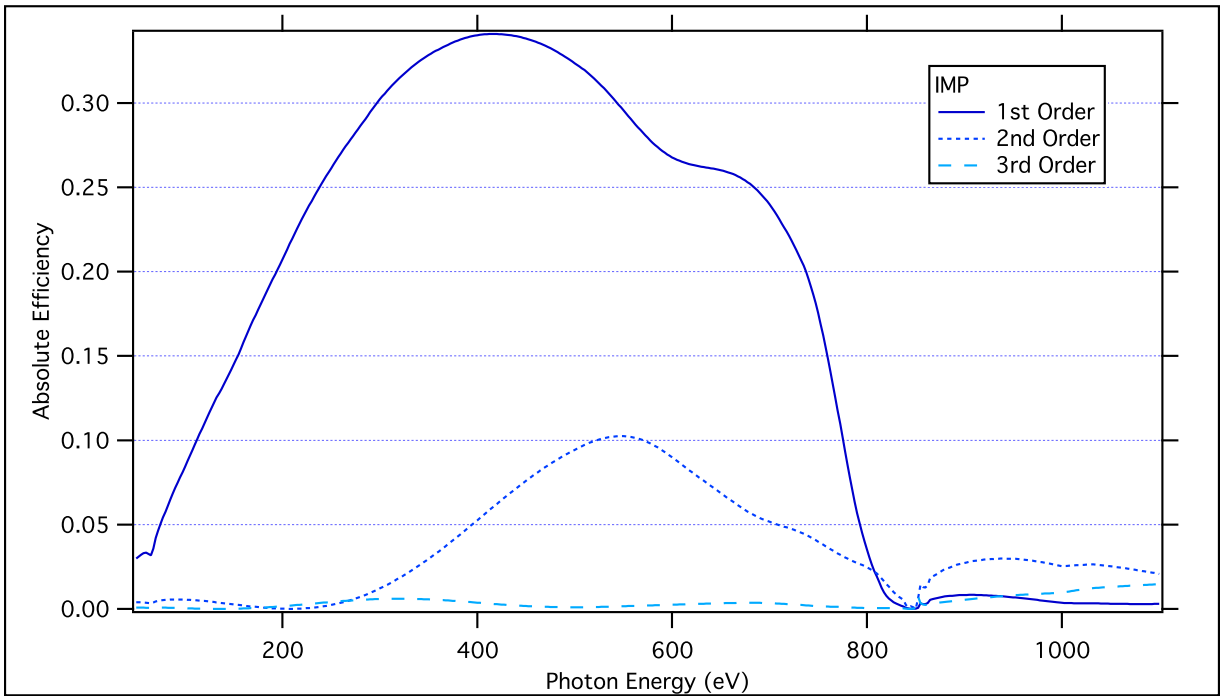


Figure 5.7: The REIXS spectrometer design offers higher predicted resolution than the existing designs we surveyed in Figure 5.1. (The advantage is even more dramatic when considering the 3rd order high resolution gratings.) However, the full strength of the design comes from a knowledgeable balance with grating efficiency, based on our combined calculations. Image from: (TODO REF David's thesis Figure 4.7)

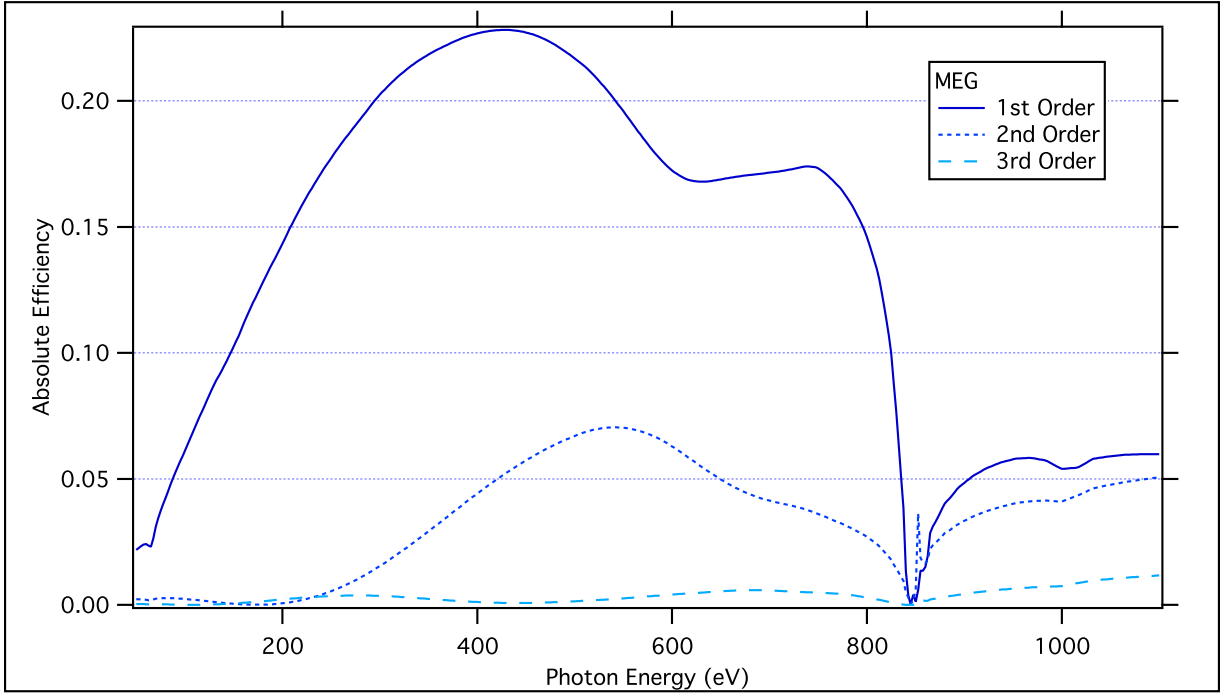


(a) Low Energy Grating (LEG): 600 lines/mm, 1.85 deg. blaze angle, Au coating, for 86 deg. incidence

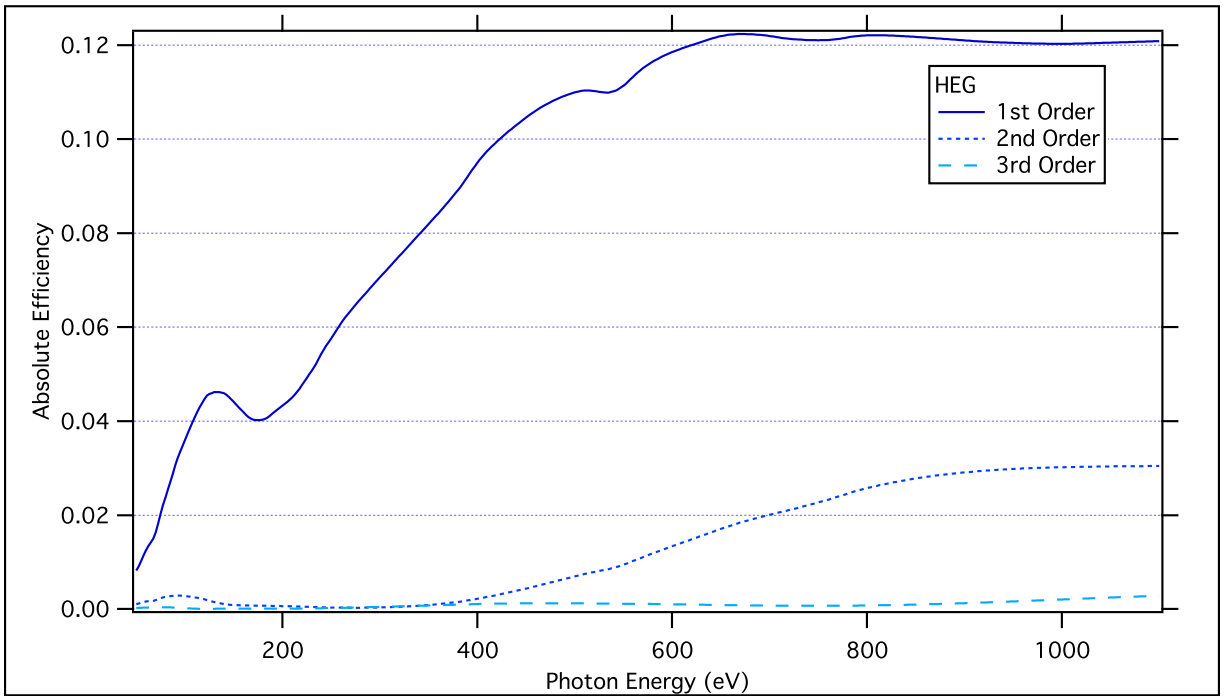


(b) Impurity Grating (IMP): 900 lines/mm, 1.11 deg. blaze angle, Ni coating, for 87 deg. incidence

Figure 5.8: Theoretical diffraction efficiency for the Low Energy Grating and Impurity Grating.

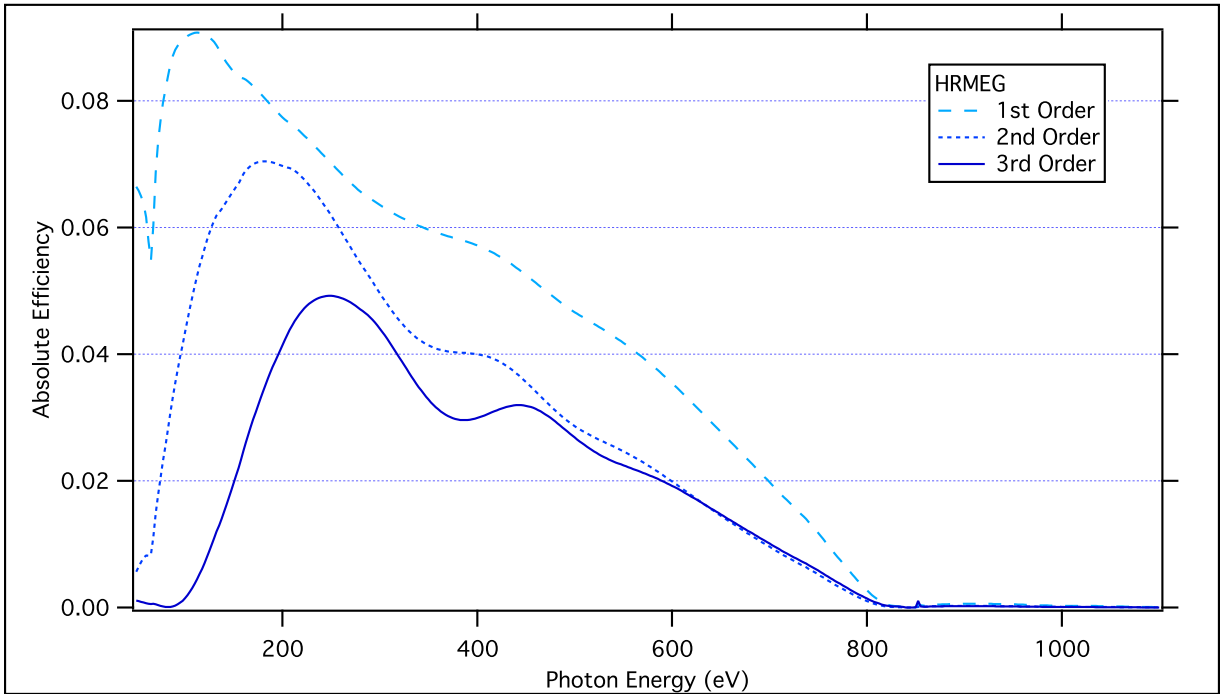


(a) Medium Energy Grating (MEG): 1200 lines/mm, 1.48 deg. blaze angle, Ni coating, for 88 deg. incidence

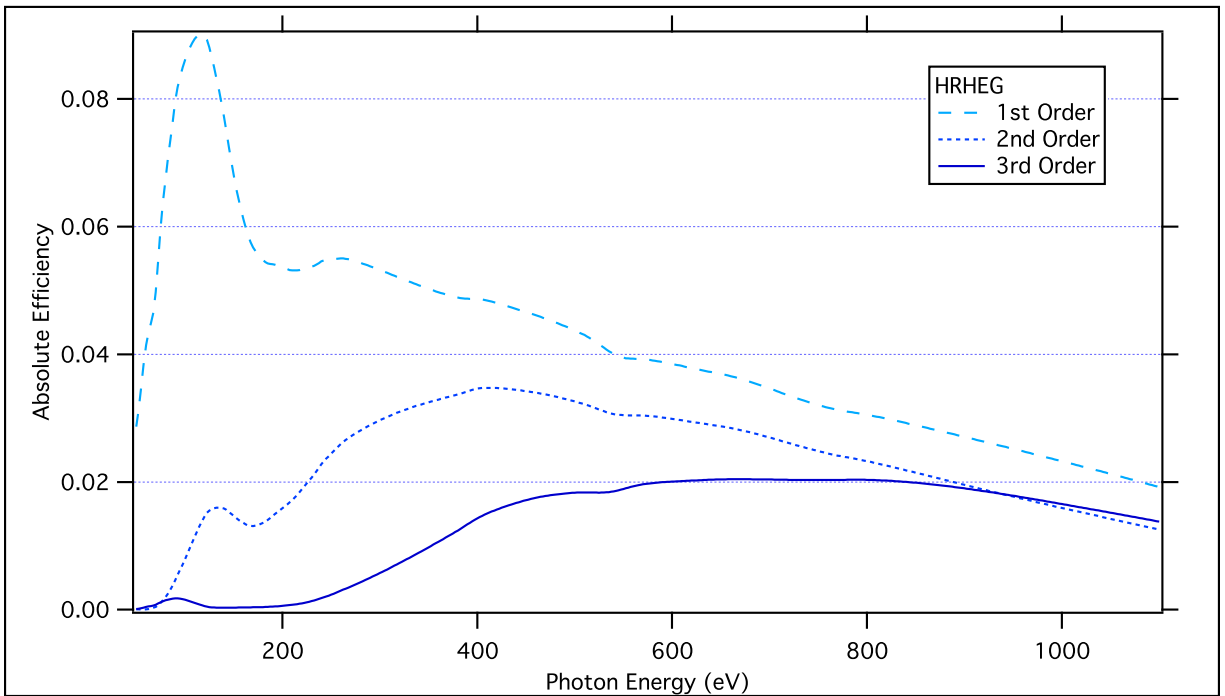


(b) High Energy Grating (HEG): 2000 lines/mm, 1.52 deg. blaze angle, Pt coating, for 88 deg. incidence

Figure 5.9: Theoretical diffraction efficiency for the Medium Energy and High Energy Gratings.



(a) High-res Medium Energy Grating (HRMEG): 1800 lines/mm, 4.85 deg. blaze angle, Ni coating, for 88 deg. incidence



(b) High-res High Energy Grating (HRHEG): 2600 lines/mm, 4.05 deg. blaze angle, Pt coating, for 88.25 deg. incidence

Figure 5.10: Theoretical diffraction efficiency for the High Resolution Gratings, optimized to be used in 3rd order.

CHAPTER 6

CHARACTERIZATION: HOW WE MEASURED THE ACTUAL GRATING PERFORMANCE, AND ACCOUNTED FOR DIFFERENCES

In the previous chapter, we applied grating efficiency calculations to create and optimize the optical design of the REIXS emission spectrometer. After having the design reviewed by an external consultant, who confirmed our resolution and efficiency predictions (TODO REF), we solicited bids from grating manufacturers and selected Bach Research to mechanically rule the six gratings. Finally, we passed the optical requirements over to a consulting engineer to design the mechanics of the spectrometer, which would be responsible for positioning the entrance slit, gratings, and detector, as well as achieving and maintaining ultra-high vacuum conditions throughout the beam path.

We lamented back in Chapter 4 the lack of published experimental comparisons of grating efficiency – particularly in the soft x-ray regime – and hypothesized that this was because beamline scientists, on receiving new gratings, were often eager to put them into their beamline and start commissioning, rather than spend more time characterizing them. Unfortunately¹, the construction of the REIXS spectrometer was delayed by a series of serious mechanical design flaws and oversights. Fortunately², this setback provided us with lots of time to characterize the ruling quality and real-world diffraction efficiency of our gratings. Even more fortunately, the characterization process alerted us to serious ruling errors with a few of the gratings, which would have dramatically affected the spectrometer’s resolution and efficiency had they not been discovered. In the end, our characterization of the gratings resulted in several beneficial outcomes:

- We were able to contribute another set of experimental comparisons to theoretical grating efficiency calculations.
- We discovered a reason to be cautious when specifying nickel-coated gratings, despite nickel’s apparently high reflectivity.
- We discovered a serious ruling problem in the HEG grating, which nearly eliminated its ability to diffract in the useful orders, and sent it back to the manufacturer for re-coating and re-ruling.
- We discovered substantial errors in the blaze angle (beyond the manufacturer’s specified tolerance) for

¹for us in our role as beamline staff

²for our interests in grating efficiency

a few of the gratings; in the case of the HRHEG, the blaze angle was off by so much that we ended up using it as a temporary replacement for the HEG.

This chapter describes these results, based on atomic force microprobe (AFM) measurements of the groove profile and soft x-ray diffractometer measurements of the actual grating efficiency. We also compare the calculated and measured grating efficiencies, and offer explanations for the differences.

6.1 AFM measurements of the manufactured grating profile

When we consider a grating like the HEG, with 2000 lines/mm and a blaze angle of 1.52° , it is clear that the physical size of the grooves is extremely small – these are little triangles about 500 nm wide and maybe 13 nm tall. Measuring the physical geometry is therefore actually impossible with a visible light microscope.

Instead, we used atomic force microscopy (AFM), an extremely high-resolution technique for measuring the topography of a surface. It uses an extremely sharp-tipped mechanical probe mounted on a piezo-electrically-controlled cantilever to “feel” the surface (Figure ??). The tip can either be dragged across the surface (contact mode) or electronically oscillated near its resonance frequency (*non-contact mode*) while measuring the change in amplitude, phase and frequency caused by the tip-sample atomic interaction forces. In both cases, the accurate vertical position of the tip is measured with a laser beam reflected off the back of the cantilever – using either an interferometer or a deflection meter – and the horizontal position of the tip is scanned using piezo drivers. The resolution of the best atomic force microscopes is sufficient to image individual atoms on a surface, although for measuring soft x-ray gratings we only need angstrom-level accuracy.

One limitation of AFM techniques is that it is easy to produce a two-dimensional map of the relative surface profile in arbitrary units, but difficult to accurately determine the absolute height. In order to measure blaze angles of gratings, we need to measure the height difference from the bottom to the top of the grooves in absolute units, which requires calibration of the AFM using a height standard. (Usually this is a gold mesh with an accurately-known wire size.)

After receiving the gratings from the manufacturer, we first imaged them using the AFM at the University of Saskatchewan Structural Sciences Centre (SSSC). However, we were not able to calibrate the z -axis for these measurements, so with the assistance of Dr. Eric Gullikson, we requested a complete set of measurements using the AFM at the Center for X-Ray Optics at the Lawrence Berkeley National Laboratory.

An example of an AFM scan is given in Figure 6.1, where we show both the two-dimensional image (top) and a cross-section of heights perpendicular to the grooves (bottom), which reveals the groove profile. Although the grooves should be ideally uniform along their entire length, most of the AFM scans show profile variation across even one image (a distance of just a few micrometers). To determine the average profile shape and average blaze angle, we integrated the two-dimensional image across the groove direction. Since a single AFM scan only spans a few micrometers of the grating, we also need to be careful in extrapolating the results

to the entire grating; therefore, we conducted multiple scans at the centre and the corners of the grating.

Figure 6.1 gives an example of the AFM output, for the LEG grating. We present groove profiles for all the gratings starting in Section 6.4, alongside a discussion of their effective diffraction performance.

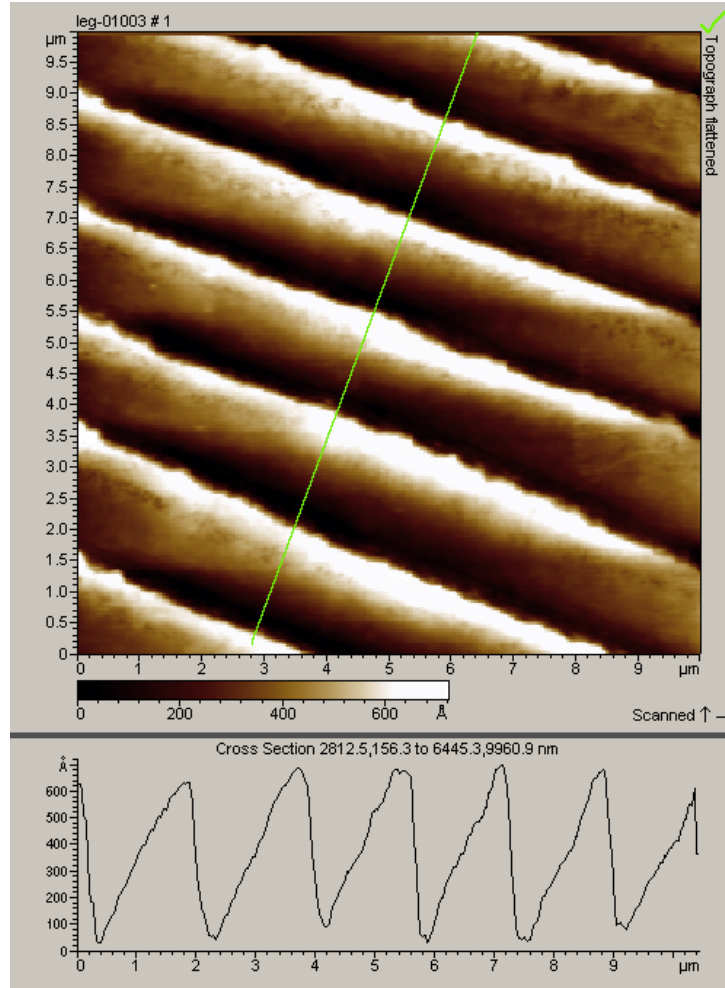


Figure 6.1: The Low Energy Grating has a smooth regular profile, shown in this example image measured using an Atomic Force Microprobe (AFM).

6.2 Diffractometer measurements of actual grating efficiency

To measure the actual grating efficiency, we used the reflectometer on the Calibration and Standards Beamline (6.3.2) at the Advanced Light Source. This beamline was designed specifically for testing the reflectivity of soft x-ray optical components like mirrors, thin films, multilayer coatings, and gratings. It consists of a bending magnet source, a VLS-PGM monochromator with a resolving power of 7000 (Figure 6.2), a higher-order suppressor, and a two-circle reflectometer (Figure 6.3). The beamline optics can focus the monochromator light to a small spot on the sample, or focus at infinite to generate parallel light (TODO REF http://ieeexplore.ieee.org/xpl/freeabs_all.jsp?arnumber=4994440).

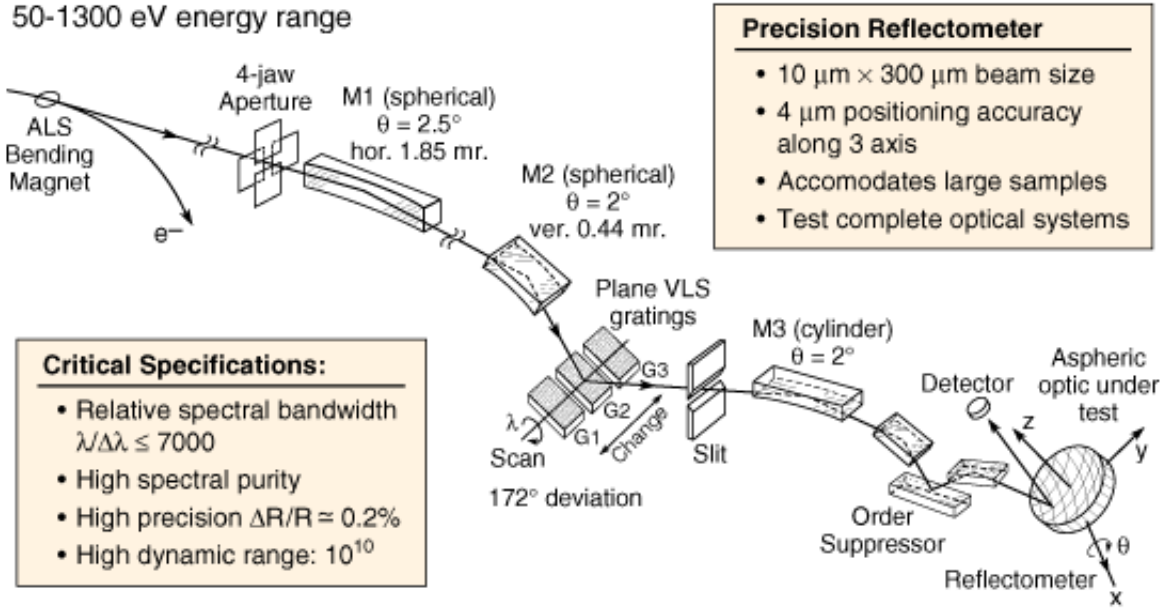


Figure 6.2: The Calibration and Standards Beamline (6.3.2) at the Advanced Light Source consists of a bending magnet source, a VLS-PGM monochromator with three selectable gratings, a higher-order suppressor, and a two-circle reflectometer shown in more detail in Figure 6.3. The curvature of refocussing mirror M3 can be adjusted to image the exit slit onto the sample, or to focus the light at infinite. **Image from:** (TODO REF <http://cxro.lbl.gov/als632/>)

6.2.1 Beamline 6.3.2 reflectometer

The purpose of the reflectometer endstation (Figure 6.3) is to measure the intensity of light reflected off a sample – in our case, a grating – as a function of both incidence and reflection angle. We used it to determine grating efficiency by positioning the grating at the intended incidence angle relative to the incoming beam, measuring the intensity at the angle of the outgoing order, and comparing this to the initial beam intensity. Upstream, the monochromator and order suppressor were used to produce the monochromatic incident beam and set its energy for each datapoint.

Inside the reflectometer mechanics, a “two-circle goniometer” provided independent control over the angle of the sample and the angle of the detector arm, as well as providing precise ($4 \mu\text{m}$) positioning to align the sample in x , y , and z . (Figure 6.4 shows the coordinate system convention, with angles measured from grazing incidence or inline with the beam; the “0 degree” sample position would place the grating at perfect grazing incidence, while the “0 degree” position for the detector would capture the incoming beam when unobstructed.) The sample holder could accommodate samples up to 200 mm in diameter, which allowed us to mount two of our gratings side-by-side at once. The detector arm contained a Hamamatsu gallium arsenide photodiode, a channel electron multiplier (CEM, or “channeltron”), and a CCD camera. For all of our grating measurements, we used the photodiode covered by a 2 mm pinhole.

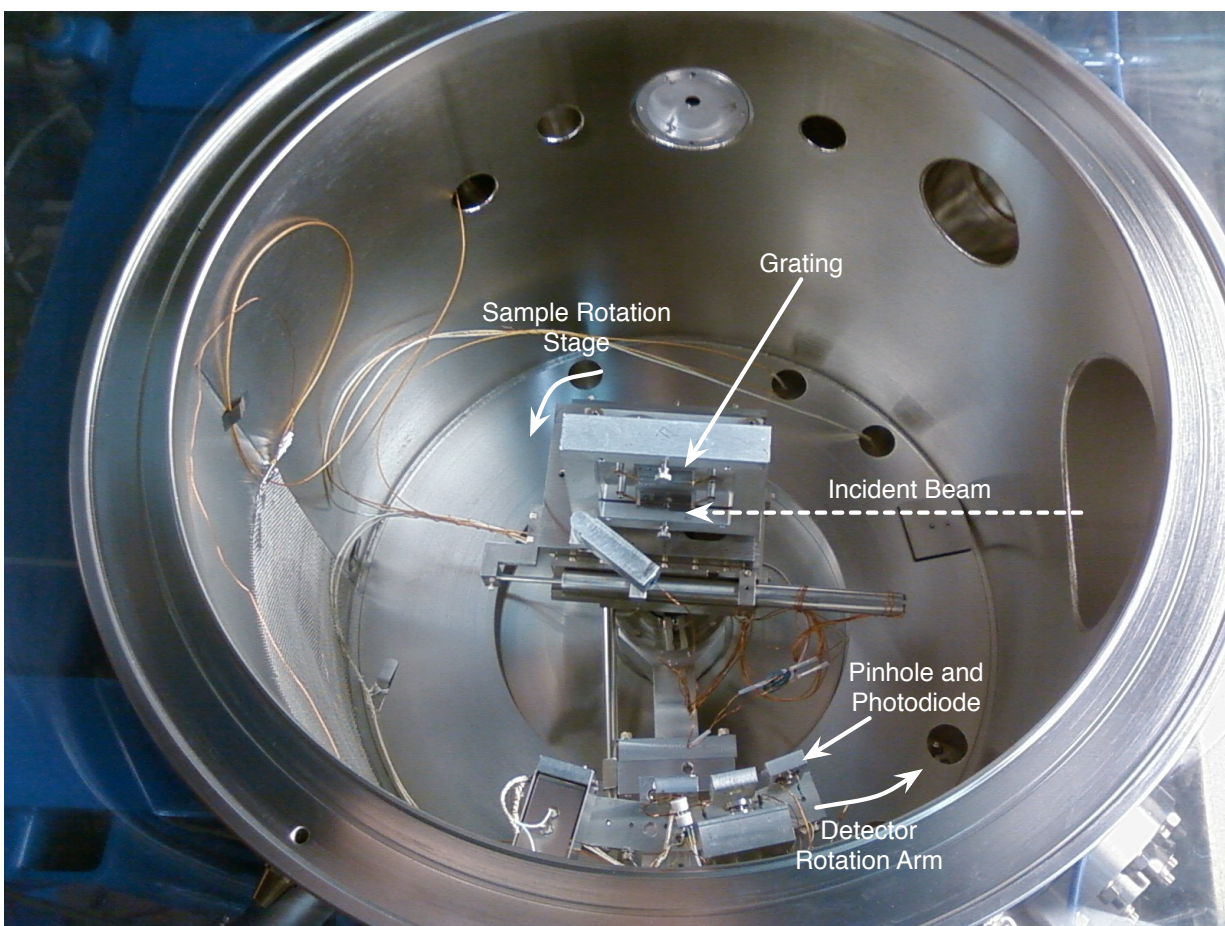


Figure 6.3: The reflectometer on Beamline 6.3.2 at the Advanced Light Source allows for independently setting the angle of the gratings in the beam, and setting the angle of a pinhole photodiode detector. Upstream, filters in the beamline are used to remove contamination from the higher-order light of the monochromator.

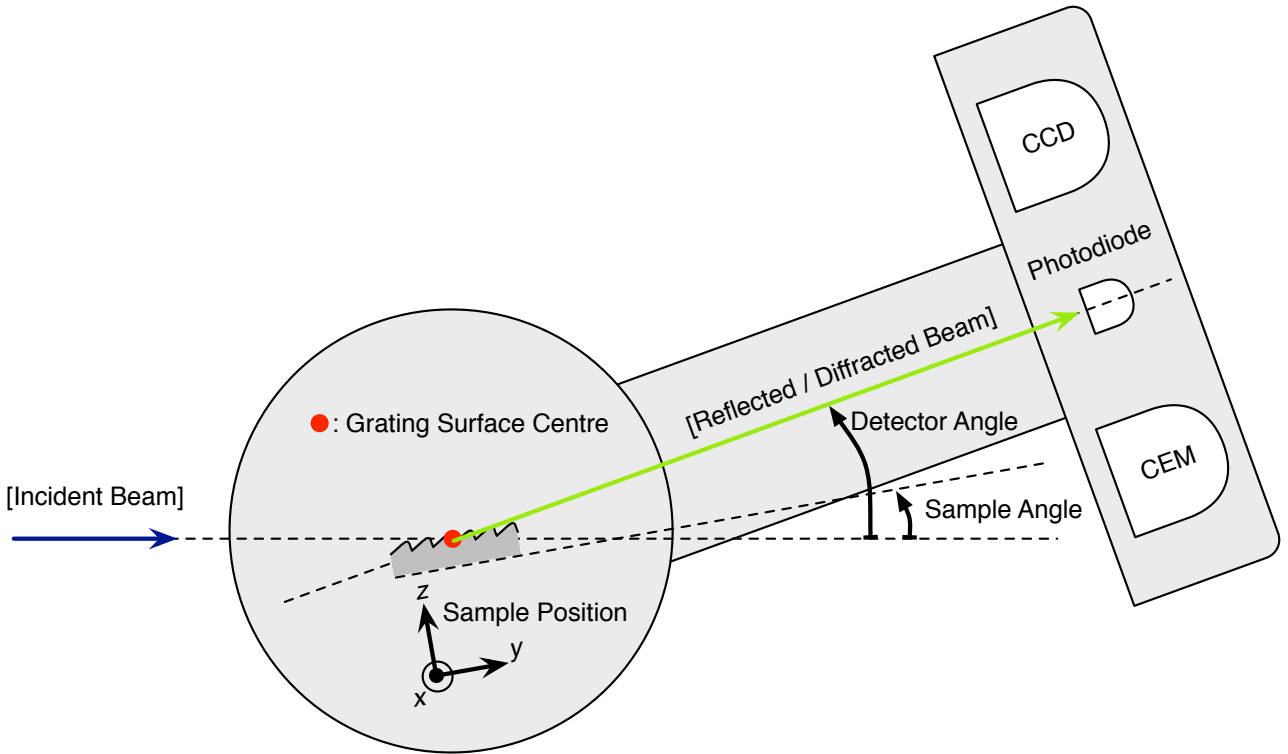


Figure 6.4: In the coordinate convention for the reflectometer, the sample angle is measured up from grazing incidence, and the detector angle is measured up from grazing incidence. The sample position stage (x, y, z) is mounted to the sample angle stage, so that the centre of rotation is always at the height of the beam.

6.2.2 Diffraction experiment procedure

Diffraction efficiency measurements are easily susceptible to a variety of systematic and unintentional errors. The following sections describe in detail the procedure we used for measuring the grating efficiency, and how we dealt with sources of error.

Grating Alignment

To achieve correct incidence angles and accurate detection angles, the grating had to be aligned correctly. In the z -direction (Figure 6.4), the centre of the grating surface had to coincide with the centre of sample rotation, which was also aligned to the height of the beam. In the x -direction (parallel to the grating grooves), the beam had to land on the centre of the grating; otherwise the curvature of the grating would introduce a slope in the sagittal direction, and we would end up with conical mounting.

1. To crudely align the grating in the z -direction, the grating angle was set to zero degrees, and the CCD camera was placed at a detection angle of 0 degrees. With the sample moved fully down out of the way in z , this allowed the beam to shine past the grating directly onto the centre of the CCD, confirming the alignment of the beam angle.
2. The grating was then moved upward in z until it just started blocking the beam from reaching the CCD detector, indicating that the surface was now at (or just above) beam height.
3. With the grating blocking the CCD detector in this position, it was translated in x until light returned, indicating that the beam had fallen off the side edge of the grating. This was repeated in the $(-x)$ -direction, providing us with the position of the opposite side; the grating was then positioned midway between these two positions, achieving alignment in x .
4. To accurately complete the alignment in z , the grating was angled at two degrees, and the photodiode detector was positioned to collect reflected (0th order) light at four degrees. As long as the beam was incident on the grating, this would register a signal on the detector. The grating was then translated upward in z until the signal disappeared, indicating that the beam had fallen off the bottom edge of the grating. This z -position was recorded as the bottom grating edge.
5. The grating was then lowered in z until the signal disappeared again, indicating that the beam had fallen off the top edge of the grating. This z -position was recorded as the top grating edge, and then the grating was moved to the average of the two recorded z -positions; this process ensured that the beam was now incident on the exact centre of the grating.

Scanning modes

All of the efficiency plots we calculated in Chapter 5 to predict the REIXS gratings' performance show efficiency as a function of photon energy. We wanted to show our real-world measurements in the same

format, which required us to scan the monochromator energy while measuring the intensity of the desired order with the photodiode. Therefore, the detector angle had to change as we changed the monochromator energy, according to the outgoing angle specified by the grating equation (Equation 3.61).

If we had known the groove density very accurately, we could have calculated the correct diffraction angle and positioned the detector simultaneously while scanning the monochromator energy. However, for brand new gratings, it would be unlikely for the groove density to end up exactly as requested from the manufacturer; in this case we would actually need to conduct a two-dimensional scan: for every photon energy datapoint, we would need to conduct an angular scan of the photodiode to find the diffraction peaks.³

For four of the gratings, we did have an accurate groove density, obtained from Power Spectral Density (PSD) measurements taken by the metrology lab at the Canadian Light Source. However, for two of the gratings, the exact groove density was unknown, so we had to use the two-dimensional scan method. Mechanically, this is actually the simplest way to operate the reflectometer, and an example of the results are shown in Figure 6.5. The procedure was as follows:

1. The monochromator was set to the desired photon energy, and the corresponding filters were selected in the higher-order absorber.
2. The grating was positioned at its specified incidence angle relative to the beam, as it would be during operation of the spectrometer.
3. The photodiode was scanned, recording intensity as a function of outgoing angle.
4. The grating was moved out of the way of the beam, and the photodiode was placed at zero degrees to measure the direct beam intensity; this intensity value was used to normalize the data as described later in this section.
5. The results (Figure 6.5) show the intensity of reflected light as a fraction of the incident beam intensity, as a function of detector angle. The 0th order, 1st order, and 2nd order peaks are clearly seen; we can quickly check that the 0th order peaks show no wavelength dependency and occur at twice the incidence angle. The grating efficiency in the n th order is taken from the height at the centre of the n th diffraction peak.

This procedure had to be repeated for every photon energy datapoint that we wanted to test, and this could be tedious. For the gratings where the groove density was known accurately, we used a more expedient method, which required synchronized scanning of the detector angle and monochromator energy:

1. The higher-order suppressor was configured for the energy range of the scan. (This limited each individual scan to the valid energy range of a single higher-order filter; see Section 6.2.3)

³After completing this scan, we could use the angular position of the diffraction peaks to calculate the actual groove density, but only within a precision determined by the angular extent of the 2mm photodiode pinhole.

2. The control software was configured to move the detector angle in tandem with the monochromator energy to stay on top of the diffraction peak, using the grating equation and the specified groove density and order.
3. The monochromator energy and the detector angle were scanned together, recording the intensity of the diffracted order at each datapoint.
4. The grating was then moved out of the way of the beam, and the detector angle was set to zero degrees to measure the direct beam. The monochromator energy scan was repeated to measure the incident intensity as a function of energy, to use for normalization (see ‘Normalization’, below).
5. An example of the normalized results is shown in Figure 6.6. They directly show the intensity of diffracted light in the specified order as a fraction of the incident beam intensity, as a function of energy. With this method, it is easier to measure a finely-spaced set of datapoints along the energy axis, to compare with our efficiency prediction plots in Chapter 5.

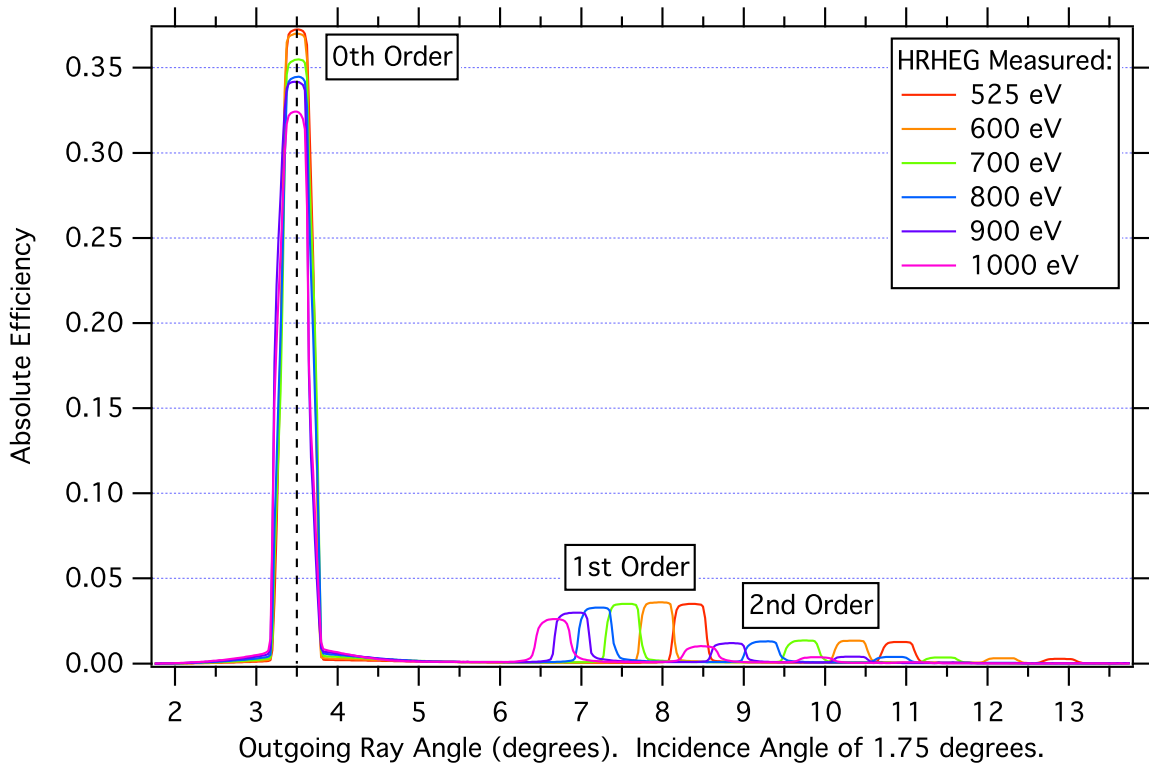


Figure 6.5: The simplest diffractometer experiment scans the detector angle while illuminating the grating with a constant photon energy. The diffraction orders are visible as peaks along the outgoing angle axis (measured up from the incident beam direction at 0°). The 0th order (reflection) peak is easily visible at 3.5° , or twice the incident angle (88.25° , or 1.75° from grazing). Grating: HRHEG.

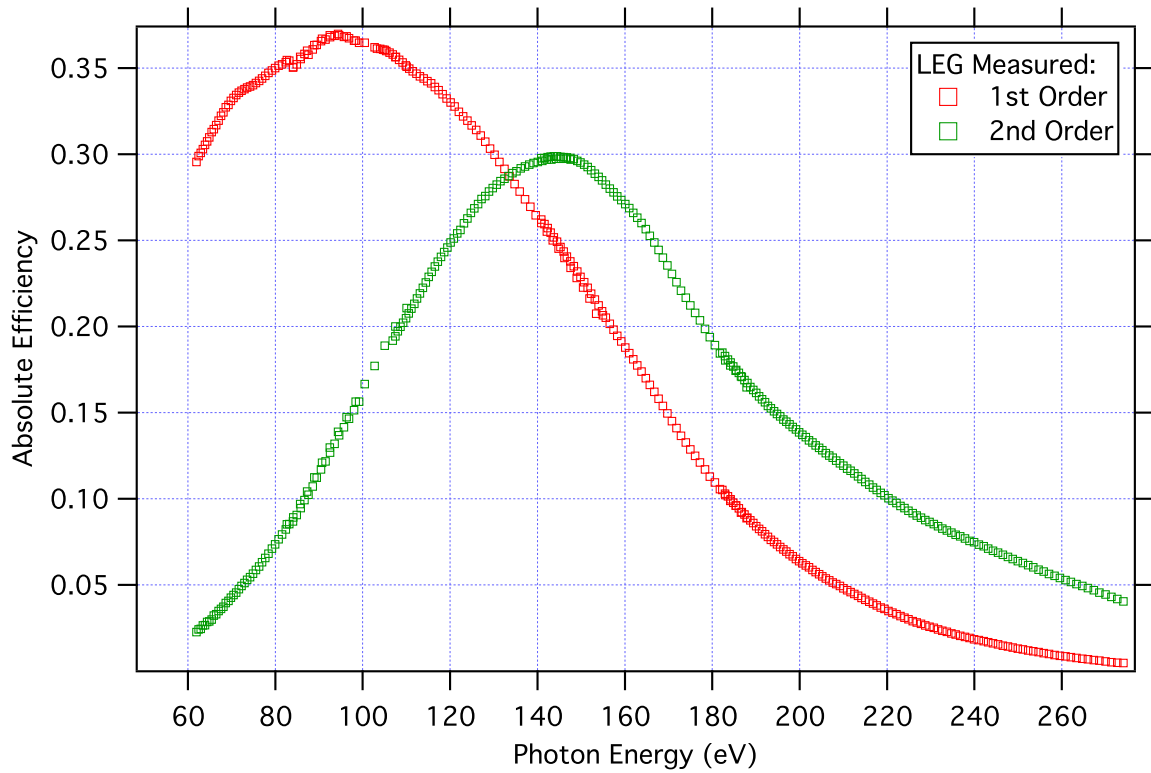


Figure 6.6: When the groove density of a grating is accurately known, the detector angle can be moved in tandem with the monochromator energy to keep it on the diffraction peak as the incident photon energy is scanned. This allows faster, nearly continuous efficiency measurements as a function of photon energy. (Grating: LEG)

Wavelength calibration

The monochromator on Beamline 6.3.2 is slitless, therefore its absolute energy calibration is affected by the position of the beam in the ALS storage ring. To calibrate the energy axis of our data, we scanned the monochromator through the absorption edges of the higher-order suppression filters, and compared the onset of the edges with the published values for the binding energies of these elements:

1. For every new energy range, monochromator grating change, or storage ring refill, the sample was moved out of the way and the photodiode was placed at 0 degrees to measure the direct beam.
2. The monochromator was scanned upward in energy through the onset of the nearest absorption edge of a filter placed in the beam path. (For example, prior to doing scans in the energy range from 82.6 to 112 eV, we installed the silicon filter and scanned across the Si $L3$ absorption edge, located at 99.42 eV.) Essentially, this amounted to measuring a transmission x-ray absorption spectrum of the filter element.
3. The wavelength shift of the onset of the absorption edge (in monochromator wavelength units) away from its theoretical position provided a correction offset that was applied to the wavelength axis for all scans in this range.⁴

Normalization

Chapter 3 defined grating efficiency as the ratio of the intensities of the n th order diffracted beam and the incident beam. In our measurement procedure (above), we used the photodiode to record the intensity of the reflected beam I_r , and subsequently the intensity of the incident beam I_i . The efficiency $e^{(r)}$ would then be

$$e^{(r)} = \frac{I_r}{I_i} \quad (6.1)$$

Using the same detector to measure both the reflected and incident beam eliminates error due to differences in detector sensitivity. However, because these measurements were not taken simultaneously, it is possible that the incident beam intensity would have changed in the interim; in fact, this would be virtually guaranteed due to decay of the storage ring current over time. Because the light intensity of a bending magnet beamline is proportional to the storage ring current J_{ring} , we can record the ring current at the time of each measurement, and use it to normalize the intensities:

$$e^{(r)} = \frac{I_r/J_{\text{ring},r}}{I_i/J_{\text{ring},i}} \quad (6.2)$$

Finally, as we identify in the following section, the dominant source of error in low-light photodiode measurements is the *dark current*: an intensity-independent signal from the photodiode that increases with

⁴The monochromator control software used wavelength units rather than energy units, so we conducted all of our efficiency scans in wavelength units and converted later from nm to eV, using the photon energy relationship $E = hc/\lambda$.

temperature due to thermal generation of electron-hole pairs. With the beam blocked, we measured the dark current I_{dark} for every gain setting of the photodiode, and subtracted this contribution from all measurements to determine the true intensity ratio:

$$e^{(r)} = \frac{(I_r - I_{\text{dark}})/J_{\text{ring},r}}{(I_i - I_{\text{dark}})/J_{\text{ring},i}} \quad (6.3)$$

We used Equation 6.3 to normalize all of the efficiency results in Section 6.4.

6.2.3 Sources of error

In the previous description of our procedure, we briefly mentioned the “higher-order suppressor”, the dark current, and the energy calibration. In this section, we take a look at all of the sources of error which could affect the grating efficiency measurements.

Higher-order contamination

A bending magnet source like the one on Beamline 6.3.2 produces light of all wavelengths, from infrared to hard x-rays; it is the responsibility of the monochromator to extract a single wavelength from this broadband input. The problem with grating monochromators, however, is that the grating equation cannot distinguish between equivalent products of n and λ : light with a wavelength of x nanometers diffracted in 1st order will leave at the same angle as $x/2$ -nanometer light diffracted in 2nd order.⁵ When both wavelengths are present in the monochromator input, this creates what is known as “higher-order contamination” in the output. Because the monochromator gratings are likely more efficient in 1st order than any other, the intensity of $x/2$ and $x/3$ -nanometer light will be comparatively lower than the desired wavelength, but it will still contaminate the mono output. If this higher-order light were to arrive at the grating under test, it would be diffracted again, introducing additional erroneous peaks into the detector angle scan. (Depending on the ratio of the monochromator and test-grating groove densities, these erroneous peaks could either overlap or fall beside the “true” diffraction peaks.) Therefore, reflectometry experiments require a method to eliminate this higher-order light before it reaches the sample.

Beamline 6.3.2 has two techniques for higher-order suppression. The first is a variable-incidence mirror with multiple sets of coating stripes. This design exploits the change in reflectivity as a function of incidence angle and energy that we saw (for example) in Figure 4.17. Depending on the desired wavelength, the mirror coating and grazing angle are chosen to provide high reflectivity at the desired wavelength, but significantly lower reflectivity at fractionally-shorter wavelengths. (TODO find ref)

The second technique is a filter wheel containing a set of transmission filters from various elements which may be inserted into the beam path prior to the endstation. The filters are between 300 nm and 1 μm thick, and are designed to remove 50% or more of the light at energies above the filter’s absorption edge.

⁵In terms of energy, photons with an energy of y eV will diffract in 1st order to the same angle as $2y$ -eV photons in 2nd order.

Table 6.1 shows the mirror coating, mirror angle, and filter element that we used for higher-order suppression. The energy ranges of each mirror/filter combination (shown in the left column) restricted the maximum extent of each efficiency scan; for the efficiency results shown in Section 6.4, we have combined multiple scans together.

Table 6.1: For higher-order suppression, Beamline 6.3.2 has a variable-incidence mirror and a set of transmission filter elements. The mirror coating, mirror angle, and filter need to be selected based on the energy range of the scan. (Mirror angles are measured from grazing incidence.)

Energy Range (eV)	Mirror	Mirror Angle ($^{\circ}$)	Filter
62 - 99	Carbon	10	Silicon
83 - 112			Beryllium
103 - 155		8	Boron
141 - 188		6.2	
182 - 276	Nickel	8	Carbon
275 - 454			[None]
441 - 546	[None]		Chromium
544 - 775			Cobalt
751 - 932			Copper
898 - 1305			Magnesium

Monochromator energy calibration

The monochromator is approximately calibrated, so that entering a wavelength set-point into the control software – for example, 2.73 nm – will align the mono grating to diffract light of approximately 2.73 nm out through the exit slit. However, the calibration is not perfect, and it is also affected by shifts in the ALS electron beam orbit position. Therefore, it is important to obtain an absolute wavelength calibration whenever moving to a substantially different wavelength range, changing monochromator gratings, or resuming scans after a storage ring refill.

As described in the procedure, we calibrated the wavelength axis of our efficiency scans (eventually, the energy axis) by conducting transmission absorption spectroscopy on the filter elements in Table 6.1. The difference between the monochromator’s apparent wavelength at the halfway height of the absorption edge, and the wavelength corresponding to the published binding energies for those elements, was used to generate a wavelength offset for nearby scans. (The monochromator’s calibration might also suffer from errors which require linear and quadratic scaling corrections, but we assumed that a simple offset would be sufficient over the short length of these scans.)

Photodiode dark current

Photodiodes can be operated in a forward-biased (*photovoltaic*) mode, or in a reverse-biased (*photoconductive*) mode. When used as sensitive detectors of light intensity, the photoconductive mode is almost always used, because it offers faster response times and a linear response to light intensity over many orders of magnitude. In this mode, a reverse bias is applied and – in the absence of light – only a small *dark current* flows through the diode, due to the thermal generation of electron-hole pairs in the $p - n$ junction. When light strikes the $p - n$ junction, incident photons create electron-hole pairs which are swept across the junction by the reverse bias, and create an intensity-dependent *photocurrent*. The total current through the photodiode is measured by a sensitive current amplifier.

The dark current depends on temperature, and slightly on the magnitude of the reverse bias voltage. (In our instrumentation, the reverse bias was affected by the gain setting of the current amplifier.) To account for this, we measured the dark current at every gain setting with the beam turned off, and then subtracted this in the normalization equation (Equation 6.3). The dark current measurements were conducted after the diode had been operating under reverse bias for some time (and hopefully had reached operating temperature). Since the dark current increases with temperature, it is possible that exposure to extreme intensity would heat the detector and change the dark current contribution; however, this effect should be negligible for the low intensities observed in our experiment.

Saggital tilt of the grating

The reflectometer mechanics enable the intended rotation of the sample (grating) around the x -axis in Figure 6.4. If the grating surface were tilted away from normal incidence around the y -axis – either due to an offset in the grating mount, or due to the curvature of the grating combined with incorrect alignment in the x -direction – light would be reflected out of the $y - z$ plane. This would create the “conical mount” situation we assumed we could avoid modelling in Chapter 3, and would also cause the diffracted beam to partially or completely miss the 2 mm pinhole of the photodiode detector. Both of these effects would reduce the observed intensity from what we would expect.

The zero-order alignment test we described in the procedure confirmed that with the grating positioned at 2 degrees, a substantial current was observed on the photodiode at 4 degrees, indicating that a substantial amount of light was staying within the plane of incidence. However, we cannot confirm that the alignment was flawless, and it is possible that the measured efficiencies are lower than they would be under perfect alignment.

Limited beam spot size

The Beamline 6.3.2 optics focus the beam to a spot size of 0.010 mm x 0.3 mm on the grating. (TODO check if we were focussed at grating or infinite.) Because the grating needs to be aligned on the centre of rotation, there can only be one position for the beam on the grating, and so we could only test the efficiency at this

point. If there is variation in the groove profile across the grating, the illuminated part of the grating may not actually be representative of the average efficiency.

It is impossible to overcome this limitation; even if it were possible to fully illuminate the grating, the grating curvature would not be correct to focus the diffracted beam to the same size on the detector as the incident beam would be. Therefore, a small beam size is a necessary compromise to minimize the focussing effect of the grating.

Energy dispersion across detector pinhole (finite size of pinhole + finite resolution dE)

TODO need to discuss with Eric Gullikson

Focussing / Defocussing

TODO need to discuss with Eric Gullikson

6.3 Real-world grating effects

The comparisons between the predicted and measured efficiencies for each grating are discussed in Section 6.4, and impatient readers might have already beat us there. However, before looking at the results, it might be useful to consider some of the factors that could cause a discrepancy between the two. If there are differences between the predicted and measured efficiency, this would imply one – or more – of three distinct possibilities:

1. That the measurement procedure, due to experimental error, did not measure the actual grating efficiency.
2. That the theory and calculation method do not correctly describe the gratings they attempted to model, or,
3. That the real-world gratings, as produced, are different from the ones we modelled.

We dealt with the first possibility in the previous section on sources of error. Before accepting the second possibility, we take a look at some of the ways manufactured gratings differ from ideal ones.

6.3.1 Stray radiant energy

For a perfectly periodic surface, the Rayleigh expansion in Chapter 3 showed that all of the light propagating away from a grating leaves as plane waves in discrete orders. Regardless of the groove shape, no light leaves except at the angles given by the grating equation (Equation 3.61). In real-world gratings, deviations from perfect periodicity lead to *stray radiant energy* (SRE), which is a general term for all radiation that leaves at other angles. (TODO REF <http://gratings.newport.com/information/technotes/technote9.asp>) Due to

conservation of energy, the more SRE that exists, the less energy there is in the desired orders, and the lower the grating efficiency. SRE also affects the resolution of a grating instrument, by increasing the background noise level and contaminating the outgoing angles with light of the wrong wavelength.

Stray radiant energy can be caused by microroughness of the grating surface, variation in the height or spacing from groove to groove, and other imperfections such as dust and scratches.

Surface roughness

The grating model in Chapter 3 assumed a perfectly smooth surface, given by the periodic profile $y = g(x)$ in Figure 3.1. Unfortunately, both ruling and coating processes invariably leave a certain amount of microroughness, shown exaggerated in Figure 6.7. When the surface is rough on the scale of the incident wavelength, it causes diffuse scattering, which is analogous to the diffuse (or non-specular) reflection that would occur off any rough surface. Because this phenomenon affects the entire area of the grating, diffuse scattering from surface roughness is typically responsible for most of the reduction in real-world grating efficiency (compared to theoretical calculations).

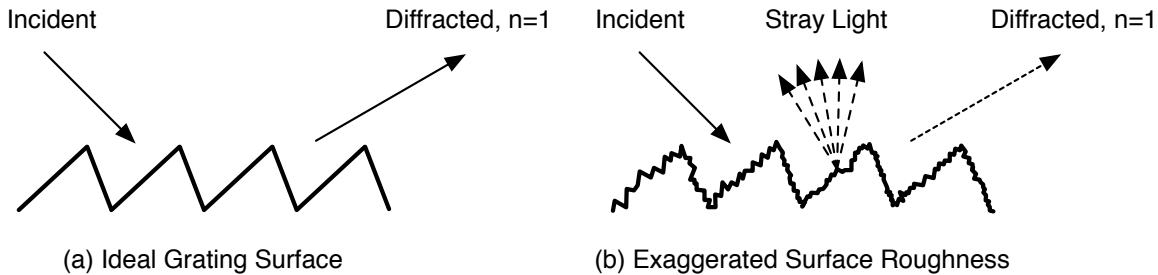


Figure 6.7: Roughness of the grating surface scatters stray light outside the diffraction orders. Typically, surface roughness is responsible for most of the reduction in real-world grating efficiency, compared to theoretical calculations.

Although it might not be clear from Figure 6.7 – which is two-dimensional – diffuse scattering need not be constrained to the plane of incidence. The roughness creates slope variation in both x and z , so scattered light could end up anywhere in the hemisphere above the grating. However, in-plane scattering is stronger than out-of-plane scattering by a factor of $1/\cos\theta$ (where θ is the incidence angle from normal). Therefore, at grazing incidence, the in-plane scattering is dominant. (TODO REF http://www2.astro.psu.edu/niel/astro485/xrayschool/schwartz-xray_optics.pdf)

To correct the predicted grating efficiencies for scattering, we need to understand two things:

1. The amount of energy lost to scattering, as a function of roughness, wavelength, incidence angle, and diffraction order.
2. The angular distribution of the scattered intensity. Does it affect all diffraction orders the same way?

Given the randomness of the surface structure, we need statistical methods to answer these questions. Statistically, the surface roughness is characterized by σ , the root mean square (RMS) variation in height from the nominal plane, and by the power spectral density (PSD) function, which describes how the height variation is distributed in frequency.

Even for the simpler (non-grating) case of roughness on flat surfaces, a substantial amount of research has only succeeded in producing a murky swamp of approximate models. (TODO REF Elfouhaily and Guerin) categorized 260 references – 177 since 1980 – into 30 different methods, before concluding that “there does not seem to be a universal method that is to be preferred systematically. All methods present a compromise between versatility, simplicity, numerical efficiency, accuracy and robustness, with a different weighting in these various fields. [...] No approximate model has fulfilled all listed criteria”

Even though they only deal with nominally flat surfaces, all of these methods are based on the assumption that a random rough surface can be decomposed into a superposition of sinusoidal gratings⁶, and that scattering can be explained as a diffraction effect from the phase changes created by the “microtopography” of the surface. (TODO REF Modified Beckmann-Kirchhoff scattering model for rough surfaces with large incident and scattering angles Opt. Eng. 46, 078002 (Jul 02, 2007); doi:10.1117/1.2752180) There are two fundamental approaches: the Rayleigh-Rice theory (TODO REF Lord Rayleigh, On the Dynamical Theory of Gratings, Proc. Roy. Soc. A79, 399-416 (1907)., S. O. Rice, Reflection of Electromagnetic Waves from Slightly Rough Surfaces, Commun. Pure Appl. Math., vol. 4, 1951, p.351.,), which is a perturbation approximation for solving the electromagnetic vector wave equation near periodic interfaces, and the Beckmann-Kirchhoff theory, which uses a scalar wave equation and applies the Kirchhoff diffraction formula (TODO REF P. Beckmann and A. Spizzichino, The Scattering of Electromagnetic Waves from Rough Surfaces; Pergamon, New York, 1963, Chaps. 4 and 5.). Both contain approximations; the Rayleigh-Rice methods are only applicable to “smooth” surfaces, where the perturbation from a flat surface is small – i.e., where the RMS roughness is small compared to the wavelength ($\sigma \ll \lambda$). The Beckmann-Kirchhoff methods are appropriate for “rougher” surfaces up to ($\sigma \cos \theta \leq \lambda$), but they contain a small-angle approximation that restricts them to near-normal incidence and scattering angles (TODO REF modified). (In the extreme case where the roughness is much larger than the wavelength, it becomes more appropriate to handle it using a geometric optics approach, rather than a diffraction approach. In this situation, we can imagine a surface made up of many “microfacets” all reflecting light at different angles; the BESSY raytracing software suite actually uses this approach to model roughness by randomly varying the direction of a mirror’s normal vector (slightly) for each reflecting ray, according to the statistical description of the surface (TODO REF bessy RAY paper.)

Since grating theories are already being used to describe diffuse scattering from rough *flat* surfaces, applying these methods to *actual* gratings is even more difficult; this amounts to creating a superposition of (very high density) gratings, *on the surface of a grating*(!)

It would be theoretically difficult to analyze “gratings structured on top of gratings”, so instead, we apply

⁶Obviously, in our case, of much higher groove density than the actual gratings!

some of the results for rough mirrors to come up with an approximate correction for our grating efficiencies. Many texts and computer programs use a simple expression called the “Beckmann factor”

$$R' = R \exp \left(- \left(\frac{4\pi\sigma \cos \theta}{\lambda} \right)^2 \right) \quad (6.4)$$

to approximate the reflectivity R' of a real mirror, where R would be the reflectivity of an ideally smooth surface. However, this is subject to the small-angle approximation in the Beckmann approach, and predicts that the reflectivity is essentially unchanged when approaching grazing incidence due to the $\cos^2 \theta$ term in the exponential.

Based on a the x-ray-specific work of (TODO REF <http://link.aps.org/cyber.usask.ca/doi/10.1103/PhysRevB.38.2297>), the X-ray Data Booklet (TODO REF) gives a correction factor of

$$R' = R \exp \left(- \left(\frac{4\pi\sigma}{\lambda} \right)^2 \sin \theta \operatorname{Re} \left[\sqrt{n^2 - \sin^2 \theta} \right] \right) \quad (6.5)$$

where n is the complex refractive index.⁷ This was derived from the “distorted-wave Born approximation”, which uses a Rayleigh-Rice-like perturbation approach; it is far more accurate in the limit of grazing incidence.

By analogy from reflectivity (“fraction of incident light reflected”) to grating efficiency (“fraction of incident light reflected in order n ”), we have used the same factor to determine the form of the roughness correction to apply to the grating efficiencies:

$$e'_n = e_n \exp \left(- \left(\frac{4\pi\sigma}{\lambda} \right)^2 \sin \theta \operatorname{Re} \left[\sqrt{n^2 - \sin^2 \theta} \right] \right) \quad (6.6)$$

Since we do not have measurements of each grating’s RMS roughness, we used σ as a free parameter to attempt to fit the theoretical efficiencies to the measured efficiencies; the results are shown in Section 6.4.

Although we do use this mirror expression to correct our predicted efficiencies, it is important to note that roughness on gratings may actually cause different effects than roughness on flat mirrors. (TODO REF <http://www.gratinglab.com/information/handbook/chapter10.asp#10.1.1>) reports that the diffuse scattering is not isotropic; within the plane of incidence, the intensity is stronger at angles near the diffraction orders than it is between orders. (TODO REF M. R. Sharpe and D. Irish, ”Stray light in diffraction grating monochromators,” *Opt. Acta* 25, 861-893 (1978)) analyzes scattering specifically from gratings, and indicates that the intensity of scattering increases as the fourth power of the energy. (TODO REF Angular distribution of light scattered from a sinusoidal grating 1 September 2000 Vol. 39, No. 25 APPLIED OPTICS) looks at sinusoidal gratings illuminated by coherent visible light, and confirms that surface roughness increases the background light level. (TODO REF L. Nevot, P. Croce, *Rev. Phys. Appl.* 15, 761 (1980). 10.1051/rphysap:01980001503076100) provides another comprehensive study of rough gratings, and comes to a result consistent with Sinha et. al. (Equation 6.6), although through a different method.

⁷TODO REF gives the complex reflection coefficient, instead of the reflectivity. Compared to the expression given there, we have converted from grazing incidence angles to normal incidence angles, and multiplied by the complex conjugate to determine the reflectivity.

Figure TODO shows the reduction in efficiency caused by different amounts of roughness, over the range of soft x-ray energies. These were calculated at grazing incidence using the Sinha approach, so we are limited to RMS roughnesses much smaller than the wavelength. The Beckmann (Equation ??) and Sinha (Equation 6.6) factors are compared in Figure TODO, showing the limits of each one’s applicability.

Figure TODO reinforces how important it is to keep the roughness low during manufacturing. Our AFM measurements suggest that re-coating the grating after ruling adds to the roughness, due to the granular nature of the evaporated coating. Due to extensive manufacturing experience, gold coatings are usually the smoothest to apply – as was the case for our LEG. The subsequent platinum and nickel overcoatings on the remaining gratings resulted in a much rougher surface.

Dust, scratches, and pinholes

Dust, scratches, pinholes, and any other out-of-place bumps on the surface also contribute to the stray radiant energy. All of these features act as scattering centres and create diffuse light; we can easily confirm this for visible wavelengths (using our biological photodetectors) when looking at a dirty grating under bright light. Given the challenges of modelling statistically well-behaved surface roughness, we do not even attempt to model these purely random defects, beyond recognizing that they will reduce the overall grating efficiency and contribute to stray light.

Periodic irregularities of the grooves: ghost peaks

In the section on grating manufacturing (Section 4.3.1), we mentioned that periodic errors in the groove position or groove height will create “ghosts”: additional light intensity peaks superimposed over the desired diffraction pattern. This happens because the higher-order structure acts like a superimposed grating with its own periodicity. Just like the other causes of stray radiant energy, these peaks – if present – will remove energy from the desired diffraction orders, and contaminate the resolution by directing light to the “right place at the wrong wavelength”.

Irregularities along the groove: out-of-plane reflection

We assumed in Chapter 3 that the grating was invariant (i.e., did not change) along the z direction of the grooves. When ruling a mechanical grating, changes in the elasticity of the metal will allow the tip to penetrate to different depths, causing variation in the shape of the profile along the grooves. (This also occurs with holographic gratings, due to variation in the mean intensity of the interference pattern during exposure.) Shape variation along the grooves can reflect light out of the plane of incidence, and the effect can be diffuse or specular.

Elasticity changes will also cause random (non-periodic) variation in the groove depth from groove-to-groove. This has been shown to create a continuous distribution of scattered light which increases as a function

of $(1/\lambda^3)$ (TODO REF M. R. Sharpe and D. Irish, "Stray light in diffraction grating monochromators," Opt. Acta 25, 861-893 (1978).)

6.3.2 Manufacturing errors the *can* be modelled

All of the previous real-world grating flaws – surface roughness, dust and scratches, periodic and non-periodic groove irregularities – represent deviation from the theoretical profile we modelled in Chapter 3, in ways that cannot be incorporated into the model without breaking our initial assumptions (Section 3.1.1). It is also possible for manufacturing errors to create deviation that we *can* actually model; the best example of this would be differences between the requested and manufactured groove geometry.

Profile errors: Blaze angle errors shift the efficiency peak

Figure 4.19 showed how small (0.1°) changes in the blaze angle can significantly shift the efficiency peak. For mechanically-ruled gratings, the accuracy of the blaze angle depends on the persistence and perfectionism of the ruling engine operator, who must adjust the diamond tip angle during setup through tedious trial-and-error. If, after manufacturing, the real blaze angle turns out to be different than what the customer specified – always true to some degree – we can measure the true blaze angle using a calibrated AFM, and re-calculate the theoretical efficiencies using a better approximation of the profile.

Alternatively, if calibrated AFM measurements are not available, we have determined that the shape of the measured efficiency curves and the ratio between 1st and 2nd order efficiency can provide a strong indication of the real blaze angle. (For example, by choosing the best-fit blaze angle to match the measured and calculated efficiency curves, we predicted a blaze angle of 2.0° for the MEG grating, before determining from AFM measurements that the real blaze angle was 2.04° .) In Section 6.4, we discuss the blaze angle agreement for each grating.

The same techniques can be applied to profiles other than blazed gratings; the first method works as long as the groove geometry (Figure 4.5) can be measured. For profiles like trapezoidal gratings that have three – instead of just one – adjustable parameters, it becomes more involved to try to estimate the best-fit geometry, but this can be accomplished using multidimensional minimization algorithms.

Coating oxidation changes the reflectivity spectrum

6.4 Grating results

: (and comparison to theoretical)

6.4.1 LEG

(gold): profile clean; as expected; blaze angle off. [modelled]

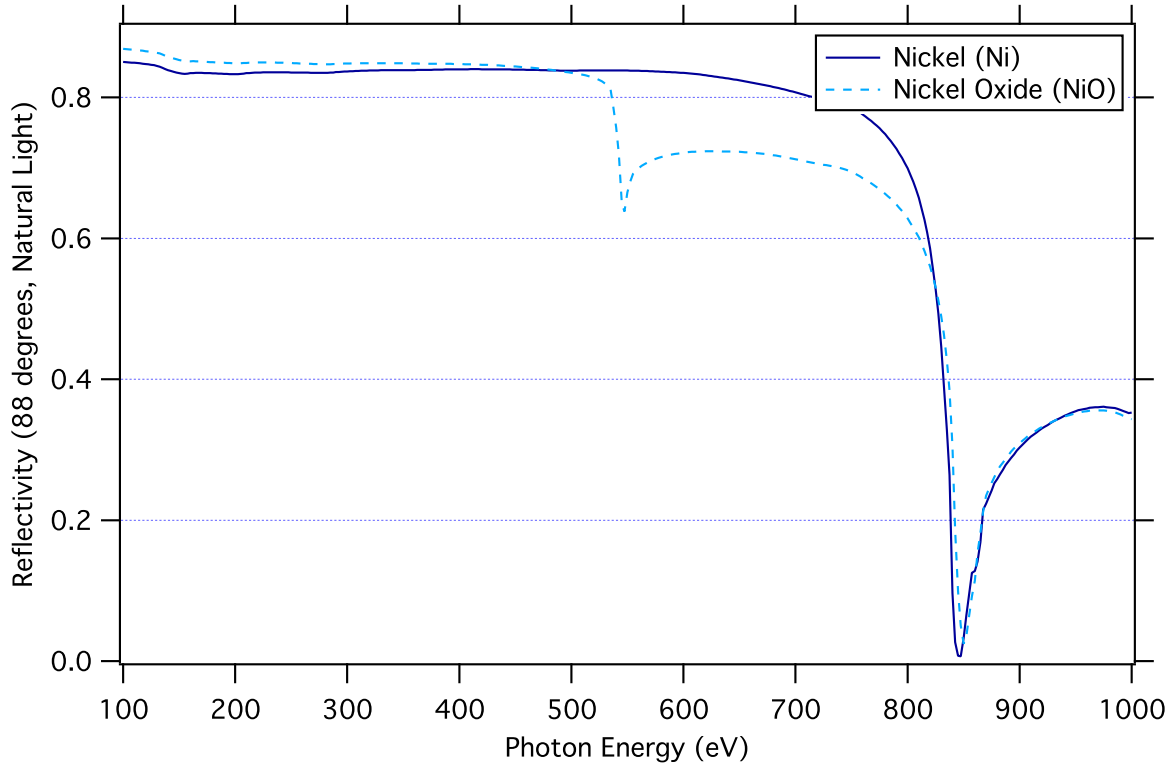


Figure 6.8: Unprotected Nickel quickly forms a surface oxide of NiO, which strongly reduces the reflectivity at the Oxygen edge (525eV)

6.4.2 IMP

(nickel): Profile clean, blaze angle off [modelled]. Oxidized Modelled as NI, layer of NiO.

TEST: NiO on top of Ni? layer thickness Caveat: Henke data reflectivities are not correct at/near absorption edges... shouldn't totally match theoretical shape.

- compare AFM and fitted

scattering factor: http://www2.astro.psu.edu/niel/astro485/xrayschool/schwartz-xray_optics.pdf - $1/\sin(\theta)$

6.4.3 MEG

(nickel): profile ok, blaze angle off [modelled]. Oxidized Modelled as combination of NiO and NiO₂.

6.4.4 HEG

(Pt): almost no diffraction performance at all. AFM: revealed double-peak structure; not ruled correctly.
Sent back to manuf.

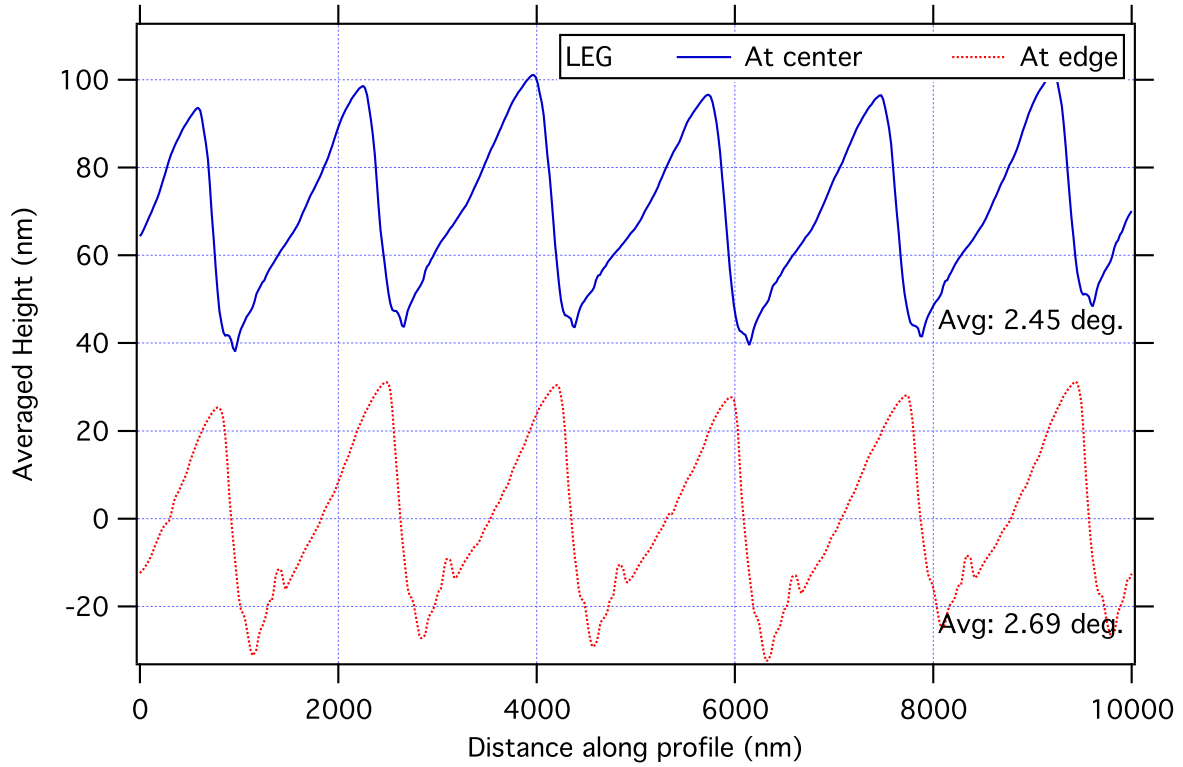


Figure 6.9: AFM measurements of the Low Energy Grating (LEG) profile, averaged along the grooves (TODO μm x TODO μm). The best-fit blaze angle is at the centre of the grating.

6.4.5 HRMEG and HRHEG

(Pt): blaze angles very off Unsuitable for actual application in 3rd order. - Temporary plan: Using HRHEG (2600l/mm) in place of HEG (2000l/mm) since blaze angle error makes it suitable for use in 1st order. - DATA 5q: plot expected reduction in efficiency

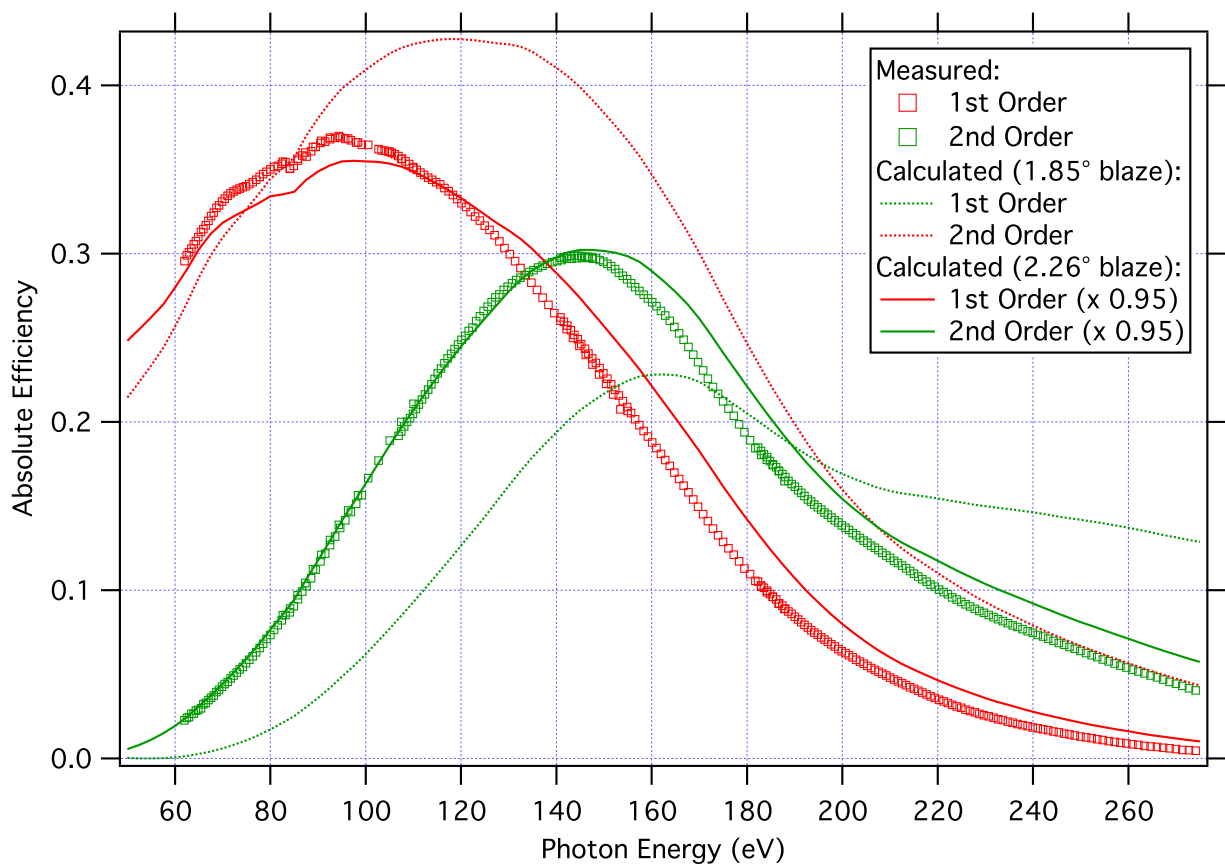


Figure 6.10: Theoretical and measured efficiency of the Low Energy Grating (LEG).

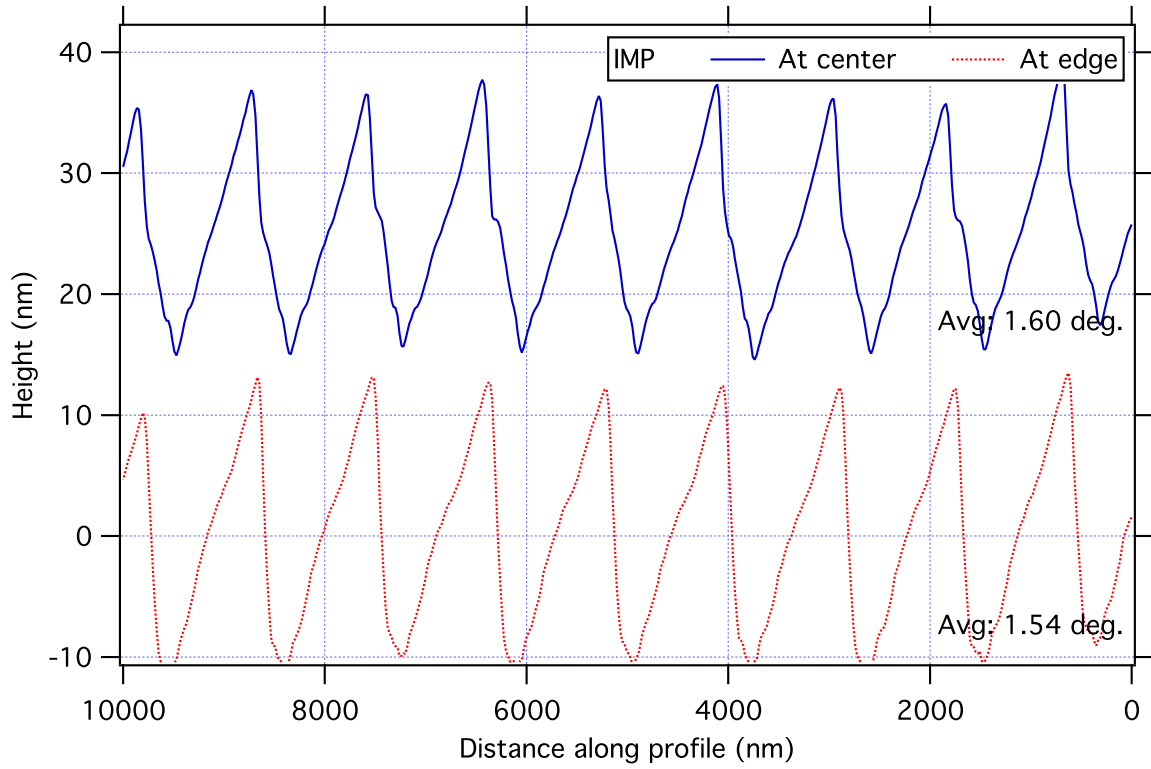


Figure 6.11: AFM measurements of the Impurity Grating (IMP) profile, averaged along the grooves (TODO μm x TODO μm). The best-fit blaze angle is at the centre of the grating.

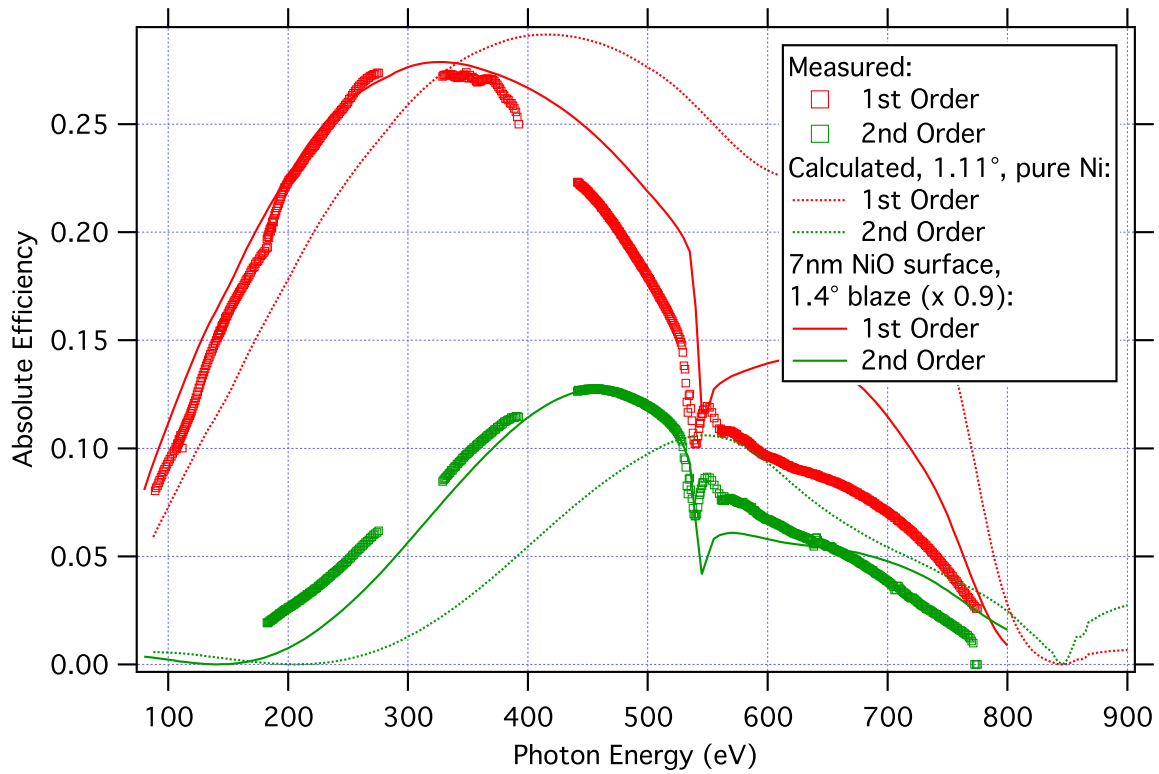


Figure 6.12: Theoretical and measured efficiency of the Impurity Grating (IMP).

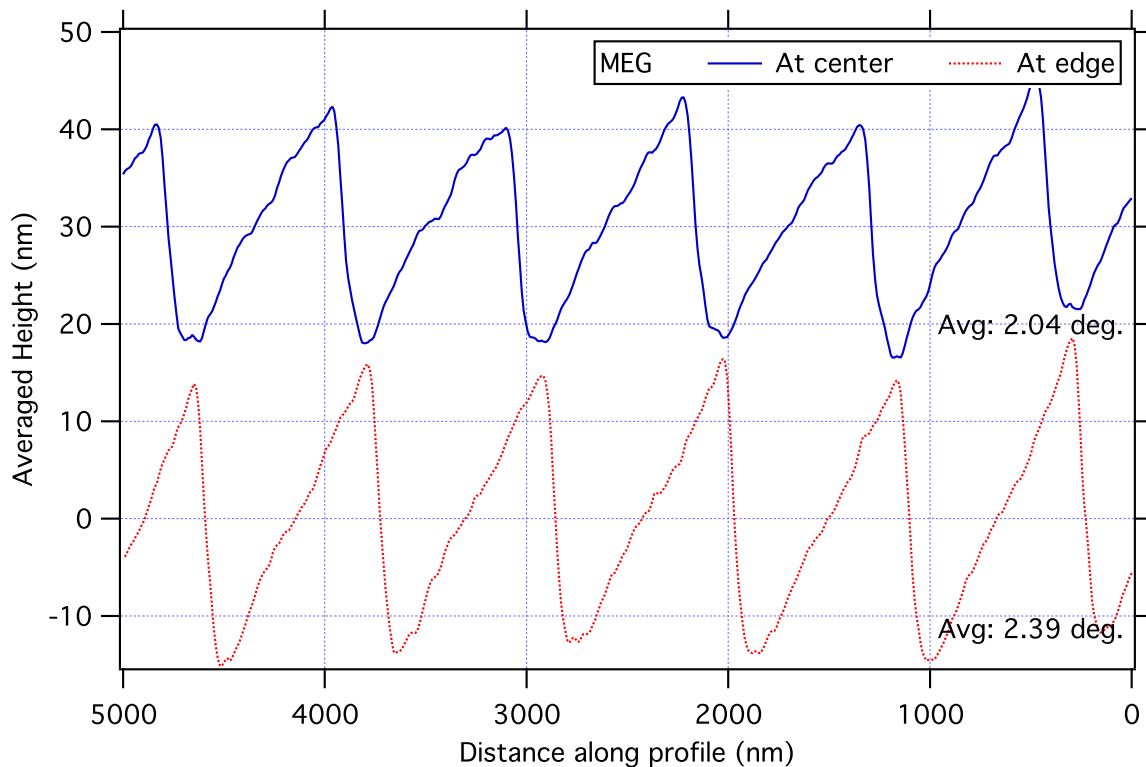


Figure 6.13: AFM measurements of the Medium Energy Grating (MEG) profile, averaged along the grooves (TODO μm x TODO μm). The best-fit blaze angle is at the centre of the grating.

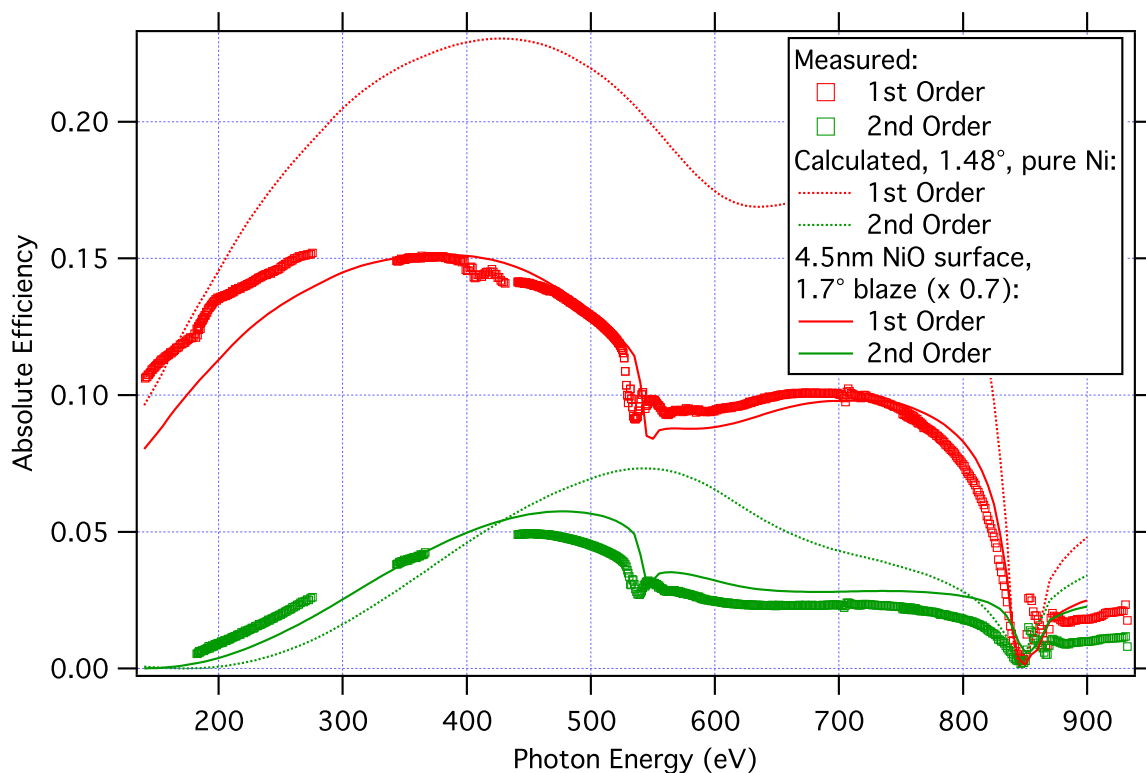


Figure 6.14: Theoretical and measured efficiency of the Medium Energy Grating (LEG).

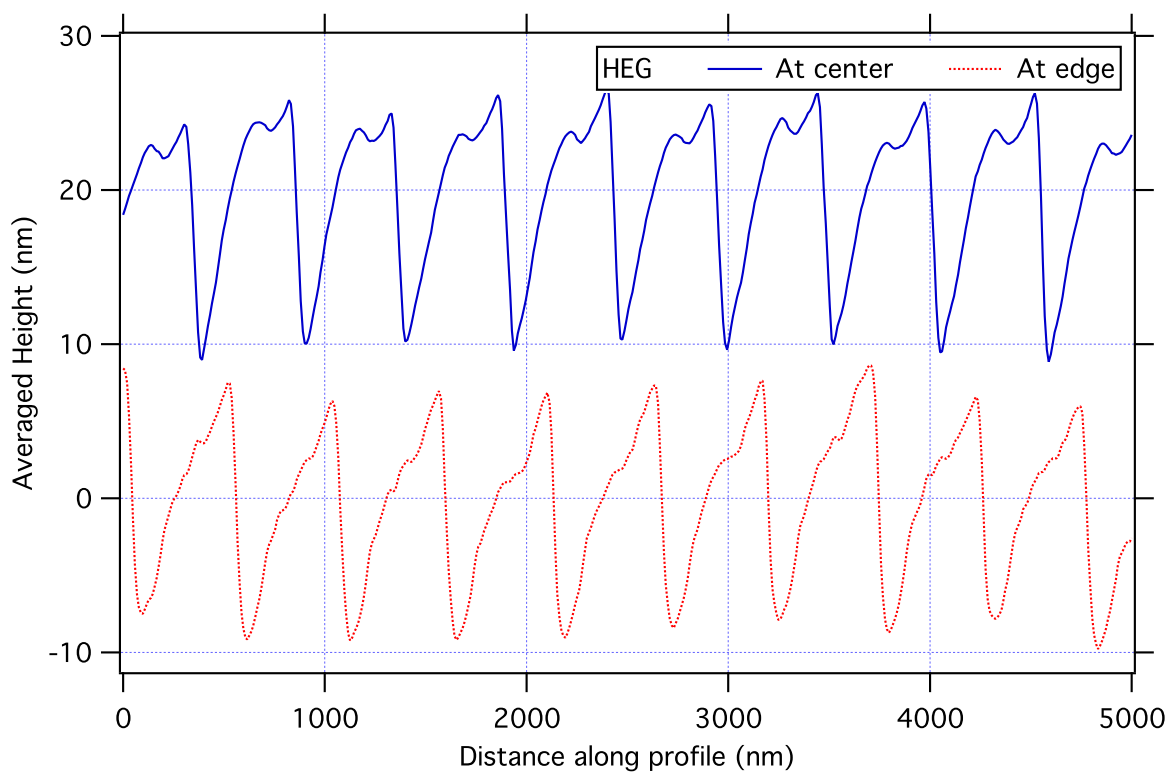


Figure 6.15: AFM measurements of the High Energy Grating (HEG) profile, averaged along the grooves (TODO μm x TODO μm). Severe ruling errors were apparent. The profile wasn't sufficiently triangular to attempt to fit a blaze angle.

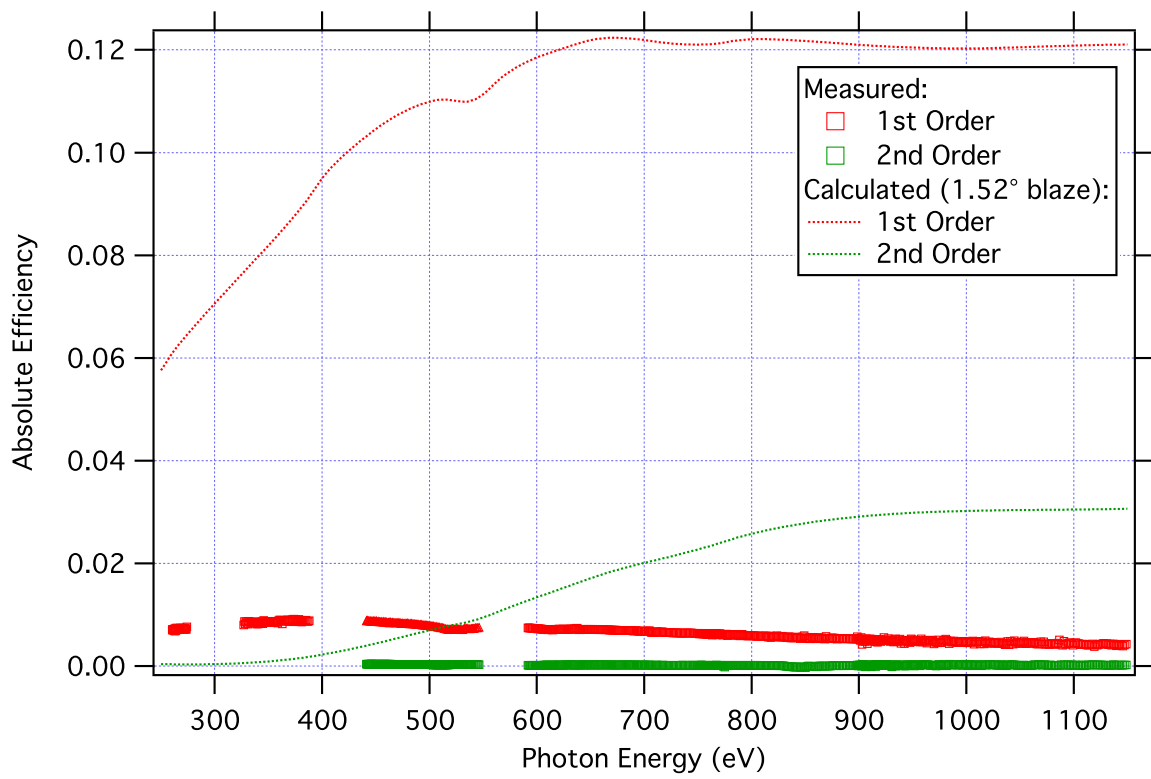


Figure 6.16: Theoretical and measured efficiency of the High Energy Grating (LEG).

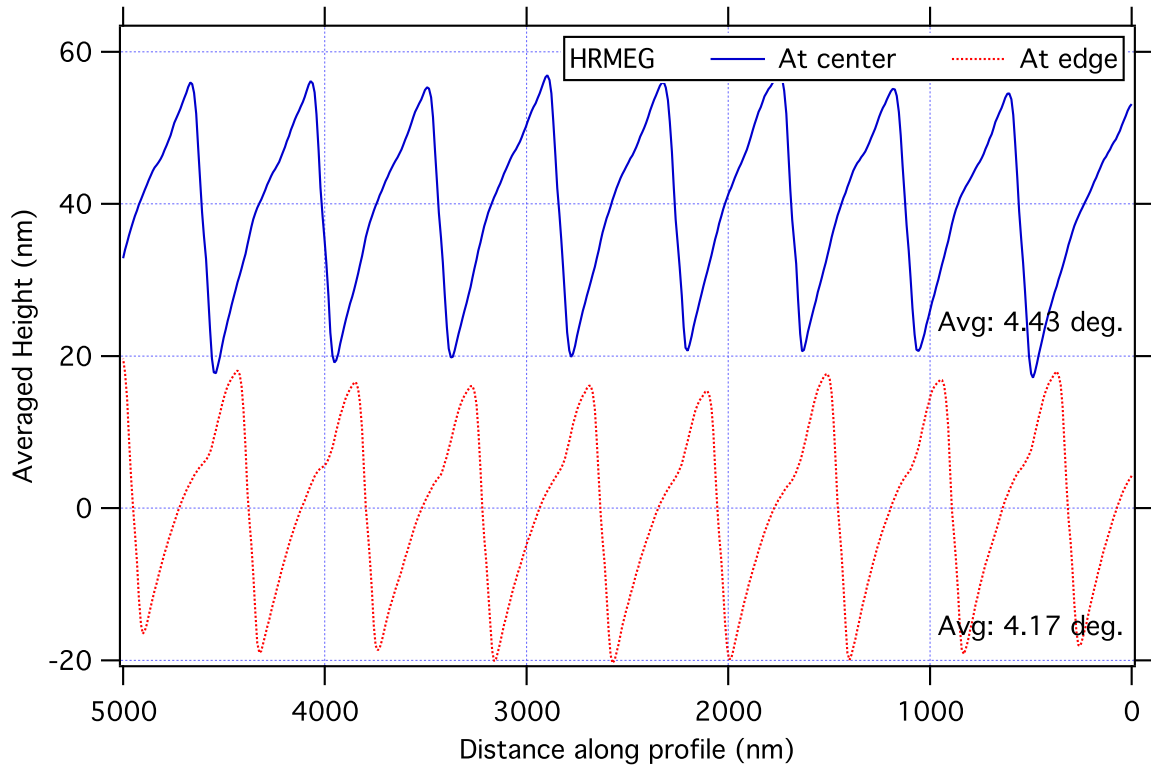


Figure 6.17: AFM measurements of the HighRes Medium Energy Grating (HRMEG) profile, averaged along the grooves (TODO μm x TODO μm). The best-fit blaze angle is at the centre of the grating.

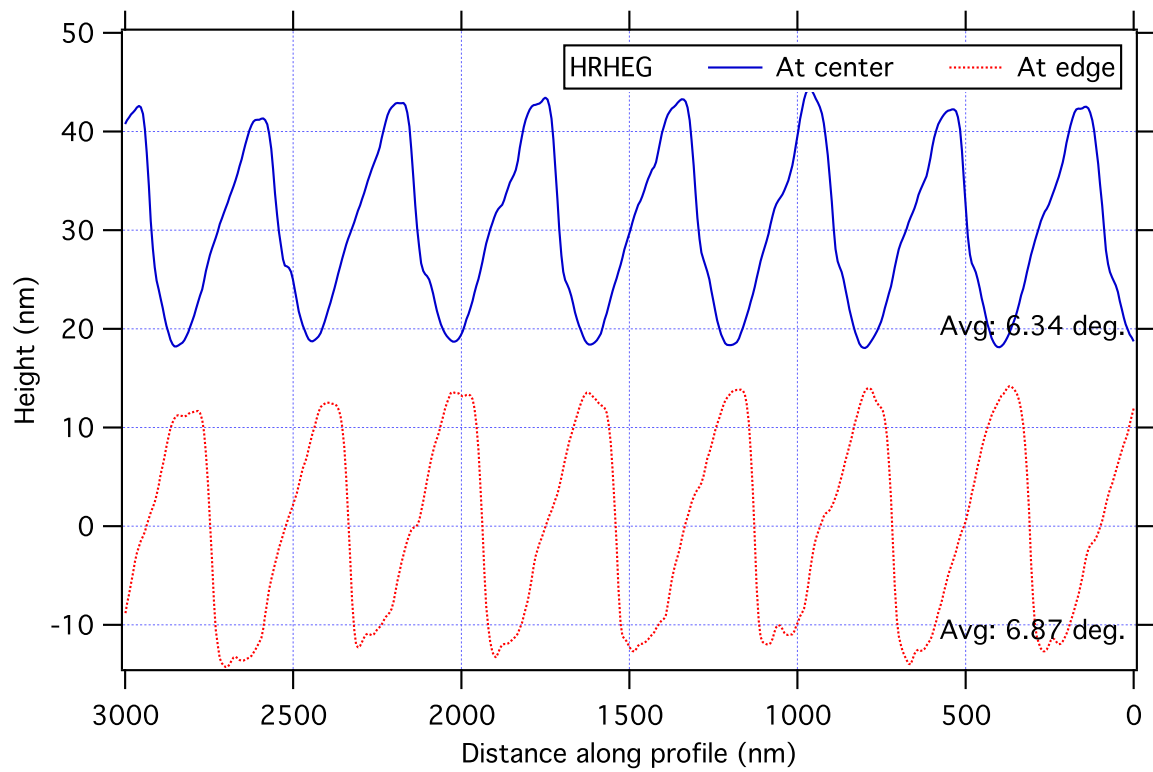


Figure 6.18: AFM measurements of the HighRes High Energy Grating (HRHEG) profile, averaged along the grooves (TODO μm x TODO μm). The best-fit blaze angle is at the centre of the grating.

CHAPTER 7

REAL-WORLD RESULTS: WHY THERE AREN'T ANY YET

- Real-world results: - Unfortunately none yet... Problems with spectrometer: - Mechanical design flaws (crashing; hexapod range) - electrical wiring and noise problems (sensitive detector in-vacuum; can't be on long signal cables) - Grating manufacturing, as covered above.

CHAPTER 8

FUTURE WORK: WHAT SHOULD HAVE BEEN IN CHAPTER 6

- Grating efficiency engine: own open-source software [combine differential method and RCWA use as check on each other, or within areas of applicability] - Cloud computing: distribute over many cores, but only for a short time. Calculations can be done massively in parallel. - web service accessible to beamline designers everywhere - Make beamline work Publish actual spectrometer results

REFERENCES

- [1] J.R. Andrewartha, G.H. Derrick, and R.C. McPhedran. A general modal theory for reflection gratings. *Optica Acta: International Journal of Optics*, 28(11):1501–1516, 1981.
- [2] I.C. Botten, M.S. Craig, R.C. McPhedran, J.L. Adams, and J.R. Andrewartha. The dielectric lamellar diffraction grating. *Optica Acta: International Journal of Optics*, 28(3):413–428, 1981.
- [3] L.C. Botten, M.S. Craig, R.C. McPhedran, J.L. Adams, and J.R. Andrewartha. The finitely conducting lamellar diffraction grating. *Optica Acta: International Journal of Optics*, 28(8):1087–1102, 1981.
- [4] L. Braicovich, J. van den Brink, V. Bisogni, M. Moretti Sala, L. J. P. Ament, N. B. Brookes, G. M. De Luca, M. Salluzzo, T. Schmitt, V. N. Strocov, and G. Ghiringhelli. Magnetic excitations and phase separation in the underdoped $\text{La}_{2-x}\text{Sr}_x\text{CuO}_4$ superconductor measured by resonant inelastic x-ray scattering. *Phys. Rev. Lett.*, 104:077002, Feb 2010.
- [5] S. M. Butorin, J.-H. Guo, M. Magnuson, P. Kuiper, and J. Nordgren. Low-energy $d-d$ excitations in MnO studied by resonant x-ray fluorescence spectroscopy. *Phys. Rev. B*, 54:4405–4408, Aug 1996.
- [6] F. M. F. de Groot, J. C. Fuggle, B. T. Thole, and G. A. Sawatzky. $2p$ x-ray absorption of $3d$ transition-metal compounds: An atomic multiplet description including the crystal field. *Phys. Rev. B*, 42:5459–5468, Sep 1990.
- [7] Center for X-Ray Optics. X-ray interactions with matter calculator. http://henke.lbl.gov/optical_constants/, October 2011.
- [8] J. Fraunhofer. Kurzer bericht von den resultaten neuerer versuche über die gesetze des lichtes, und die theorie derselben (Short account of the results of new experiments on the laws of light, and their theory). *Annalen der Physik*, 74(8):337–378, 1823.
- [9] J. Fraunhofer, J.S. Ames, and W.H. Wollaston. *Prismatic and diffraction spectra*. Harper’s scientific memoirs. Harper & brothers, 1898.
- [10] Ocean Optics Inc. Usb4000-uv-vis miniature fiber optic spectrometer. <http://www.oceanoptics.com/Products/usb4000uvvis.asp>, October 2011.
- [11] Pavageau J. and Bousquet M.J. Diffraction par un reseau conducteur nouvelle methode de resolution. *Journal of Modern Optics*, 17(6):469–478, 1970.
- [12] J. J. Jia, T. A. Callcott, J. Yurkas, A. W. Ellis, F. J. Himpsel, M. G. Samant, J. Stöhr, D. L. Ederer, J. A. Carlisle, E. A. Hudson, L. J. Terminello, D. K. Shuh, and R. C. C. Perera. First experimental results from IBM/TENN/TULANE/LLNL/LBL undulator beamline at the Advanced Light Source. *Review of Scientific Instruments*, 66(2):1394–1397, 1995.
- [13] Lifeng Li. Formulation and comparison of two recursive matrix algorithms for modeling layered diffraction gratings. *J. Opt. Soc. Am. A*, 13(5):1024–1035, May 1996.
- [14] Lifeng Li. Use of fourier series in the analysis of discontinuous periodic structures. *J. Opt. Soc. Am. A*, 13(9):1870–1876, Sep 1996.
- [15] D. Maystre. Sur la diffraction d’une onde plane par un reseau metallique de conductivite finie. *Optics Communications*, 6(1):50 – 54, 1972.

- [16] F. Montiel, M. Neviere, and P. Peyrot. Waveguide confinement of cerenkov second-harmonic generation through a graded-index grating coupler: Electromagnetic optimization. *Journal of Modern Optics*, 45(10):2169–2186, 1998.
- [17] David Muir. Design of a high performance soft x-ray emission spectrometer for the REIXS beamline at the canadian light source. Master’s thesis, University of Saskatchewan, 2006.
- [18] M. Nevière and E. Popov. *Light propagation in periodic media: differential theory and design*. Optical engineering. Marcel Dekker, 2003.
- [19] W.B. Peatman. *Gratings, mirrors, and slits: beamline design for soft X-ray synchrotron radiation sources*. Gordon and Breach Science Publishers, 1997.
- [20] H. Petersen, C. Jung, C. Hellwig, W. B. Peatman, and W. Gudat. Review of plane grating focusing for soft x-ray monochromators. *Review of Scientific Instruments*, 66(1):1–14, 1995.
- [21] R. Petit. Contribution à l’étude de la diffraction par un réseau métallique. *Rev. Opt.*, 45:249–276, 1966.
- [22] R. Petit and M. Cadilhac. Electromagnetic theory of gratings: some advances and some comments on the use of the operator formalism. *J. Opt. Soc. Am. A*, 7(9):1666–1674, Sep 1990.
- [23] A. Pietzsch, Y.-P. Sun, F. Hennies, Z. Rinkevicius, H. O. Karlsson, T. Schmitt, N. Strocov, V. J. Andersson, B. Kennedy, J. Schlappa, A. Föhlisch, J.-E. Rubensson, and F. Gel’mukhanov. Spatial quantum beats in vibrational resonant inelastic soft x-ray scattering at dissociating states in oxygen. *Phys. Rev. Lett.*, 106:153004, Apr 2011.
- [24] Evgeny Popov and Michel Nevière. Maxwell equations in fourier space: fast-converging formulation for diffraction by arbitrary shaped, periodic, anisotropic media. *J. Opt. Soc. Am. A*, 18(11):2886–2894, Nov 2001.
- [25] J.W.S. Rayleigh. *The theory of sound*. Number v. 2 in The Theory of Sound. Macmillan, 1896.
- [26] Lord Rayleigh. On the dynamical theory of gratings. *Proceedings of the Royal Society of London. Series A, Containing Papers of a Mathematical and Physical Character*, 79(532):pp. 399–416, 1907.
- [27] A. Wirgin. Selected papers from the ursi symp. *Alta. Freq.*, 38:327–338, 1969.
- [28] P. Zeeman. On the influence of magnetism on the nature of the light emitted by a substance. *Astrophysical Journal*, 5:332, 1897.

APPENDIX A

SAMPLE APPENDIX

Stuff for this appendix goes here.

APPENDIX B

ANOTHER SAMPLE APPENDIX

Stuff for this appendix goes here.